A theoretical study of thermoelectric efficiency and cooling power in organic molecular junctions

Fatemehsadat Tabatabaeikahangi

N° d'ordre NNT: 2021LYSE1179

THÈSE DE DOCTORAT DE L'UNIVERSITÉ DE LYON

opérée au sein de

l'Université Claude Bernard Lyon 1

École Doctorale ED52

Physique et Astrophysique

Spécialité de doctorat :Nano-électrothermique

Discipline : Physique

Soutenue publiquement le 29/09/2021, par:

TABATABAEI Fatemeh

A theoretical study of thermoelectric efficiency and cooling power in organic molecular junctions

---

Devant le jury composé de:

BANFI Francesco, Professeur des Universités, Universite Lyon 1	Président.e
MARTIN Evelyne, Directrice de Recherche, CNRS Strasbourg	Rapporteure
PECCHIA Alessandro, Chercheur, Université de Rome-Tor Vergata (Italie)	Rapporteur
GOTSMANN Bernd, Chercheur, IBM Research-Zurich (Suisse)	Examinateur
MICHELINI Fabienne, Maître de conférences, Aix-Marseille Universite	Examinateurice
NIEHAUS Thomas, Professeur, Université Lyon 1	Directeur de thèse
MERABIA Samy, Directeur de Recherche, CNRS Lyon	Co-directeur de thèse
CHAPUIS Pierre-Olivier, Chargé de Recherche, CNRS Lyon	Invité
SAINT-MARTIN Jérôme, Maître de Conférences, Universite Paris Saclay	Invité

A theoretical study of thermoelectric efficiency and cooling power in organic molecular junctions

Fatemeh TABATABAEI

Abstract

Thermoelectricity is the conversion of heat to electricity and vice versa. As Seebeck discovered, a voltage applied to an electronic device generates a heat current, while a temperature difference can generate electricity. During the past decades, the size of consumer electronics has been continuously decreasing. The down-sizing of the electronic devices requires a more efficient heat management. An interesting route towards this goal is the idea of using single molecules as electronic components which gave rise to "molecular electronics". In fact, the usage of organic molecules in thermoelectric applications has attracted a great deal of attention due to their flexibility, relatively low price and their eco-friendly nature. In this work, the thermoelectric properties of molecular junctions based on oligo(phenyleneethynylene) (OPE3) derivatives were studied. With the help of Density Functional Theory (DFT) calculations, models for the molecular junctions were constructed. The electronic transport properties were obtained using Non Equilibrium Green's Function-Density Functional based Tight-Binding (NEGF-DFTB). Firstly, the effect of side groups on the electronic conductance and thermopower of OPE3 derivatives was quantified. It is shown that these derivatives provide structural properties that are needed for highly efficient thermoelectric materials. Next, the effect of cross-linking molecules on the thermoelectric efficiency was investigated. Classical Molecular Dynamics (MD) was used to compute the phonon transport across the junctions. Combining the results from ab-initio and MD for electron and phonon transport, respectively, the thermoelectric efficiency in terms of the figure of merit ZT was computed for OPE3 derivatives. We have found that cross-linked molecules show a high ZT value, which makes them good candidates to be used as cooling systems. Finally, we introduce a circuit model that combines electron and phonon transport channels. This

model allows to determine optimal parameter ranges in order to maximize cooling. Overall, our results demonstrate that the OPE3 derivatives display the necessary structural rigidity and compatible electronic structure to enable high performance devices for cooling applications.

Supervisors: Prof. Dr. Thomas NIEHAUS and Dr. Samy MERABIA

Acknowledgements

Acknowledgements

Contents

Declaration

The work in this thesis is based on research carried out at the institut Lumière Matière (ILM), UMR5306 - UCBL - CNRS, France and I was a PhD student at École doctorale de Physique et d'Astrophysique (PHAST).

No part of this thesis has been submitted elsewhere for any other degree or qualification, and it is the sole work of the author unless referenced to the contrary in the text.

Some of the work presented in this thesis has been published in journals and conference proceedings - the relevant publications are listed below.

Publications

Relevant Publications

List of Figures

List of Tables

Nomenclature

EFINED Energy Filtering Non-Equilibrium Devices

DFT Density Functional Theory

LDA Local Density Approximation

GGA Generalized Gradient Approximations

PBE Perdew, Burke, and Ernzerhof

DFTB Density Functional based Tight-Binding

SCC-DFTB Self consistent charge- Density functional tight-binding

TB Tight Binding

NEGF Non Equilibrium Green's Function

NEGF-DFTB Non Equilibrium Green's Function-Density Functional based Tight-Binding

MD Molecular Dynamics

LAMMPS Large-scale Atomic/Molecular Massively Parallel Simulator

OPLS Optimized Potentials for Liquid Simulations

AMBER Assisted Model Building with Energy Refinement

PBC Periodic boundary conditions

NEMD Non-equilibrium molecular dynamics

OPE3 oligo(phenyleneethynylene)

DHBT dihydrobenzo[b]thiophene

I-V current-voltage

Introduction

"We must be clear that when it comes to atoms, language can be used only as in poetry"

— Niels Bohr

The demand for down-scaling size of daily used electronic devices has been rising [6, 7, 8]. The high heat dissipation in micro and nano devices necessitates optimizing the efficiency and their cooling [9, 3]. To this end, minimization of phonon transport, construct electronic refrigerators and harvesting thermal energy is the path. [10, 11, 12]. Building new molecular devices and understanding the electron, heat and near field energy flux as well as overcome the limitations in this field is our final goal in Energy Filtering Non-Equilibrium Devices (EFINED) project. This project is a teamwork that merges theory, experiment and the development of the device technology.

In the framework of EFINED project (see Fig.0.1), we simulated the electron and phonon energy flux. The main question in our part is:

How much cooling happens in the candidate molecular junctions?

To answer this question, we computed:

- Electronic properties of the molecular junctions
- Thermal properties of the molecular junctions

- Thermoelectric efficiency of the molecular junctions

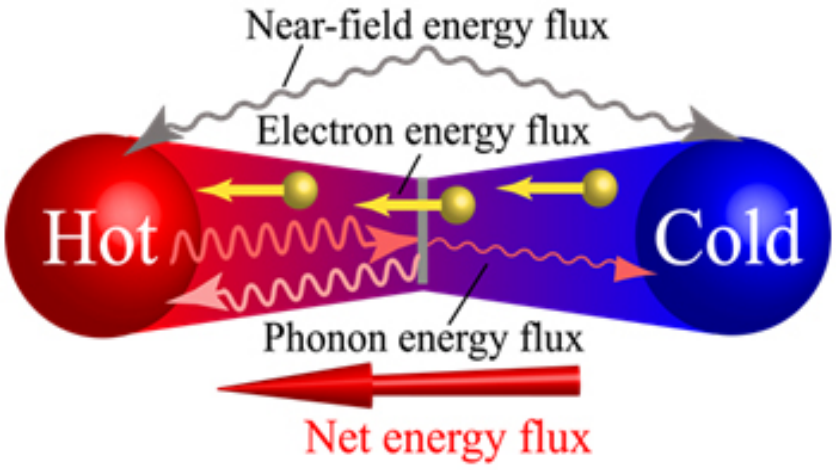

Figure 0.1: Particle and energy fluxes in junction between hot and cold electrodes during electronic cooling [1].

In the present work, chapter.1 is on "electron structure of solids" and a brief description of Density Functional Theory DFT, Density Functional Tight Binding Density Functional based Tight-Binding (DFTB), and Non-equilibrium Green's Function Non Equilibrium Green's Function (NEGF) to compute the electronic transport.

Chapter.2 covers a general introduction about "phonons in molecular systems", where molecular dynamic MD simulations, and non-equilibrium molecular dynamic Non-equilibrium molecular dynamics (NEMD) approach to calculate the phonon transport are described.

Chapter.3 on "thermoelectricity in molecular systems", we showed how to calculate thermoelectric efficiency using all the thermoelectric properties that have been computed where the methods in first two chapters were employed.

In chapter.4, "Electronic conductance and thermopower of single molecular junctions" were computed, where we studied the effect of side groups on the electronic properties of OPE3 molecular junctions.

Chapter.5 was written on "Thermoelectricity of cross-linked molecular junctions", where we computed the electronic and thermal transport of cross-linked molecular

junctions and used these properties to calculate the thermopower and thermoelectric efficiency.

At last, in chapter.6, "out of equilibrium", the main question was answered. The optimal cooling power were calculated for the molecular junctions under bias voltage. Finally, applying an electro-thermal circuit model, the maximum cooling temperatures were computed.

Chapter 1

Electron structure of solids

"When you change the way you look at things, the things you look at change. "

— Max Planck

1.1 Schrödinger equation for a many-body system

The electronic structure of a solid is based on the behaviour of electrons and the nuclei in the system. To investigate this behaviour, quantum mechanics is the proven theory to use. The heart of quantum mechanic is the Schrödinger equation for a solid system with n electrons and N nuclei

$$H_{total}\Psi_{total}(\mathbf{R},\mathbf{r}) = E_{total}\Psi_{total}(\mathbf{R},\mathbf{r}), \tag{1.1}$$

where H_{total} is the Hamiltonian of the system, Ψ_{total} is the wave function, $\mathbf{r}$ and $\mathbf{R}$ are representing the coordinate vector of all n electron and N nuclei, respectively, and E_{total} is the total energy for the system. More precisely, we can write the Hamiltonian as following

$$H_{total} = T_{nn} + T_{ee} + V_{ee} + V_{nn} + V_{ext}, \tag{1.2}$$

where T_{nn} is the kinetic energy of nuclei, T_{ee} is the kinetic energy of electrons, V_{ee} is the Coulomb interactions between electrons, V_{nn} is the Coulomb interactions between nuclei, and V_{ext} is the Coulomb interactions between electrons and nuclei

and considered as an external potential [13, 14]. Throughout this thesis, we use atomic units for all the equations.

1.1.1 Born–Oppenheimer approximation

Considering the fact that the mass of nuclei is considerably bigger than the mass of electrons we can separate their motions from each other in solving the Schrödinger equation of a many-body system [15]. This approach called "Born–Oppenheimer approximation " helps us to break down the many-body Schrödinger equation to two parts: nuclei and electrons. When applying Born–Oppenheimer approximation, we consider that the nuclei are at a constant position. Therefore, we can neglect the kinetic energy of nuclei in the Hamiltonian when solving the Schrödinger equation for electrons. Additionally, the number of variables in our wave function decreases. The other consequence of this approximation is that the Coulomb energy between nuclei is constant. Furthermore, in the total wave function of the system, the positions of nuclei are not varying anymore.

All in all, now we can write the Schrödinger equation for electrons as

$$H_{electrons}\Psi(\mathbf{r}) = E\Psi(\mathbf{r}), \tag{1.3}$$

where $\Psi(\mathbf{r})$ is the all-electron wave function. As for the Hamiltonian, the T_{nn} cancels and V_{nn} is a constant term in the Hamiltonian, we consider it as a shift in the potential and neglect it. Therefore, the Hamiltonian reads

$$H_{electrons} = T_{ee} + V_{ee} + V_{ext}. \tag{1.4}$$

Henceforth, the problem reduces to equation 1.3 for electrons.

1.2 Density functional theory

It is fair to say a significant amount of work in the field of quantum chemistry is devoted to solving equation 1.3. In 1998, the Nobel prize in chemistry was given to

Walter Kohn a theoretical physicist and John Pople a theoretical chemist. Walter Kohn for his work of developing the base of DFT and John Pople for developing a quantum chemistry package in order to calculate the electronic structure of atoms and molecules. There was a key difference between Kohn and Pople approaches. Kohn (DFT) focused on electronic density and Pople tried to extract all the properties of the system from the wave function. As Kohn mentioned in his Nobel prize lecture, there are advantages and disadvantages to both theories.

As we take out a path in chemistry or physics, we are trained to think about quantum physics in terms of wave functions. Solving the Schrödinger equation using wave function based approaches, has been satisfying. Moreover, in the case of high accuracy needed or increasing the number of particles in the system the calculation is time consuming. Additionally, when increasing the number of particles, the physical behaviour is very complicated to understand and the time of calculation grows exponentially. Therefore, if the system does not have high symmetry, these approaches become very expensive. On the other hand, density functional theory derives the physical properties of the system from electron density of many-body systems. This helps to have a better insight of many-body system's nature. Moreover, the time needed for DFT calculation does not grow exponentially with respect to the number of atoms, it grows by the power of three.

Nevertheless, as not all the interactions between electrons in DFT is not known, using wave function based methods holds an asset over DFT in that with a well defined wave function and infinite computer time, it will reach the exact solutions [16].

Without further discussion, let's commence solving equation 1.3 in the framework of DFT. Thence, consider an n-electron system.

Applying the Born–Oppenheimer approximation, we can write the Schrödinger

equation for electrons as below:

$$\left(-\frac{1}{2}\sum_{i=1}^{n}\nabla_i^2+\frac{1}{2}\sum_{i=1}^{n}\sum_{j=1,j\neq i}^{n}\frac{1}{|r_i-r_j|}+\sum_{i=1}^{n}V_{ext}(r_i)\right)\Psi(r_1,r_2,...,r_n)=E\Psi(r_1,r_2,...,r_n). \tag{1.5}$$

Using Dirac representation, we can write:

$$H_{el}\left|\Psi\right\rangle = E\left|\Psi\right\rangle. \tag{1.6}$$

The goal would be to find the ground state energy and to do so we need to minimize the energy. We can do it using the variational theorem:

$$E_0 = Min_{\Psi}\left\langle\Psi|H_{el}|\Psi\right\rangle, \tag{1.7}$$

where Ψ is normalized to the number of electrons in the system, meaning if we define the density of electron at position r in a many-body system with n electrons as below

$$\rho(\mathbf{r}) = n\int\int...\int\left|\Psi(r,r_1,....,r_{n-1})\right|^2 dr_1....dr_{n-1}, \tag{1.8}$$

then we will have:

$$\int\rho(\mathbf{r})d\mathbf{r} = n. \tag{1.9}$$

The idea behind density functional theory is to formulate everything in terms of the electron density [17].

DFT is based on Hohenberg–Kohn theorems. The first Hohenberg–Kohn theorem asserts that the ground state of any interacting many-body system is a unique functional of the electron density $\rho(\mathbf{r})$ [17]:

$$E = E[\rho(\mathbf{r})]. \tag{1.10}$$

The first Hohenberg–Kohn theorem proves that a functional of the electron density $E[\rho]$ exists but it does not talk about the form of this functional. The second Hohenberg–Kohn theorem states that the electron density that minimizes the energy of the overall functional is the true electron density corresponding to the full solution of the Schrödinger equation [17].

Hence, instead of finding the all-electron wave function with 3n degrees of freedom, we should find the electron density of the system with 3 degrees of freedom [17].

In principle, every property of the system that we extract from the electron wave function can be derived from the electron density as well. It is time to finally rephrase the equations in terms of density. In DFT instead of assuming an n-electron system where all the electrons are correlated, we assume a system with n non-interacting electrons, and this system shares the same electron density with the true system. Electrons are indistinguishable fermions, hence, there is Pauli repulsion interaction between them. Moreover, the movement of one electron is affected by the presence of all the other electrons. All these effects are to be described by the energy functional called "exchange-correlation functional". As a result, the total electron wave function of the non-interacting system can be written as a product of single electron wave functions, $\Psi_i(\mathbf{r})$. And the electron density is

$$\rho(\mathbf{r}) = \sum_{i=1}^{n} \Psi_i(\mathbf{r})\Psi_i^*(\mathbf{r}). \tag{1.11}$$

Instantly, the energy functional in terms of electron density reads

$$E[\rho] = T_s[\rho] + E_{ext}[\rho] + E_H[\rho] + E_{xc}[\rho], \tag{1.12}$$

where

$$T_s[\rho] = \sum_{i=1}^{n} \int d\mathbf{r}\Psi_i(\mathbf{r})\Big(-\frac{\nabla^2}{2}\Big)\Psi_i(\mathbf{r}), \tag{1.13}$$

is the kinetic energy of the non-interacting system, E_{ext} is the external energy functional and reads

$$E_{ext}[\rho] = \int V_{ext}(\mathbf{r})\rho(\mathbf{r})d\mathbf{r}, \tag{1.14}$$

where V_{ext} is the external potential due to the Coulomb interaction between nuclei and electrons, E_H known as Hartree energy functional is the Coulomb interaction between electrons

$$E_H[\rho] = \frac{1}{2}\int \frac{\rho(\mathbf{r})\rho(\mathbf{r}')}{|\mathbf{r}-\mathbf{r}'|}d\mathbf{r}d\mathbf{r}', \tag{1.15}$$

and the last term ,$E_{xc}[\rho]$, is the exchange-correlation functional (we will talk more about this term in sections 1.2.1). Straightforward, the Schrödinger equation for

one electron reads

$$\Big(-\frac{\nabla^2}{2}+V_{ext}(\mathbf{r})+V_H(\mathbf{r})+V_{xc}(\mathbf{r})\Big)\Psi_i(\mathbf{r})=\epsilon_i\Psi_i(\mathbf{r}), \tag{1.16}$$

where $V_H \equiv \frac{\delta E_H[\rho]}{\delta\rho(\mathbf{r})}$, is the Hartree potential, $V_{xc} \equiv \frac{\delta E_{xc}[\rho]}{\delta\rho(\mathbf{r})}$, is the exchange-correlation potential, ϵ_i is the energy eigenvalue for single electron, and $\Psi_i(\mathbf{r})$ is single electron wave-function. This equation is called Kohn-Sham equation, which describes the particles in the non-interacting system. These particles in the non-interacting system are called "Kohn-Sham" particles.

In many-body scale even after applying Born-Oppenheimer approximation, we consider the electrons interacting with each other and also with nuclei. Since each electron has three degrees of freedom the dimension of the problem is 3n (n number of electrons). In DFT instead of considering all these interactions, we assume that the Kohn-Sham particle is interacting with an effective potential from all the other electrons in the system and we consider all of these effects inside the density functional (Fig.1.1). DFT reduces the many-body problem with 3n degrees of freedom to n single electron problems with only three degrees of freedom for the electron density $\rho(\mathbf{r})$.

1.2.1 Exchange-correlation functional

So far, everything in DFT is exact. The many-body problem has been reduced to the single Kohn-Sham electron equation 1.16. We also know how to solve the Kohn-Sham equation using self consistent approach which we will discuss in section 1.2.3. In equation 1.16 every term in the Hamiltonian is known, except the V_{xc}. There has been a lot of effort to develop an exchange-correlation functional that works for every many-body system.

Historically, the first functional introduced is the Local Density Approximation (LDA). The exchange energy functional for to the uniform electron gas has been calculated analytically by Dirac et al. [18] as

$$E_x^{LDA}[\rho]=-\frac{3}{4}\Big(\frac{3}{\pi}\Big)^{\frac{1}{3}}\int\rho(\mathbf{r})^{\frac{4}{3}}d\mathbf{r}, \tag{1.17}$$

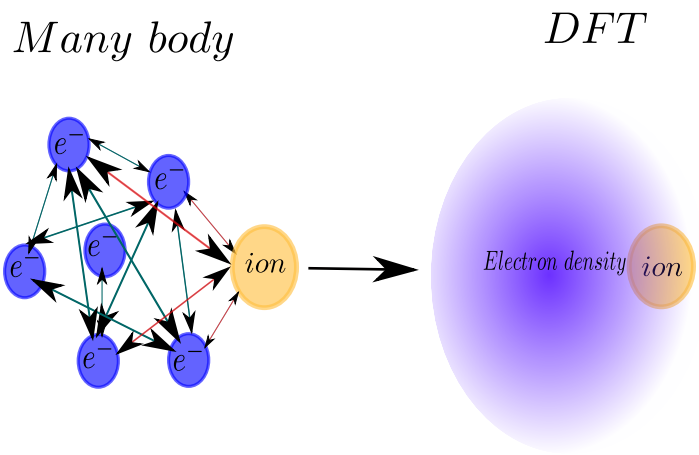

Figure 1.1: In a many-body system, there are n electrons in the system which interact with each other and each of them interacts with the nucleus (ion), vs in DFT we consider the electron density of all the electrons interacting with the ion

and correlation term of the exchange-correlation functional is derived by Monte Carlo simulations [19]. This functional has been used to predict the electronic structure of solids with good accuracy [20], since the errors coming from the exchange and correlation parts cancel each other, which is known as "error compensation". As successful as this functional can be for such systems with uniform electron density, it fails to describe all the physical properties of a many-body system.

Subsequently, by adding the gradient of density $\nabla\rho$ to the exchange-correlation functional, the development of Generalized Gradient Approximations (GGA) exchange-correlation functionals has been started. One of the GGA functionals has been developed by Perdew, Burke, and Ernzerhof (PBE) [21, 22], and it is the most used exchange-correlation functional in literature. We will also use this exchange-correlation functional for our calculations [23].

With this in mind, further development of exchange-correlation functionals continued. The so called "Meta-GGA" functionals include the Laplacian of the electron density $\nabla^2\rho$ [24].

The more recent idea is the work of Becke in 1993 [25] which adds some contribution of exchange energy of Hartree-Fock to the exchange-correlation functional. This group of functionals are called Hybrid functionals.

Not to mention, there is some recent developments of functionals using the generalized random phase approximation [26, 27].

We close the section with an illustration of accuracy for different types of functionals known as Jacob's ladder in quantum chemistry as discussed in [24]. We can summarize the work of Perdew in the schematic illustration in Fig.1.2. In Hartree land we do not consider any exchange-correlation for the electrons. In the first step of the ladder, we add exchange-correlation and as we climb up the ladder we add more and more accuracy to our exchange-correlation functional. But keep in mind the higher we climb the more time consuming our calculations will be. In the end, one should optimize accuracy versus computational cost. There is much more to say about exchange-correlation functionals [28, 22].

1.2.2 Basis sets

The next term in equation 1.16 that we investigate in more depth is the wave function of a single electron, Ψ_i. In order to have efficiency in solving the Kohn-Sham equation by computers, we will try to have some algebraic equations instead of partial differential ones. To that end, we state the single electron wave function as a linear composition of an arbitrary basis set as

$$\Psi_i(\mathbf{r}) = \sum_{\mu=1}^{\infty} c_\mu^i \Phi_\mu(\mathbf{r}), \tag{1.18}$$

where c_μ^i are molecular orbital expansion coefficients and Φ_μ are basis functions. In practice, we do not expand to an infinite number of basis functions. Eventually, for any given problem there is an optimized number of basis sets which meets the accuracy needed to extract electronic properties of the system.

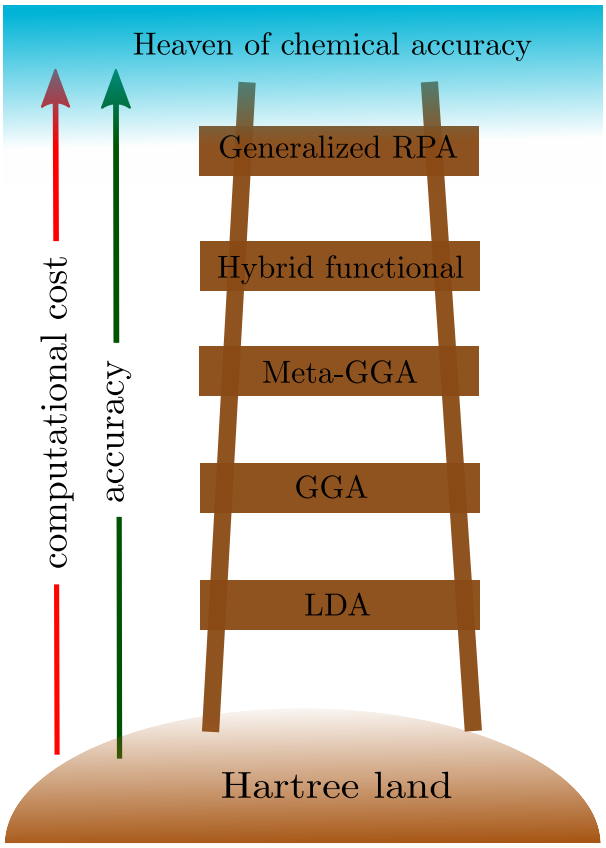

Figure 1.2: Illustration of Jacob's ladder, using different types of exchange-correlation functional

Therefore, solving equation 1.16 reduces to a general eigenvalue problem as below

$$\sum_{\mu} \left(H^{KS}_{\nu\mu} - \epsilon_i S_{\nu\mu} \right) c^i_{\mu} = 0, \tag{1.19}$$

where $H^{KS}_{\nu\mu} = \langle \Phi_\nu | \, \hat{H}^{KS} \, | \Phi_\mu \rangle$, is the Kohn-Sham Hamiltonian matrix, where Kohn-Sham Hamiltonian operator is defined as $\hat{H}^{KS} = [-\frac{1}{2}\nabla^2 + V_{ext}(\mathbf{r}) + V_H(\mathbf{r}) + V_{xc}(\mathbf{r})]$, ϵ_i is the eigenvalue corresponding to Ψ_i, and $S_{\nu\mu} = \langle \Phi_\nu | \Phi_\mu \rangle$, is the overlap matrix between the basis functions.

Carrying on, we talk about electing proper basis sets for a given electronic system. In this thesis DFT calculations have been performed on metallic surfaces and organic molecules. Therefore, we have periodic structures and molecular structures. There are two main types of basis sets that are used in DFT calculations: atomic orbitals basis sets, and plane waves basis sets. Further, we introduce these two methods and their usage in our DFT calculations.

Atomic orbital basis functions are solutions to the Schrödinger equation of free atoms. When performing DFT calculations we can use Linear combination of atomic orbitals (LCAO) method to construct the single electron wavefunction. The simplest form of atomic orbital basis functions called Slater type orbitals reads

$$\Phi_{\mu,\zeta lm}(\mathbf{r}) = Y_{lm}(\Theta,\phi) r^{\mu-1} e^{-\zeta r}, \tag{1.20}$$

where $\Phi_{\mu,\zeta lm}(\mathbf{r})$ is the basis function number μ , and $Y_{lm}(\Theta,\phi)$ is the angular part of free atoms.

These basis functions are centred on atoms of the molecule, therefore the atomic positions. Additionally, they are not orthogonal. But on the other hand, using the LCAO method, a small basis set would be sufficient to describe a molecule.

In addition to the atomic orbitals basis sets that are localized, plane waves basis sets are also used in DFT calculations. These basis sets are used in calculations for periodic solids. The single electron wave function can be written as a superposition of plane waves

$$\Psi_i^K(\mathbf{r}) = \sum_{\mathbf{G}} u_i(\mathbf{G}) \exp\big(i(\mathbf{K}+\mathbf{G})\cdot\mathbf{r}\big), \tag{1.21}$$

where $\mathbf{G}$ are the reciprocal lattice vectors, $u_i(\mathbf{G})$ plane wave coefficients, and $\mathbf{K}$ and $\mathbf{r}$ are reciprocal space vector and real space vector, respectively.

This basis set is not localized in space, which makes it suitable for periodic systems. Furthermore, by adding more plane waves the calculation could systematically converge. Besides, plane waves are mathematically simple. And last but not the least, the number of plane waves that are needed to represent the single electron wave functions depends strongly on their shape. This means when constructing the wave functions for the region of core electrons and close to the nucleus, we will need millions of plane waves to describe the wave function, and this makes the calculations very computationally expensive. Fortunately, when it comes to studying condensed matter, we are more interested in the behaviour of valence electrons. Yet, the wave function is not smooth close to the core. There are two causes for this oscillation of the wave function. Firstly, the wave functions should be

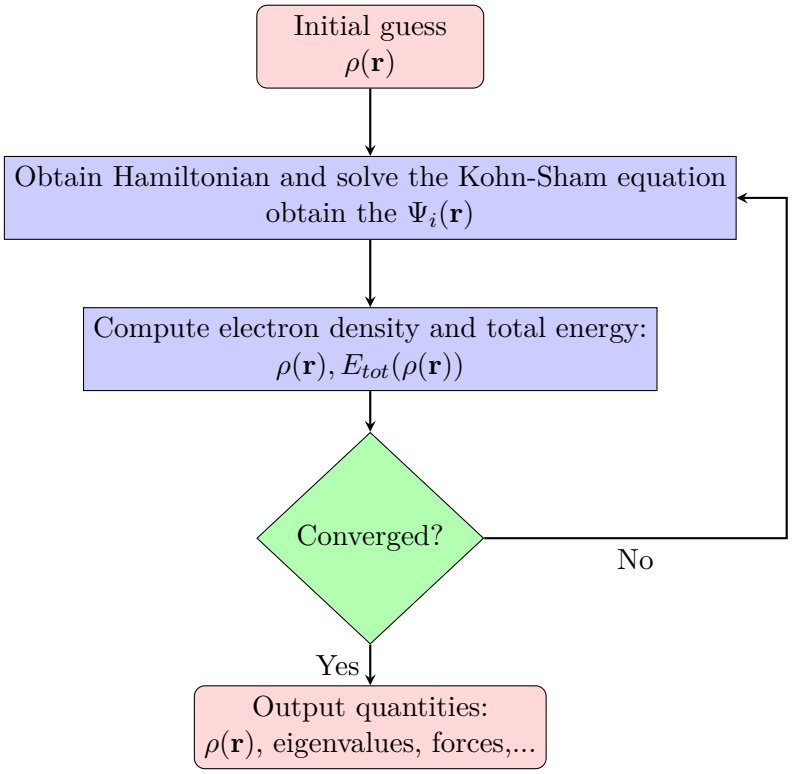

Figure 1.3: Self consistent algorithm to solve Kohn-Sham equation

orthogonal to core electron states, and secondly, there is strong Coulomb potential there. Instead, we can replace the atomic nucleus and the core electrons by an effective smooth potential. This effective potential is called pseudopotential. When implementing pseudopotential in DFT calculations, as we freeze the core electrons, we have fewer electrons in the system, Thus, the calculations are systematically faster [29, 30].

1.2.3 Solving Kohn-Sham equation

In this section as the last thing about equation 1.16, we will talk about self consistent scheme to find the ground state energy [31, 32].

To calculate the ground state energy we should do these steps:

1. Guess a trial $\rho(\mathbf{r})$.

2. Construct the Hamiltionian and solve the Kohn-Sham equation 1.16 and obtain the single electron wave functions $\Psi_i(\mathbf{r})$.

3. Calculate $\rho_{new}(\mathbf{r})$ from single electron wave function $\Big(\rho(\mathbf{r}) = \sum_{i=1}^{n} \Psi_i(\mathbf{r})\Psi_i^*(\mathbf{r})\Big)$.

4. If the difference between the new electron density and the initial electron density is less than a given threshold then stop the self consistent circle and if not put the $\rho_{new}(\mathbf{r})$ as $\rho(\mathbf{r})$ and repeat until convergence.

A flowchart of this algorithm is shown in Fig.1.3.

1.3 Density functional tight binding (DFTB)

Usually, if we want to choose a method for electronic structure calculations most probably, one will use DFT. The size of the DFT community shows the efficiency and accuracy of this theory. Yet, as we go to larger systems with a larger number of atoms, the computational cost grows as μ^3 with respect to the number of basis functions, μ [33]. Additionally, when going to larger time scale the DFT calculations become computationally demanding. In this part DFTB which is an approximation method based on density functional theory, is introduced. Since it holds on to DFT and quantum description, it is not an empirical method. To describe the core-core interaction atomic short-range repulsion energy is introduced which is an analytical expression fitted to ab initio interactions between atoms [34, 35, 36]. Yet, we have to keep in mind that DFTB is not as accurate as DFT. Additionally, we have to consider that DFTB is less transferable to systems which are beyond its fittings database. But, the DFTB method is more transferable than tight binding TB [37] method, since there are no empirical parameters. Yet, when using DFTB we do not reach the length and time scale as TB. In case of the classical force field (FF) and molecular mechanics (MM) we could reach a bigger length and time scale (μm), but with less accuracy Fig.1.4.

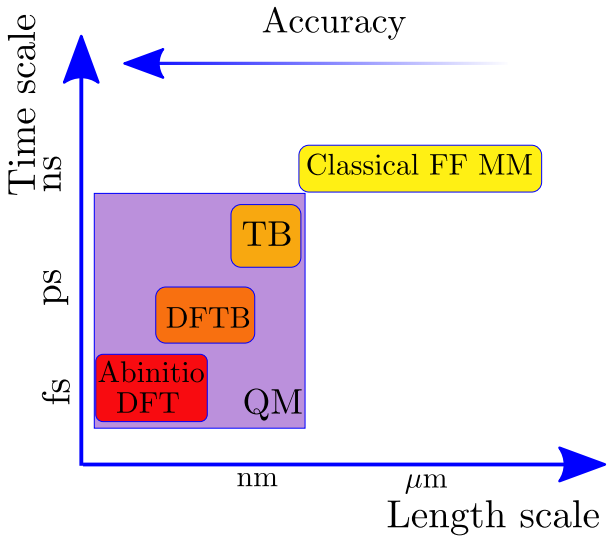

Figure 1.4: Time scale vs. length scale for quantum mechanic (QM) calculations (density functional theory (Ab initio DFT), density functional based tight binding (DFTB), tight binding (TB)), classical force field (FF) and classical molecular mechanic (MM)

In principle, DFTB is a Taylor expansion of the Kohn-Sham total energy around a convenient electron density $\rho_0(\mathbf{r})$. To that end, we assume a system of independent neutral atoms. Then we consider a density $\rho_0(\mathbf{r})$ correspond to this system. This density does not include any charge transfer. We know that this is not the density which minimizes the energy functional but we introduce

$$\delta\rho(\mathbf{r}) = \rho(\mathbf{r}) - \rho_0(\mathbf{r}), \tag{1.22}$$

where $\rho(\mathbf{r})$ minimizes the energy functional and $\delta\rho(\mathbf{r})$ is a small electron density fluctuation. The approach in DFTB is to write molecular potentials and basis functions as compositions of Slater type functions. These Slater type functions are obtained self-consistently for neutral atoms. In this thesis, we used the self consistent charge density functional tight binding (SCC-DFTB) or DFTB2 up to the second order energy expansion. The next section is on the derivation of SCC-DFTB from DFT [36].

1.3.1 Self consistent charge density functional tight binding (SCC-DFTB)

As we discussed in previous sections in DFT, we write the total energy of the electronic system in terms of the electron density. The total energy of a solid containing electrons and nucleus is the total energy of electrons plus the repulsive energy of all nucleus [38].

Carrying on, we expand the total energy at $\rho(\mathbf{r})$ to second order in fluctuation, $\delta\rho(\mathbf{r})$, the total energy emerges as

$$\begin{aligned} E[\rho] \approx \langle\Psi_i| \sum_i \Big(-\frac{1}{2}\nabla^2 + V_{ext} + V_H[\rho_0] + V_{xc}[\rho_0]\Big) |\Psi_i\rangle \\ + \frac{1}{2}\int\int \Big(\frac{\delta^2 E_{xc}[\rho_0]}{\delta\rho(\mathbf{r})\delta\rho(\mathbf{r}')} + \frac{1}{|\mathbf{r}-\mathbf{r}'|}\Big)\delta\rho(\mathbf{r})\delta\rho(\mathbf{r}')d^3r d^3r' \\ - \frac{1}{2}\int V_H[\rho_0](\mathbf{r})\rho_0(\mathbf{r})d^3r + E_{xc}[\rho_0] - \int V_{xc}[\rho_0](\mathbf{r})\rho_0(\mathbf{r})d^3r + E_{nn}(R). \end{aligned} \tag{1.23}$$

This is the total energy expression for SCC-DFTB also known as DFTB2 [39, 40, 38]. If we expand the energy functional up to the third order of charge fluctuation, we will have what we call DFTB3 [41]. In DFTB2 and DFTB3 a self consistent charge (SCC) has been represented. The atomic charges are self-consistently determined.

Considering the repulsive energy as

$$E_{rep}[\rho_0] = -\frac{1}{2}\int V_H[\rho_0](\mathbf{r})\rho_0(\mathbf{r})d^3\mathbf{r} + E_{xc}[\rho_0] - \int V_{xc}[\rho_0](\mathbf{r})\rho_0(\mathbf{r})d^3\mathbf{r} + E_{nn}(R), \tag{1.24}$$

and the band structure energy as

$$E_{BS} = \sum_i \langle\Psi_i| H[\rho_0] |\Psi_i\rangle , \tag{1.25}$$

where $H[\rho_0] = -\frac{1}{2}\nabla^2 + V_{ext} + V_H[\rho_0] + V_{xc}[\rho_0]$, we could write the total energy from equation 1.23 as

$$E[\rho] = E_{BS}[\rho_0] + E_{rep}[\rho_0] + E^2[\delta\rho, \rho_0], \tag{1.26}$$

where $E^2[\delta\rho, \rho_0]$ contains all the terms that depend on second order density fluctuation

$$E^2[\delta\rho, \rho_0] = \frac{1}{2}\int\int \Big(\frac{\delta^2 E_{xc}[\rho_0]}{\delta\rho\delta(\mathbf{r})\rho(\mathbf{r}')} + \frac{1}{|\mathbf{r}-\mathbf{r}'|}\Big)\delta\rho(\mathbf{r})\delta\rho(\mathbf{r}')d^3r d^3r'. \tag{1.27}$$

From here we talk about each term in equation 1.26.

To compute the band structure energy we expand the single electron wave function in the basis of atomic orbitals (section 1.2.2). Having said that we rephrase E_{BS}

$$E_{BS} = \sum_i \sum_{\mu\nu} c_\mu^{i*} c_\nu^i H_{\mu\nu}^0, \tag{1.28}$$

where $H^0 = H[\rho_0]$, and $H_{\mu\nu}^0 = \langle\phi_\mu| H^0[\rho_0] |\phi_\nu\rangle$. These integrals are computed for the system consisting of neutral atoms and are tabulated as a function of the distance between two centers. It should be noted that the three center terms are neglected. In order to compute Hamiltonian matrix elements in two centre representation, we decompose the electron density of the Kohn-Sham system into atomic contributions [38]. Not to mention, in order to calculate overlap integrals and Hamiltonian elements the Slater-Koster transformation rules are used [37].

To compute the repulsive energy term it is assumed to be pairwise [34]. Correspondingly, the repulsive term converts to

$$E_{rep} = \sum_{I<J} V_{rep}^{IJ}(R_{IJ}), \tag{1.29}$$

where $R_{IJ} = R_I - R_J$ is the distance between atom I and J and $V_{rep}^{IJ}(R_{IJ})$ is the repulsive potential which is derived from DFT calculations. A set of reference molecules are chosen. For each molecule, the energy difference between DFT total energy and band structure energy E_{BS} have been calculated as a function of bond length. These parameters along with Hamiltonian and overlap matrices have been tabulated in some files named Slater-Koster files in the DFTB+ package, so as a user we will not need to do the parameterizations.

The last term in equation 1.26 depends on second order density fluctuations. Forthwith, rather than computing double integrals, assume a whole space V is filled with

V_I which is the volume related to atom number I. Hence, computing double integrals in the continuous space V reduces to compositions of the functions in V_I of each atoms [38, 42, 43, 44]. Therefore, the charge fluctuation is composed of atomic contributions. Consequently, this energy term could be written pairwise as

$$E^2[\delta\rho, \rho_0] = \frac{1}{2}\sum_{IJ}\gamma_{IJ}(R_{IJ})\Delta q_I \Delta q_J, \tag{1.30}$$

where γ_{IJ} is approximated to a function that depends on interatomic distances, For $I = J$ it tends towards the Hubbard parameter for atom I [34]. Then, Δq_I are net atomic charges, which are obtained using Mulliken charge analysis [45]. All in all, we can write the total energy

$$E = \sum_i \sum_{\mu\nu} c_\mu^{i*} c_\nu^i H_{\mu\nu}^0 + \frac{1}{2}\sum_{IJ}\gamma_{IJ}\Big(R_{IJ}\Big)\Delta q_I \Delta q_J + \sum_{I<J} V_{rep}^{IJ}\Big(R_{IJ}\Big). \tag{1.31}$$

Instantly, the problem reduces to minimize the energy from equation 1.31. We discuss this in the next section 1.3.2.

1.3.2 Secular equation in DFTB and self consistent solution

In this section we try to solve equation 1.31. To that end, using the variational principle method of Lagrange multipliers, we obtain

$$\frac{\partial}{\partial c_\mu^i}\Big(E_- \sum_i \lambda_i (\sum_\mu \sum_\nu c_\mu^i c_\nu^i S_{\mu\nu})\Big) = 0, \tag{1.32}$$

where λ_i are unknown Lagrange multipliers. Immediately, the equation for coefficients c_μ^i reads

$$\sum_\nu c_\nu^i (H_{\mu\nu} - \lambda_i S_{\mu\nu}) = 0, \tag{1.33}$$

where

$$H_{\mu\nu} = H_{\mu\nu}^0 + \frac{1}{2} S_{\mu\nu} \sum_K (\gamma_{IK} + \gamma_{JK})\Delta q_K, \quad \mu \in I \quad \nu \in J. \tag{1.34}$$

Equation 1.33 is called the DFTB secular equation and is the equivalent of the Kohn-Sham equation in DFTB. Moreover, it should be noted λ_i, the unknown Lagrange multipliers, are the eigenvalues of this equation.

Equations 1.33 and 1.34 can be solved using self-consistent method.

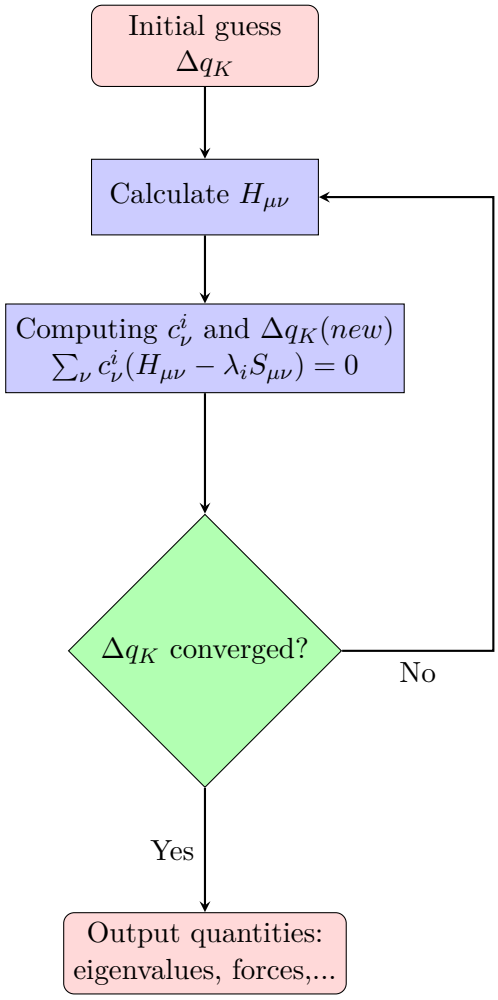

Figure 1.5: SCC-DFTB algorithm

- Firstly, the net atomic chargers $\Delta q_K = 0$ are set to zero.
- Secondly, $H_{\mu\nu}$ is computed from 1.34.
- Thirdly, having $H_{\mu\nu}$ and using equation 1.33 we obtain c^i_ν coefficients and a new Δq_K .
- Lastly, we continue this cycle until the $\Delta q_K(new) - \Delta q_K$ is smaller than a given threshold.

To give an illustration to this algorithm, look at Fig.1.5.

1.4 Electronic transport in mesoscopic scale

The aim in this section is investigating the transport properties of nanostructures. When a voltage is applied to a conductor, a current proportional to the applied voltage is produced. The constant of this proportionality is the electronic conductance which is a key parameter in the analysis of transport properties. For a macroscopic conductor, Ohm's law describes the electronic conductance

$$G = \frac{\sigma W}{L}, \tag{1.35}$$

where G is the value of conductance, σ is the electronic conductivity and is a material-dependent parameter, L and W are the length and width of the sample, respectively. However, in the atomic scale, quantum effects become important, therefore, Ohm's law is no longer valid.

To compute the conductance of a mesoscopic system, one needs to carefully determine the transport regime according to the length scale of the system of interest. A crucial length scale is a phase coherent length L_ϕ, which is the mean distance between two inelastic collisions of electrons. If $L < L_\phi$, where L is the length of the sample, one is in the mesoscopic regime. Another critical length scale is the electron mean free path, l_{el}, which is the mean distance between two elastic collisions of electrons. When $L \gg l_{el}$, the transport regime is called diffusive. On the other hand, when $L < l_{el}$ the transport regime is ballistic, where electrons are only scattered by the sample boundaries.Hence, the physics of electron transmission is quantum and can not be described by classical mechanics. In the next subsections, the objective is to compute the conductance in the ballistic regime based on microscopic principles.

1.4.1 Ballistic regime: the Landauer-Büttiker formalism

We shall introduce the Landauer-Büttiker formalism to compute quantum coherent conductance at the microscopic scale [46]. The heart of this approach is that if

there are no inelastic collisions, then one can relate all the transport properties to the probability of electrons transmitting through the system. In other words, as Landauer said himself: "conductance is transmission" [46]. Thus, the conductance at energy E for a system in the ballistic regime reads

$$G(E) = \frac{2e^2}{h}\tau(E), \tag{1.36}$$

where h is Planck's constant and $\tau(E)$ is the transmission function of the system at energy E, which is the probability of an electron with energy E transmitting from one end of the system to the second end. Furthermore, $G_0 = \frac{2e^2}{h} \sim (12.9k\Omega)^{-1}$, is defined as the quantum of conductance. So, if a mode has a perfect transmission the conductance of that mode will be exactly one conductance quantum. All in all, to compute conductance, one should solve the Schrödinger equation 1.1, extract all the eigenmodes, and calculate the transmission for each mode. Then one should do a summation over all the modes and add those together to reach the total transmission.

In practice, the sample is connected to two electrodes (or leads) and grants us to insert current or voltage (Fig.1.6). The conductor is the molecule plus an arbitrary number of layers of the electrodes. These arbitrary layers are necessary to ensure that charge density is changing smoothly at the boundaries of the conductor/lead, so we can consider the leads bulk-like. When the leads are showing bulk-like properties, in thermal equilibrium, they behave as ideal electron reservoirs, with a well defined temperature and chemical potential [47, 48]. The lead with the smaller chemical potential is referred to as collector lead. The idea in the scattering approach is to relate all the transport properties to transmission probabilities. The electron is preserved (and not scattered) in the whole conductor and it scatters only at boundaries with the electron reservoirs. Inside the reservoirs, the electrons are in thermal equilibrium, thus, they have the same temperature as the leads. We compute the transmission of each eigenmodes for the system we described. Thus,

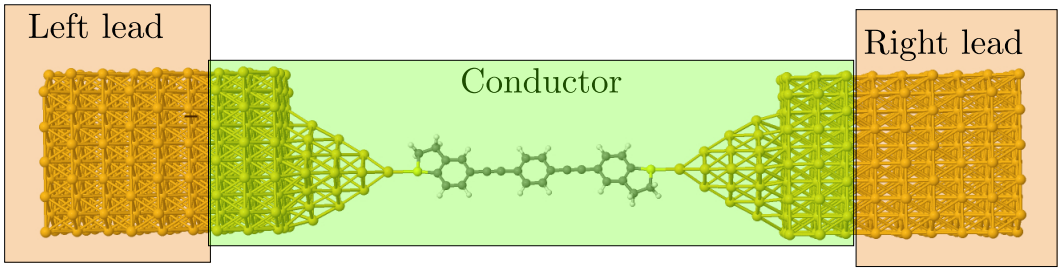

Figure 1.6: The system used in the ballistic regime. The conductor is connected to two leads. The leads are considered semi-infinite. The colours on the lead and conductor region are used as a visual guide only.

the conductance reads

$$G = \frac{2e^2}{h} \int_{-\infty}^{\infty} dE\tau(E)(E-\mu)\Big(-\frac{\partial f(E,\mu)}{\partial E}\Big), \tag{1.37}$$

where μ is the chemical potential of the leads, and $f(E,\mu)$ is the Fermi-Dirac distribution for the electrons defined as

$$f(E) = (e^{(E-\mu)/k_BT} + 1)^{-1}. \tag{1.38}$$

Eventually, applying a voltage to the two end of the system causes a difference in energy levels of the two leads, so we will have different values for the chemical potential (assume $\mu_L < \mu_R$). Consequently, an electrical current will appear which reads

$$I = \frac{2e}{h} \int_{-\infty}^{\infty} dE\tau(E)[f_L(E,\mu_L) - f_R(E,\mu_R)], \tag{1.39}$$

where $f_L(E,\mu_L)$ and $f_R(E,\mu_R)$ are the Fermi-Dirac distribution in the left and right lead, respectively [46, 49].

Instantly, our problem reduces to find the transmission function to calculate the transport properties of the system. We can derive the transmission from Green's functions. The Green's function is a powerful tool which predicts us the response at any point (inside or outside of the conductor) due to an unitary excitation at the origin. Regardless of mathematical complexity, the Non-Equilibrium Green's Function method (NEGF) has gained popularity[50].

1.4.1.1 Non-Equilibrium Green's Function method

When solving the transport problem, we can not assume local thermodynamic equilibrium, since the global Fermi energy is not defined. But we can assume that the leads have different chemical potential and are large enough so the electrons are locally in equilibrium [47]. Both leads to be at equilibrium, the transmission function in terms of Green's function is [51]

$$\tau(E) = Tr(\Gamma_L(E)G^r(E)\Gamma_R(E)G^{r\dagger}(E)), \tag{1.40}$$

where G^r and $(G^r)^\dagger$ are retarded and advanced Green's functions which read

$$\begin{aligned} G^r &= [ES - H - \Sigma^r]^{-1} \\ G^{r\dagger} &= [ES - H - \Sigma^{r\dagger}]^{-1}, \end{aligned} \tag{1.41}$$

where Σ^r is the retarded self energy due to the interactions with the right lead, $\Sigma^{r\dagger}$ is the advanced self energy due to the interactions with the leads, H is the Hamiltonian of the conductor, and S is the overlap matrix in the conductor. $\Gamma_{\{L,R\}}$ are the coupling of the conductor with the left L and right R lead, and reads

$$\Gamma_{L,R}(E) = i[\Sigma^r_{L,R}(E) - \Sigma^{r\dagger}_{L,R}(E)]. \tag{1.42}$$

We could write the density matrix as below

$$\rho = \frac{1}{2\pi i}\int_{-\infty}^{\infty} dE G^<(E), \tag{1.43}$$

where $G^<(E)$ is the electron–electron correlation matrix, and it depends on the density of occupied states [47]. The electron–electron correlation matrix can be written as a function of the retarded Green's function. The electron–electron correlation matrix has been calculated by kinetic (KKB) equation [52]

$$G^{<,>}(E) = G^r(E)\Sigma^{r,r\dagger}(E)G^{r\dagger}(E), \tag{1.44}$$

where $G^>$ in contrast to $G^<$ is the part of electron–electron correlation matrix that depends on the density of unoccupied states. When calculating the density matrix

it is more convenient to write $G^<$ as a composition of three terms. So the electron density can be written as

$$\rho = \int_{-\infty}^{\infty} dE f_C(E) G^r(E) - \int_{-\infty}^{\infty} dE f_C(E) G^{r\dagger}(E) + \sum_{\alpha=L,R} \int_{-\infty}^{\infty} dE [f_\alpha(E) - f_C(E)] G^r(E) \Gamma_\alpha(E) G^{r\dagger}(E), \tag{1.45}$$

where $f_C(E)$ is the Fermi-Dirac distributions for the collector lead , and $f_\alpha(E)$ is the Fermi-Dirac distributions for the leads [47]. Equation 1.41 and 1.45 can be solved self consistently. As stated in equation 1.41, in order to calculate the Green's function we need the Hamiltonian [53]. Thus, we could give an initial value to electron density and calculate the Hamiltonian from the SCC-DFTB method. Afterwards, using equation 1.41 the Green's functions are computed. Having the Green's functions and using equation 1.45, a new value for electron density is obtained. We repeat this cycle until the electron density is converged. Having the converged electron density, one can obtain the Green's functions for the last time and compute the transmission function [52]. For an illustration look at Fig.1.7.

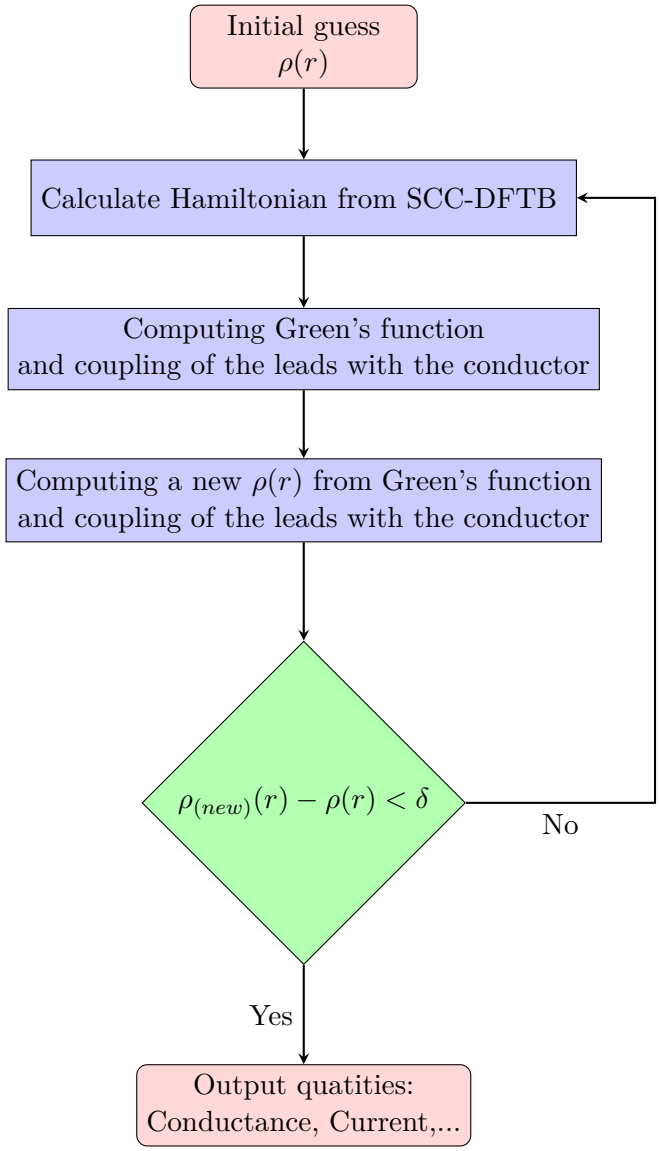

Figure 1.7: Self consistent algorithm in NEGF-DFTB method where δ is a given threshold

Chapter 2

Phonons in molecular systems

"Everything that living things do can be understood in terms of the jiggling and wiggling of atoms."

— Richard Feynman

2.1 Molecular dynamic simulations

To simulate the equilibrium and transport properties of a classical many-body solid, Molecular Dynamic (MD) method is traditionally used. In a lot of aspects, a MD simulation is similar to an experiment. In an experiment, we first set up the system. Afterwards, we set up the measurement tools and do the measurement for the property of interest during a certain time interval. In the presence of statistical noises, which is very likely, we will do an average over a longer time. In a simulation, first, we set up the molecular system with N classical particles. Then, we let the system equilibrate applying Newton's equation of motion until the properties of interest do not change over time. And at last, we run the measurement. The way to compute errors in the experiment and molecular dynamic simulation are similar, as well. The examples of errors, we may not prepare the system correctly. We may measure a given property before the system reaches an equilibrium state. In a way, we could say when running MD calculations, we are experimenting on a computer [54]. After solving Newton's equation of motion (section 2.1.2), the trajectories of

each atom is known. To measure any property of the system, we will need to write the observable in terms of positions and momentum of the particles [55].

In MD simulation, we set up the system of N particles by giving a mass, a position and a velocity. Then, we numerically solve the time-dependent Newton's equation of motion [56]

$$M_I \frac{d^2\mathbf{R}_I}{dt^2} = -\frac{\partial V(R)}{\partial \mathbf{R}_I}, \tag{2.1}$$

where M_I, $\mathbf{R_I}$ and $V(R)$, are mass of the particle $I(I = 1, ..., N)$, the position vector of atom I, and the inter-atomic potential, respectively. The inter-atomic potential can be written as summation of individual atoms, pairs, triplets and so on [57]

$$V = \sum_I v_1(R_I) + \sum_I \sum_{J>I} v_2(R_I, R_J) + \sum_I \sum_{J>I} \sum_{K>J} v_3(R_I, R_J, R_K) + ..., \tag{2.2}$$

where the condition $J > I$ is to prevent counting any pair twice, v_1 corresponds to the effect of an external field. The next terms represent particle interactions, v_2 is the pair potential, v_3 is the triplet potential, etc. Not to mention, for an isotropic system, the pair potential coefficient depends only on the distance between the two atom, $\mathbf{R}_{IJ} = |\mathbf{R}_I - \mathbf{R}_J|$, so that it can be written as $v_2(R_{IJ})$. The pair potential includes a repulsive term at short distances, due to overlap between the electron clouds. The triple part of the potential (v_3) becomes important when it comes to liquid densities.

The potentials used in computer simulations are most of the time approximated by effective pair potentials which represent all the many-body effects and need to reproduce the experimental data. We introduce now a commonly used pair potential in computer simulations. This potential which is a simple Lennard-Jones 12–6 potential describes most notable features of real pairwise interactions [58]

$$V(R_{IJ}) = 4\epsilon\left(\left(\frac{\sigma}{R_{IJ}}\right)^{12} - \left(\frac{\sigma}{R_{IJ}}\right)^{6}\right), \tag{2.3}$$

where ϵ is the depth of potential wall defined as 'dispersion energy', and σ is the distance which the pairwise potential is zero. The potential has a long-range dipole-dipole attraction part and a repulsive wall (due to Pauli repulsion) at distances less

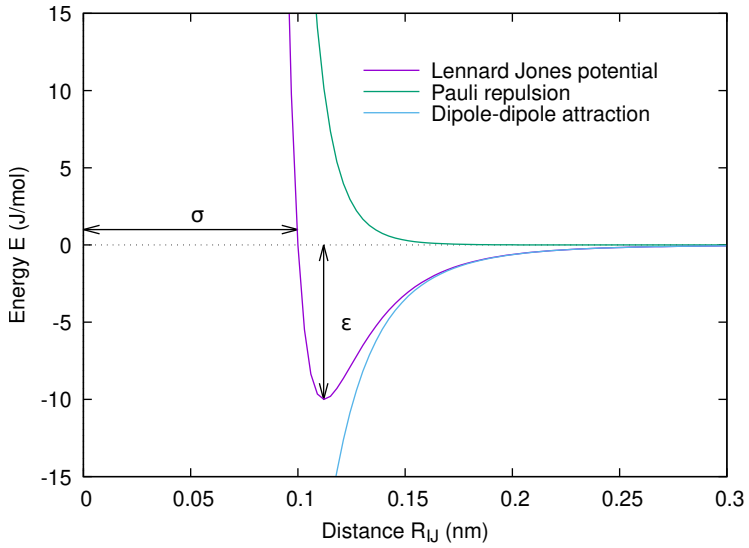

Figure 2.1: Illustration of the Lennard-Jones pair potential

than $R_{IJ} \sim \sigma$. Figure 2.1 represents the Lennard-Jones potential as a function of the pair distance. One of the estimation for pair potential among two argon atoms as a function of the distance which was fitted on ab initio calculations of argon dimer has been shown a very good agreement with Lennard-Jones approximation for pair potential [59].

2.1.1 Force field in molecular dynamic calculations

In MD simulations, empirical force field is traditionally employed to describe the interactions in complex molecular system. Force field approximates the forces between atoms within molecules called intra-molecular interactions and the forces between the molecules called inter-molecular interactions. When developing a force field for a molecular system, there are different type of atoms to consider and several intra-molecular and inter-molecular potential parameters to fit. One can build the force field from ab initio calculations. Fortunately, the parametrization of different types of force fields has been done over the last 50 years for most atoms [60, 61, 62, 63, 64]. The force fields are a collection of equations and constants fitted to the experiment or ab initio calculations to reproduce the configuration

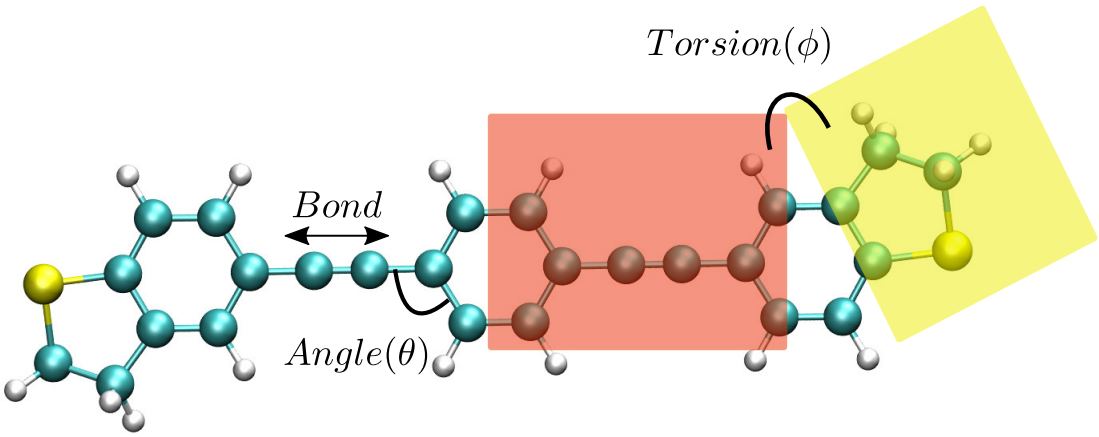

Figure 2.2: A schematic illustration of a molecule in MD calculations

and structural properties of reference molecules. In MD, a molecule is described as some charged points (atoms) linked by springs (bonds) to their first neighbours as shown in Fig.2.2. In addition to these bonded interactions, there is van der Waals and electrostatic interactions between atoms [65]. In this thesis we used Assisted Model Building with Energy Refinement (AMBER) [63, 66] and Optimized Potentials for Liquid Simulations (OPLS) [64, 67] force fields. These force fields share a common functional form [68]

$$V(R) = \sum_{bonds} k_r(R_{IJ} - R_{eq})^2 + \sum_{angles} k_\theta(\theta - \theta_{eq})^2 + \sum_{torsions} \sum_{f} k_{\phi,f}\Big(1 + \cos\left(f\phi\right)\Big) + \sum_{I} \sum_{J>I} \left[\frac{q_I q_J}{R_{IJ}} + 4\epsilon\left(\left(\frac{\sigma}{R_{IJ}}\right)^{12} - \left(\frac{\sigma}{R_{IJ}}\right)^{6}\right)\right], \tag{2.4}$$

where k_r is the elastic constant of the bonds, R_{eq} is the equilibrium bond length between two atoms, k_θ is elastic constant for angles, θ_{eq} is the angle between two atoms in equilibrium, f is the number of torsion degrees of freedom, $k_{\phi,f}$ is elastic constant for torsion, and $q_{\{I,J\}}$ are the electronic charge of atom I and J, respectively. In practice, k_r, R_{eq}, k_θ, and θ_{eq} are fitted to vibrational frequencies data of molecular fragments which belong to proteins and nucleic acids [69]. The torsion parameters were fitted such that they reproduce the structural properties of small model compounds. Hence, a torsion parameter is optimized for simple structures

and applied to large molecules. This makes the force field more transferable [64]. The last term in equation 2.4 is the intra-molecular interaction containing Coulomb energy and Lennard-Jones potential.

2.1.2 Solving the equations of motion

Once the choice of the force field has been done, one needs to solve the equations of motion 2.1 to obtain the trajectory of the system in time. Starting from a physical initial state for positions and velocities in which the system is in equilibrium, we can use Verlet algorithm [56] to predict how the atomic positions and velocities evolve during time. Having the position at time t and $t - dt$, the Verlet algorithm predicts the position at time $t + dt$

$$\mathbf{R}_I(t + dt) = 2\mathbf{R}_I(t) - \mathbf{R}_I(t - dt) + \frac{d^2\mathbf{R}_I(t)}{dt^2}dt^2 + \mathcal{O}(dt^4), \tag{2.5}$$

where dt is small as such we can expand $\mathbf{R}_I(t + dt)$ around it, and $\mathcal{O}(dt^4)$ means we are neglecting all the terms after the third order of the expansion. Similarly, the velocity is computed as below:

$$\mathbf{v}_I(t) = \frac{\mathbf{R}_I(t + dt) - \mathbf{R}_I(t - dt)}{2dt} + \mathcal{O}(dt^2), \tag{2.6}$$

where $\mathbf{v}_I(t)$ is the velocity of atom I at time t, $\mathcal{O}(dt^2)$ means we are neglecting all the terms after the first order of the expansion [70]. In our simulations it is important to compute accurately the kinetic energy of the system, since it is directly related to the system temperature. Hence, we will need to compute the velocities more accurately. In order to gain accuracy in the determination of the velocity, Velocity Verlet algorithm [71] predicts the position at time $t + dt$

$$\mathbf{R}_I(t + dt) = \mathbf{R}_I(t) + \mathbf{v_I}(t)dt + \frac{1}{2}\frac{d^2\mathbf{R}_I(t)}{dt^2}dt^2 + \mathcal{O}(dt^3), \tag{2.7}$$

and velocity at time $t + dt$

$$\mathbf{v}_I(t + dt) = \mathbf{v_I}(t) + \frac{1}{2}\left(\frac{d^2\mathbf{R}_I(t)}{dt^2} + \frac{d^2\mathbf{R}_I(t + dt)}{dt^2}\right)dt + \mathcal{O}(dt^2). \tag{2.8}$$

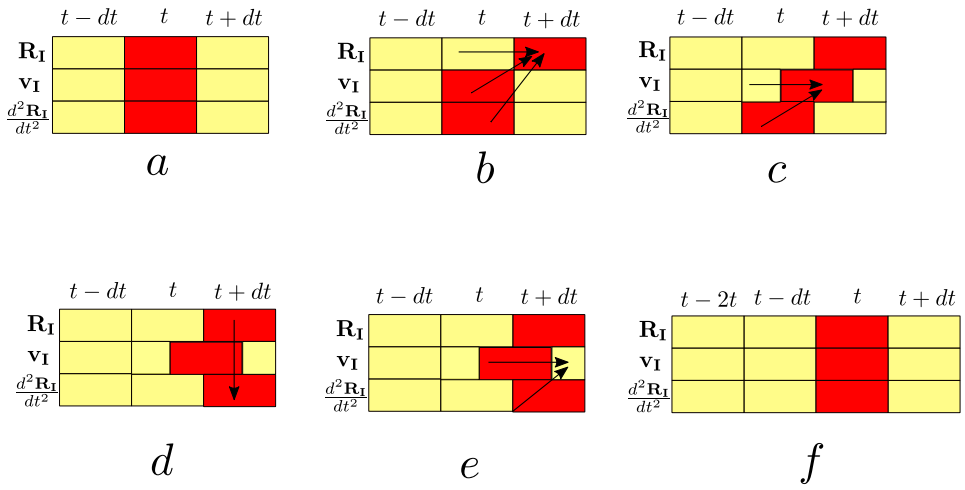

Figure 2.3: Schematic illustration of the velocity Verlet algorithm a) Give current position, velocity, and force b) Compute new positions c) Compute velocity at half step d) Compute forces at new position e) Compute velocity at full step f) Advance to next time step, repeat.

As illustrated in Fig.2.3 the first step of this algorithm is to give initial values to the positions, velocities and forces to all the atoms. Then we update the positions at time $t + dt$ from equation 2.7. The velocity update takes two steps, first, the velocity is computed at time $t + \frac{1}{2}dt$ using the forces at time t, then the forces are computed at time $t + dt$ and used to update the velocities at time $t + dt$. The value of the time step dt depends on the problem considered. A larger time step needs less computational time, however, it should be noted that the time step should ensure that the dynamic properties of the system which have the highest frequencies are well described. Moreover, the total energy of the system should be conserved during the calculation.

2.1.3 Initial state

To insure stability during MD calculations, it is crucial to start from a physical initial state. For solids, one can start from the equilibrium solid state positions, where there are no forces on the individual atoms and the whole system. To start the dynamics in the MD system, atoms should have initial velocities in random

directions consistent with the desired temperature. One can sample the velocities from a Maxwell-Boltzmann distribution as below

$$f(\mathbf{v}_I) = \left(\frac{M_I}{2\pi k_B T}\right)^{1/2} e^{-M_I \mathbf{v}_I^2/2k_B T}, \tag{2.9}$$

where k_B is the Boltzmann constant, and T is the desired temperature of the MD calculation. Maxwell derived this distribution in 1860 and later Boltzmann investigated its physical origins [72, 73]. The distribution can be derived from the state that maximizes the system entropy. At first, this distribution was used to describe atom velocities in ideal gases, where they move freely in a box without any interaction but some elastic collisions, which during that they exchange energy and momentum in thermal equilibrium [74].

2.1.4 Periodic boundary condition

The conventional MD simulation system sizes are limited to a few hundred nanometers. As a consequence of this limitation, the properties of the simulated system will be affected by finite size effects. To overcome this situation, Periodic boundary conditions (PBC) [75] are commonly used. As shown in Fig.2.4, the central unit cell is replicated throughout two-dimensional space to create an infinite lattice. To ensure that the number of atoms in the unit cell is conserved, when an atom passes the boundary of the unit cell, its periodic images move as well (see Fig.2.4). It is crucial to investigate if the properties of the periodic system and the corresponding macroscopic system are the same. It should be noted that the minimal size of the unit cell should be larger than the range of any inter-molecular potential in the system.

To summarize this section on MD calculation, we describe the MD algorithm [76] in Fig.2.5.

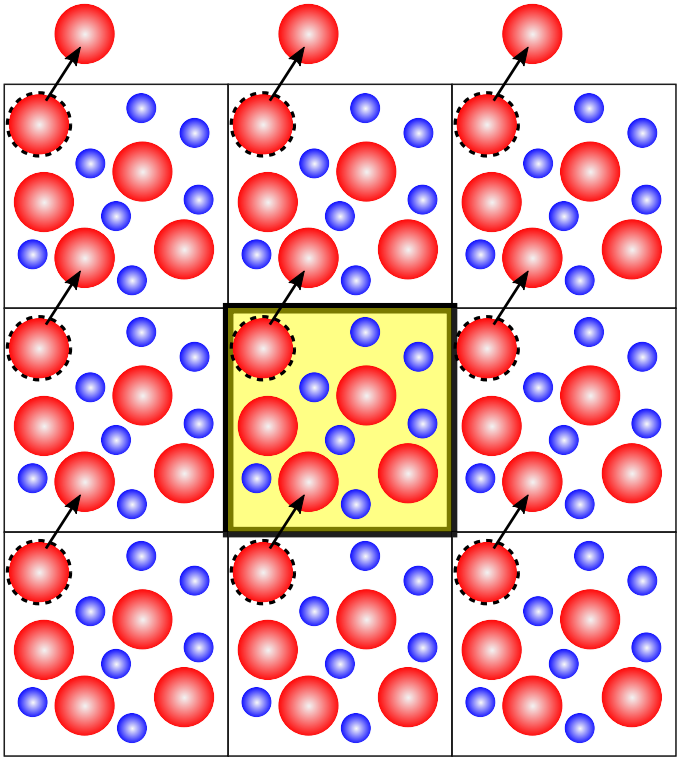

Figure 2.4: A two-dimensional periodic system in MD. Atoms and molecules can enter and leave the unit cell (The unit cell is highlighted in yellow).

2.2 Thermodynamic properties in molecular dynamics

All the relevant thermodynamic properties of a classical many-body system can be computed from the dynamics of the system. Thereupon, to measure an observable, one should first express it in terms of positions and velocities of the atoms in the system. For instance, using the equipartition principle the average kinetic energy reads

$$\left\langle K \right\rangle = \frac{1}{2}\left\langle \sum_{I}^{N} M_I \mathbf{v}_I^2 \right\rangle = \frac{3}{2} N k_B T, \tag{2.10}$$

where the brackets show the average value, k_B is the Boltzmann constant, and T is the temperature. We use this equation to measure the temperature of the system in MD simulations. The instantaneous temperature oscillates as a consequence of the kinetic energy fluctuations. Another important thermodynamic quantity is the

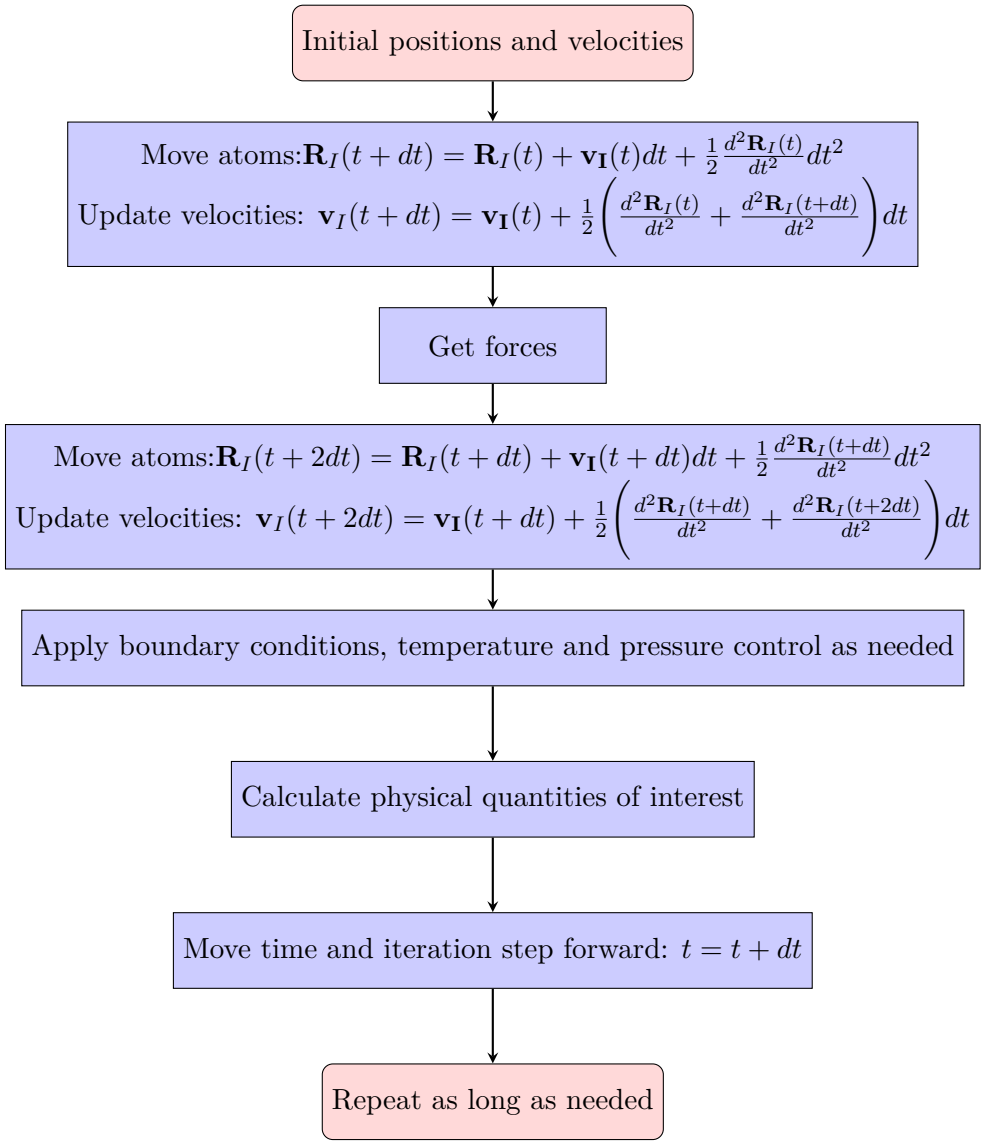

Figure 2.5: Simplified description of Molecular dynamic algorithm

pressure which can be written as:

$$P = \frac{Nk_BT}{V} + \frac{1}{3}\Big\langle \sum_{I}^{N-1}\sum_{J>I}^{N} \mathbf{R}_{IJ}.M_I\frac{d^2\mathbf{R}_{IJ}}{dt^2}\Big\rangle. \tag{2.11}$$

And last but not the least, is the total energy of the system which is the sum over kinetic energy and potential energy

$$\Big\langle E\Big\rangle = \Big\langle V\Big\rangle + \Big\langle K\Big\rangle = \Big\langle \sum_{I}^{N-1}\sum_{J>I}^{N} V(\mathbf{R}_{IJ})\Big\rangle + \frac{1}{2}\Big\langle \sum_{i}^{N} M_I\mathbf{v}_I^2\Big\rangle. \tag{2.12}$$

In MD simulations, to compute the thermodynamic properties of the system, one should wait enough to reach the equilibrium. The equilibrium conditions could

be reached with the constraint of having constant energy or temperature, constant number of atoms, constant volume or pressure. The most used ensembles are the canonical ensemble (NVT), microcanonical ensemble (NVE), and isobaric-isothermal ensemble (NPT) [77]. Nonetheless, as most of the situations of interest do not occur at equilibrium, it is convenient to measure the thermodynamic properties in NEMD state or using the so called direct method [70]. In the following, we will describe the non-equilibrium method for thermal transport problems.

2.2.1 Non-equilibrium molecular dynamic (NEMD) steady state method

In this section, the direct method for measuring thermal conductance is briefly described [78]. Assume a system of two solid slabs which are connected by a molecule. A temperature difference ΔT is applied across the system as shown in Fig.2.6. The slab which has the higher temperature is called hot wall and the slab which has the less temperature is called cold wall. In this method, the temperatures of the hot wall and the cold wall are restrained at $T + \Delta T$ and $T - \Delta T$ values by scaling the atomic velocities in the two walls. The thermal power exchange between the hot wall and the cold wall and this yields to a heat flux across the system

$$Q = \frac{dE}{dt}, \tag{2.13}$$

where Q is the heat flux, and E is the energy of the wall (cold or hot). The thermal conductance is the ratio of this heat flux and the applied temperature difference [79] and can be written as

$$\kappa_{ph} = \frac{Q}{\Delta T} = \frac{dE}{dt\Delta T}, \tag{2.14}$$

where κ_{ph} is the thermal conductance, and ΔT is the temperature difference [80, 70]. After a transient regime during which heat diffuses from the hot to cold wall, the system reaches a steady state, which ensures to obtain correct statistical measurements [81].

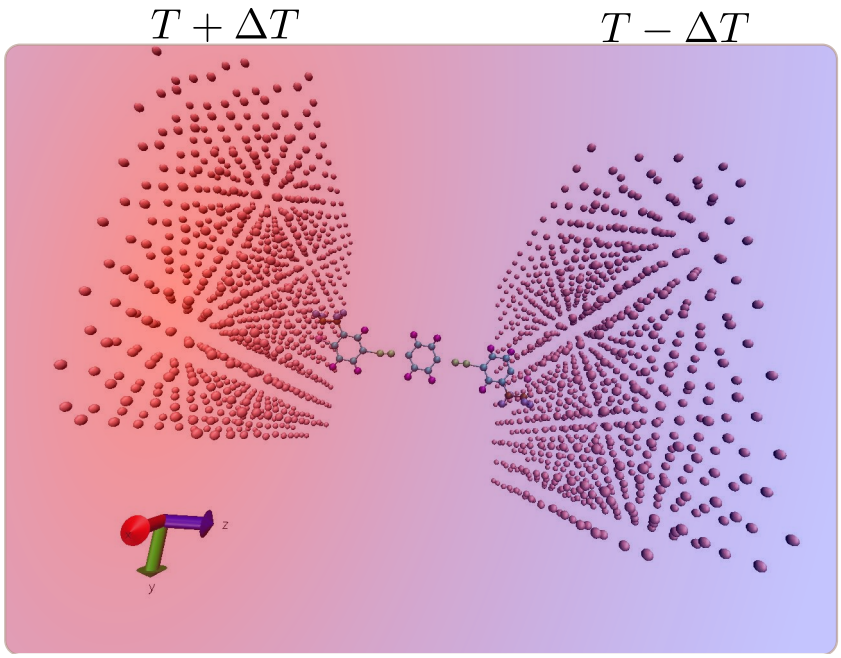

Figure 2.6: Applying a temperature difference on a system where two solid slabs are connected by a molecule. The heat flux is imposed along the z-direction

2.3 Phonons in molecular dynamic calculations

A phonon is a quantum mechanical description of a vibrational modes in a lattice, where a group of atoms is oscillating collectively at the same frequency. In classical molecular dynamics, a phonon will be translated to a vibrational normal mode. All the vibrations in the system could be described as a superposition of the vibrational normal modes [82, 83, 84]. To compute the vibrational normal modes of the system in equilibrium, in which their quantities gives rises to phonons, we expand the potential energy of the system around the equilibrium position $\mathbf{R}_I^{eq}$ where the position of atom I is $\mathbf{R}_I = \mathbf{R}_I^{eq} + u_I$. In the harmonic approximation, we have

$$V(R_I) = V_0(R_I^{eq}) + \sum_I \sum_\alpha \left.\frac{\partial V}{\partial u_{I,\alpha}}\right|_{eq} u_{I,\alpha} + \sum_{I,J} \sum_{\alpha,\beta} \left.\frac{\partial^2 V}{\partial u_{I,\alpha} \partial u_{J,\beta}}\right|_{eq} u_{I,\alpha} u_{J,\beta}, \quad (2.15)$$

where α and β are x, y, and z directions. The first term is a constant and can be safely ignored, and the second term is the forces on atoms at equilibrium and vanishes. The third term describes the interaction between atom I and J. The

term $D^{I\alpha}_{J\beta} = \frac{\partial^2 V}{\partial u_{I\alpha} \partial u_{J\beta}}$, is the dynamical matrix. We can define the matrix

$$D_{\alpha\beta}(\mathbf{q}) = \sum_{IJ} \frac{\partial^2 V}{\partial u_{I\alpha} \partial u_{J\beta}} \exp\Big(i\mathbf{q}.(\mathbf{R_I} - \mathbf{R_J})\Big), \tag{2.16}$$

where the normal modes are given by the equation

$$D_{\alpha\beta}(\mathbf{q}) e_\beta = \omega^2_{\mathbf{q}} e_\beta, \tag{2.17}$$

where $u_{I\alpha}(\mathbf{R}, t) = \sum_{\mathbf{q}} e_\alpha(\mathbf{q}) \exp^{i(\omega(\mathbf{q})t - \mathbf{q}.\mathbf{R})}$, $\mathbf{q}$ is any wave vector, e_β is the eigen vectors and $\omega^2_{\mathbf{q}}$ are the eigen values. The elements of the dynamical matrix are classically equivalent to spring constants between the atoms and are used to compute the phonon spectrum. The higher terms that are neglected in the harmonic approximation will produce the effect of phonon-phonon interaction. The dynamical matrix plays a crucial role to obtain, vibrational modes, frequencies, and mode shapes, therefore, mapping the system from real space coordinates to phonon space coordinates [82]. This calculation using the dynamical matrix is called harmonic lattice dynamics [85]. Harmonic lattice dynamics calculations are just valid at zero temperature, where the vibrational normal modes are harmonic. The anharmonicity which comes from finite temperature causes interactions between vibrational normal modes, which leads to thermal expansion and finite thermal conductivity. However, if the anharmonicity is not too strong, if we use the finite temperature lattice constant along with harmonic lattice dynamics calculations, we can provide a convenient description of the phonon dispersion of the system [86, 87].

2.3.1 Lattice dynamics calculations

Lattice dynamics calculations are employed to obtain the normal modes of a solid. The goal is to calculate the frequency of each phonon as a function of its wavevector which is called phonon dispersion. In this section lattice dynamic calculations for a one dimensional di-atomic system is presented [85, 88, 89]. Consider a one dimensional system with two different types of atom as shown in Fig.2.7. K and k are the elastic constants of the different bonds, U_N and u_N are the displacement

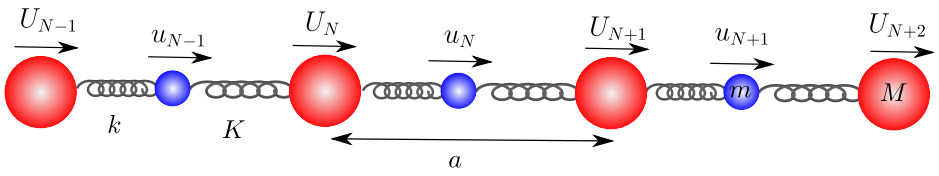

Figure 2.7: Diatomic linear harmonic chain considered in harmonic approximation

of the N-th atom with mass M and m, respectively, and a is the lattice vector at equilibrium. As the displacements are usually a few percent of inter atomic distance, the harmonic approximation is used. Moreover, only the nearest neighbour interactions are considered.

The total harmonic energy in this model is given as

$$E = \frac{1}{2}\sum_N K(U_N - u_N)^2 + k(u_{N-1} - U_N)^2. \tag{2.18}$$

Considering nearest neighbour interactions, the equation of motion for N-th atom with mass M becomes

$$M\frac{d^2U_N}{dt^2} = -\frac{\partial E}{\partial U_N} = -(K+k)U_N + ku_{N-1} + Ku_N, \tag{2.19}$$

and for the N-th atom with mass m is

$$m\frac{d^2u_N}{dt^2} = -\frac{\partial E}{\partial u_N} = -(K+k)u_N + kU_{N-1} + KU_N. \tag{2.20}$$

The solution to the harmonic equation of motion is a periodic wave and the total motion depends on travelling waves along the diatomic chain that fulfill the boundary condition. Our purpose will be to find the frequencies correspond to these waves. The motion of the N-th atom with mass M is a linear superposition of travelling waves in the chain, the mathematical representation reads

$$U_N(t) = \sum_q \tilde{U}_q \exp[i(qna - \omega_q t)], \tag{2.21}$$

where q is the wave vector, ω_q is the frequency corresponding to the wave vector, and $\tilde{U}_q$ is the amplitude of the wave vector. Similarly, the equation of motion for the N-th atom with mass m is

$$u_N(t) = \sum_q \tilde{u}_q \exp[i(qna - \omega_q t)], \tag{2.22}$$

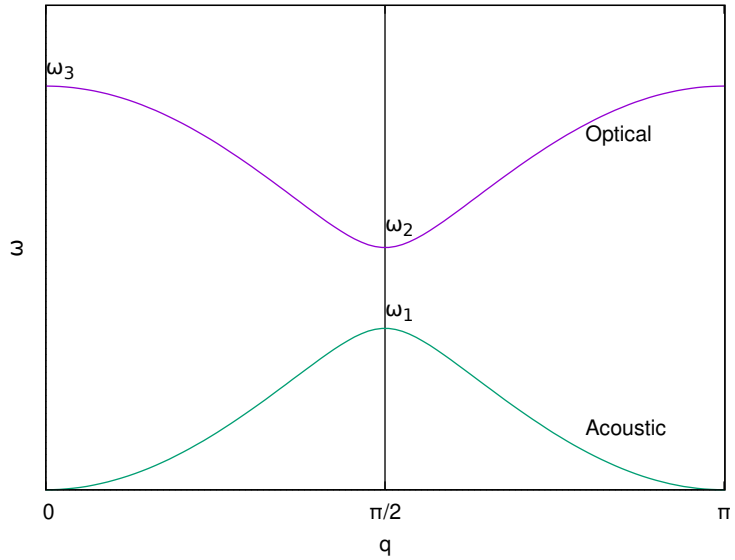

Figure 2.8: Dispersion curve for the one-dimensional diatomic chain, where we assume $k = K$. The maximum happens in the edge of Brillouin zone. $\omega_1 = (2K/M)^{1/2}, \omega_2 = (2K/m)^{1/2}$ and $\omega_3 = (2K(\frac{1}{M} + \frac{1}{m}))^{1/2}$

where $\tilde{u_q}$ is the amplitude corresponding to the wave vector q. Substituting equations (2.21) and (2.22) into equations (2.19) and (2.20), we obtain the dispersion relation as below:

$$\omega_q^2 = \frac{(M+m)(K+k)}{2Mm} \pm \frac{\left((M+m)^2(K+k)^2 - 16MmKksin^2(ka/2)\right)^{1/2}}{2Mm}. \tag{2.23}$$

Therefore, for the diatomic chain there are two solutions, which in dispersion diagram are called "branches". As shown in Fig.2.8, the first branch corresponds to a wave for which the two atoms move in the same phase and the second one is when the two atoms move in opposite phase. When the atoms are moving in the same phase, the branch is called "acoustic branch" and when two neighbour atoms are moving in opposite phase, the branch is called "optical branch" [85].

Chapter 3

Thermoelectricity in molecular systems

"Turning temperature differences directly into electricity could be an efficient way of harnessing heat that is wasted in cars and power plants."

— David L. Chandler

Thermoelectricity is the direct conversion of heat into electricity and vice versa. Applying a temperature difference through a material can produce electricity and having an electric current along the material creates a temperature difference. Using efficient thermoelectric materials, it is possible to generate electricity, measure temperature, and heating/cooling the electronic devices [90].

At the atomic scale, when a temperature gradient is applied, the charge carriers in the material will diffuse from the hot end to the cold end [91]. The concept of using single molecules in the composition of electronic components, also known as molecular electronics, to reach the increasing demand for minimization of electronic circuits, looks promising [92, 93, 94, 95]. Transport characteristics of molecular junctions have been exhaustively investigated to explore the possibility of building molecular devices with desirable thermoelectric efficiency [8, 96, 97, 94, 98, 99, 100, 101, 4, 7]. Yet, in both theory and experiment, it is still challenging to study the thermoelectric properties of molecular junctions [102, 11, 103]. Fundamentally, exploring thermal transport in molecular junctions

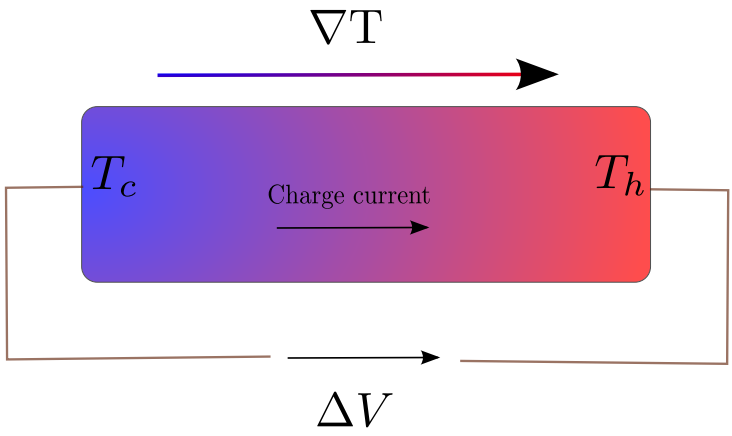

Figure 3.1: Illustration of a system under a temperature gradient

is useful to spot the limits to classical transport theories at the nanoscale. Additionally, for developing high efficient energy conversion devices, studying thermal transport of molecular junctions is essential [9, 104, 105]. Nonetheless, in the last decade, with all the technical and computational advance, the thermoelectric properties of molecular junctions had been widely explored both experimentally and theoretically [8]. Besides, converting the extra heat produced in the electronic device to electricity will increase the total efficiency. Therefore, it is interesting to engineer the thermoelectric properties of conductive materials[106, 107, 6]. In this chapter, we discuss the basic definitions of thermoelectricity.

3.1 Seebeck and Peltier effect

In 1821, T. J. Seebeck discovered the effect governing thermoelectric power generations in solids. Afterwards, this effect was investigated in more details by J. Peltier. When two leads are in electric contact, there will be an electron flow from the lead that has a higher occupation level to the one with a lower occupation level. The occupation level depends on the Fermi energy of the metal. The Fermi energy is between the energy levels occupied by electrons and the ones that are unoccupied. The electron flow between the two leads occurs until the Fermi energies of both leads coincide.

Assume a solid under a temperature gradient where the temperature of the hot end is T_h and the temperature of the cold end is $T_c < T_h$ (see Fig.3.1). To set the temperature difference, heat must enter the hot lead and leave through the cold lead. The electrons in the hot end are in a higher energy level as compared with the cold end. Therefore, a charge current density $\vec{j}$ is produced. This current creates a voltage difference ΔV in the solid. The electromotive force is linearly proportional to the temperature difference. The so called Seebeck coefficient S is the ratio of the voltage over the temperature difference [91]:

$$S = -\frac{\Delta V}{T_h - T_c}. \tag{3.1}$$

The sign of the Seebeck coefficient depends on the nature of charge transport. If most of the charge carriers are electrons the Seebeck coefficient is negative, conversely, if most of the charge carriers are holes it will be positive. The charge current corresponding to the voltage is

$$I = \frac{2e}{h}\int_{-\infty}^{\infty} \tau(E)(f_L - f_R)dE, \tag{3.2}$$

where $\tau(E)$ is the electronic transmission, and $f_{\{L,R\}}$ is the Fermi-Dirac distribution function for the electrons in the left L and right R lead [108].

When the transport is coherent meaning there is no inelastic scattering, we could express the Seebeck coefficient in terms of transmission function $\tau(E)$. Having defined K_n as below

$$K_n(\mu) = \frac{2}{h}\int_{-\infty}^{\infty} dE\tau(E)(E-\mu)^n\left(-\frac{\partial f(E,\mu)}{\partial E}\right), \tag{3.3}$$

where μ is the chemical potential, the Seebeck coefficient reads [109]

$$S = \frac{K_1(\mu)}{eTK_0(\mu)}. \tag{3.4}$$

It should be noted that similar to electrons, phonons also cause some gradient temperature contributing to thermal conductance, and could interact with the charge carriers. Therefore, there is a phonon contribution to the Seebeck coefficient.

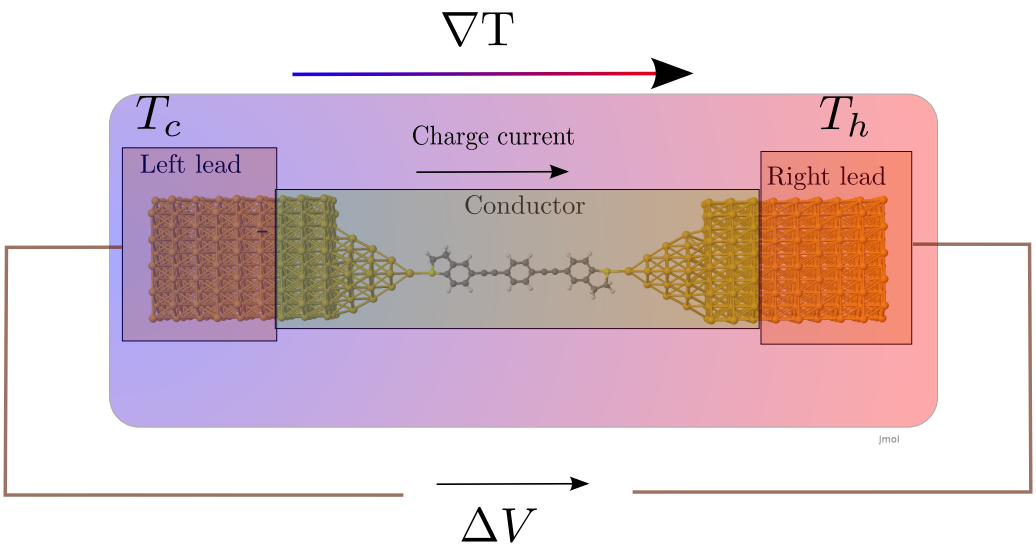

Figure 3.2: An electric circuit containing a molecular junction under a temperature gradient

Yet, by cause of extensive phonon-phonon interactions, we can neglect phonon contribution at high temperature [110].

Peltier also discovered that if an electric current flows from one lead to another, then heat dissipates throughout the junction (Fig.3.2). The Peltier heat can be evolved and heat up the junction or absorbed and cool down the junction. Net cooling is accomplished when Peltier cooling is larger than Joule heating [3]. The power associated with the total heat dissipated in the left lead P_L within the Landauer-Büttiker formalism, considering the coherent electronic transport, is calculated as [3]

$$P_L(T_L, T_R, V) = \frac{2}{h}\int_{-\infty}^{\infty}(\mu_L - E)\tau(E,V)(f_L - f_R)dE, \tag{3.5}$$

where μ_L is the chemical potential of the left lead, $\tau(E,V)$ is the bias dependent electronic transmission and V stands for an applied bias [91]. Note that the total heat dissipation includes both Joule heating and Peltier effect, consequently, net refrigeration happens when P_L <0. We should mention, despite of all the theoretical studies, due to technical difficulties in measuring pW level cooling [11], there were not so many experimental results until recently [3].

3.2 Thermoelectric efficiency and figure of merit

All the materials show thermoelectric effect, but not all of them are efficient to be used in electro-thermal devices. During the last decades, there has been an intensive effort to search for efficient thermoelectric materials. The basic challenge in the quest of efficient thermoelectric materials is that they need to have a high electric conductance and low thermal conductance, so one side of the material gets hot while the other side is cold [91]. Hence, to achieve high efficiency, one needs a careful tuning of the material electrical and thermal properties [2].

The efficiency of a thermoelectric molecular junction η is the ratio of energy supplied to the load per heat energy adsorbed at the junction [110]. The efficiency depends on the system electrical conductivity, Seebeck coefficient and its thermal conductivity, which are all temperature dependent. The maximum efficiency of the energy conversion process is described by the figure of merit ZT of the thermoelectric material as [104, 110]

$$\eta_{max} = \frac{T_H - T_C}{T_H} \frac{\sqrt{1+ZT}-1}{\sqrt{1+ZT}+\frac{T_C}{T_H}}, \tag{3.6}$$

which converges to the efficiency of a Carnot engine when $ZT \to \infty$,and ZT is given as

$$ZT = \frac{GS^2T}{\kappa_{el}+\kappa_{ph}}, \tag{3.7}$$

where G is the electrical conductivity, S is the Seebeck coefficient and $\kappa_{el}(\kappa_{ph})$ is the thermal conductivity of the electrons (phonons). The numerator GS^2 is called the power factor and appears often in the literature. It is directly related to the output power that is generated in a thermoelectric device. It should be noted, if the geometry is fixed and there is unlimited heat source, a material with higher power factor will generate more energy. However, as for different applications the thermoelectric device is optimized, they will operate at the maximum efficiency which is characterized by ZT and not power factor [111].

Since the electronic thermal conductivity depends on charge carries, it is related to electrical conductivity. Once again if the transport is coherent, we could express the electronic contribution to the thermal transport in terms of the transmission function $\tau(E)$. Having K_n from equation 3.3 the thermal conductivity of the electrons can be written as [109]

$$\kappa_{el} = \frac{K_2(\mu) - [K_1(\mu)]^2/K_0(\mu)}{T}. \tag{3.8}$$

By contrast, the thermal conductivity of phonons depends on the lattice dynamics and is independent of charge carriers [110]. The phonon contribution to the thermal conductivity does not have a simple expression and depends on phonon-phonon processes. However, we measure the phonon thermal conductivity using Eq.2.14.

Generally, a thermoelectric material displaying a relatively large value of ZT should have a high electric conductivity, a high Seebeck coefficient and a low thermal conductivity. Molecular junctions may have interesting thermoelectric transport properties if their thermal conductance is minimized. Part of this work consists in finding routs to reduce thermal transport across molecular junctions.

Chapter 4

Electronic conductance and thermopower of single molecular junctions

"Everything is energy and that's all there is to it. "

— Albert Einstein

***Preamble**: A large part of some sections in this chapter are literal excerpts of the article "Electronic conductance and thermopower of single-molecule junctions of oligo(phenyleneethynylene) derivatives" [2] written by Hervé Dekkiche, Andrea Gemma, Fatemeh Tabatabaei, Andrei S. Batsanov, Thomas Niehaus, Bernd Gotsmann and Martin R. Bryce. This article has been written collaboratively with the experimental partners in EFINED project from Durham university, Durham, UK and IBM, Zurich, Switzerland. To this article, I contributed by running the simulations. At the beginning of every section I will mention whether the content of the section is taken from this paper, or not. As for the short introduction, it is taken from the article.*

Governing the electrical, thermal and thermo-electric transport in molecular junctions has a crucial role in the design and operation of energy conversion devices used for new energy-saving technologies. It is highly desirable to achieve a large

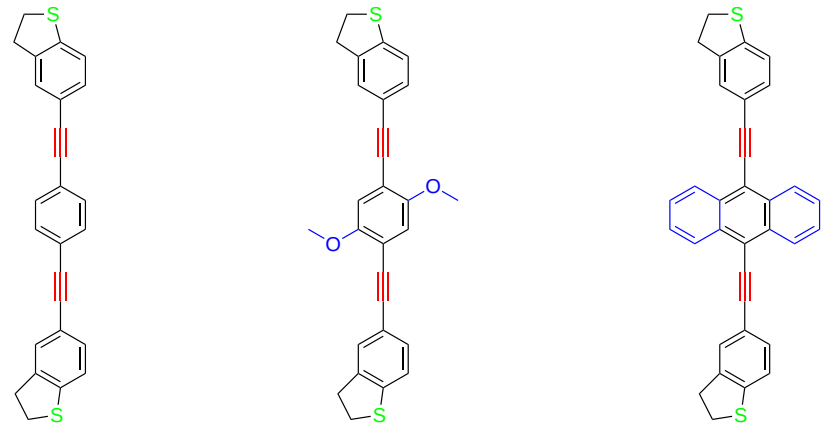

Figure 4.1: The structure of new OPE3 derivatives studied in this chapter

thermopower for thermoelectic materials [2, 6, 7, 4, 9]. The use of solid material for efficient thermoelectric materials had been studied and the results were promising. However, their price and their complex manufacture makes them inefficient for wide usage [112]. Recently, the usage of organic materials in thermoelectric devices has attracted a great attention as they are flexible, low cost, and climate-friendly [113, 114]. Also high thermoelectric efficiency has been predicted for some of them. Additionally, organic molecules show a conductive delocalised π electronic system [115]. Overall, organic molecules can be used for thermoelectric devices.

In this chapter we compute the single-molecule conductance and thermoelectric properties of new OPE3 derivatives where three is the number of phenylene rings in the backbone. The structure of these molecules is shown in Fig.4.1. As mentioned in [2], we chose OPE3 derivatives as they are synthetically-versatile, highly-conjugated, robust molecules and they have been widely studied in molecular electronics. OPE3 systems, in particular, can be conveniently assembled and measured in metal–molecule–metal junctions. The wide agreement between conductance data obtained for OPE3 junctions in different research groups, makes this an excellent candidate for a systematic study on the influence of side groups. We chose the dihydrobenzo[b]thiophene (DHBT) anchor as this group is known to bind efficiently

to metal electrodes, with high junction formation probability [116], and without the problems associated with thiol anchors, such as oxidation and formation of metal-thiolate clusters [117]. Using DFT and DFTB, the calculations were performed to support the experimental results obtained by our partners in EFINED project [2]. We demonstrate that these molecules show the structural features that are required for thermal conductance studies.

4.1 OPE3-Ph vibrational density of states in DFT and DFTB

Preamble: *This section corresponds to my work during the project.*

As a first step, the compatibility of DFT and DFTB has been investigated. For this reason, we performed a normal mode analysis of OPE3-Ph in the gas phase to identify characteristic vibrations that could be relevant for the thermal conductance of the molecular junctions. We focus on modes of the terminal anchor groups as well as some important vibrations of the molecular backbone. Calculations were performed with DFTB using DFTB+ package and with DFT using the PBE exchange-correlation functional and a $6-31G^*$ basis set as implemented in the NwChem code. Table 4.1 summarizes the main results.

The largest frequencies involving the backbone occur when the two triple carbon bonds oscillate asymmetrically and symmetrically along the backbone direction (By asymmetric oscillations we mean that while the triple bond on the left is shrinking the one on the right is expanding and vice versa. Both of the triple bonds expand and shrink at the same time for the symmetric motion.) The anchor groups feature some low lying vibrations from approximately 300 to 500 cm^{-1} which are at significant larger frequency than the phonon modes of gold [118], that extend up to 200 cm^{-1}. This would indicate low phonon transmission across the junction. Interesting in this respect is the mode at 136 cm^{-1} in DFTB and 123 cm^{-1} in DFT lying in the gold phonon bands. It corresponds to a rocking motion of the central

Description of vibrational mode	$\omega_{DFTB}(cm^{-1})$	$\omega_{DFT}(cm^{-1})$
central ring rocking	136	123
anchor group (asym.rocking)	318	301
anchor group (sym.rocking)	330	319
SC_2 (asym.scissoring)	473	463
SC_2 (sym.scissoring)	481	464
middle benzene (rocking)	659	614
middle benzene (asym. stretching)	1565	1426
triple bonds (sym. stretching)	2388	2223
triple bonds (asym. stretching)	2397	2237

Table 4.1: Comparison of vibrational modes as given by DFT and DFTB

ring which is accompanied by large changes in the total molecular length. We predict that phonon transmission occurs mainly via this channel. Comparing the results of DFTB and DFT, we find that the predictions are rather close with DFTB providing in general larger frequencies. In general, both DFT and DFT/PBE are expected to yield frequencies with an average accuracy of roughly 50 cm^{-1} with respect to experiment [119].

4.2 Optimization and binding energy of OPE3-Ph on Au(111)

Preamble: *The content of this section is a literal copy of our collaborative paper [2]. However, the straight binding configurations in DFT and DFTB are not mentioned in the paper.*

In this section binding energies of OPE3-Ph on Au(111) were computed. We employed DFT as implemented in Quantum ESPRESSO [120] and DFTB as developed in DFTB+ package. For DFT, we used the PBE exchange–correlation functional [21], and PAW pseudo-potentials [121]. Energy cutoffs of 70 Ry and 280 Ry were used for the plane wave expansion of wave functions and electron density, respectively. As for the gold surface, a 4-layer slab model of the (5×6) surface supercell of Au(111) was relaxed at the Γ point. For the surface calculations, all the layers

were allowed to move. The same settings were applied to model the adsorption of OPE3-Ph on the surface except that during adsorption simulations only the top two layers were allowed to move. As for DFTB calculations, we used the auorg-1-1 Slater-Koster set [39, 122, 123] with orbital dependent Hubbard parameters. A periodic setup was used as well and the optimization was done at the Γ point.

Binding energies E_{ads} were computed as

$$E_{ads} = E_{cmp} - E_{Au(111)} - E_{mol}, \tag{4.1}$$

where E_{cmp} is the total energy of the OPE3-Ph-Au(111) complex, E_{mol} is the total energy of OPE3-Ph relaxed in the gas phase, and $E_{Au(111)}$ is the total energy of the relaxed surface. The size of the unit cell was chosen such that the distance between the complex and its periodic image is at least 9 Å, to avoid interaction between the surface and its periodic image.

4.2.1 Straight binding configurations in DFT

The binding configuration between gold and the molecule is not known in the experimental measurements. We thereby computed the binding energy of OPE3-Ph to ideal $Au(111)$. This will give us a first impression of the relevant binding motifs that should also be of relevance for the rough surfaces in break junctions. DFT geometry optimizations were performed for OPE3-Ph on the Au(111) surface using periodic plane wave calculations. First, we investigated structures where the molecular backbone is orthogonal to the surface. The sulfur atom of the DHBT anchoring group was positioned at the top, bridge, fcc and hcp positions of the surface as shown in Fig.4.2.

The most stable binding configuration is the top position with an Au–S bond length of 2.77 Å, as shown in Fig.4.2. The bridge structure shows a low adsorption energy and a very long Au-S distance of 2.91 Å. Optimization of the fcc configuration leads to a structure where the sulfur is nearly at a top position.

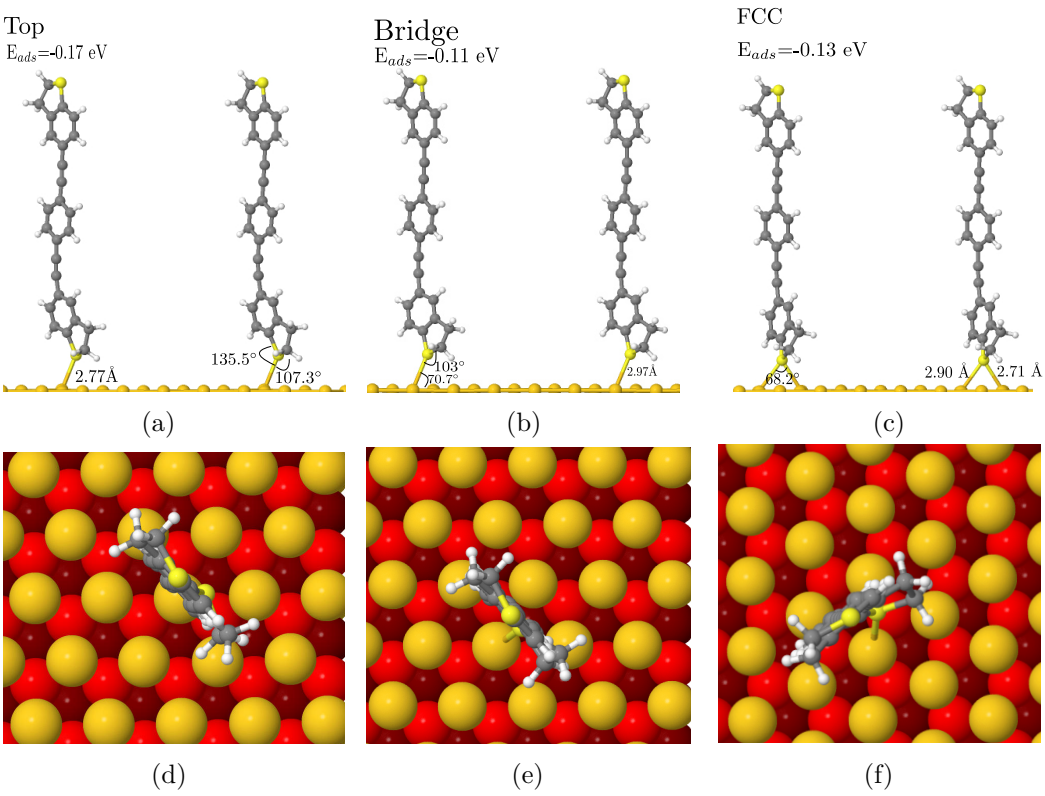

Figure 4.2: Optimal binding configurations of OPE3-Ph on Au(111) from periodic DFT simulations. Side views and bond parameters for a) top b) bridge and c) fcc. Top view for d) top e) bridge f) fcc (darker colour of Au atoms indicates larger distance to the surface).

4.2.2 Straight binding configurations in DFTB

For the same binding configuration as Sec. 4.2.1, the optimization was done at the Γ point using DFTB. The binding energies and Au-S bond lengths for different binding configuration calculated using DFT and DFTB are listed in Table. 4.2. The optimal structure when Sulfur is on the top position has been shown in Fig.4.3. The Au-S bond length is pretty large (4.32Å) compared with DFT calculations. For the binding energies, there is a large difference (at least 4.9 eV) between the result of DFT and DFTB.Moreover, the periodic gold surface should remain in its crystal structure (FCC symmetry) after geometry optimization but the atoms can move slightly. Fig.4.3a shows that this is not the case when the geometry of OPE3-Ph on gold surface is optimized in DFTB. Not only the gold atoms do not

Structure	Binding energy (eV)			Au-S (Å)		
	DFT PBE	DFTB	DFTB fixed	DFT PBE	DFTB	DFTB fixed
bridge	-.11	-5.29	-.18	2.97	4.79	3.90
fcc	-.13	-6.31	-.19	2.71	4.21	3.82
top	-.17	-5.03	-.18	2.77	4.32	3.79

Table 4.2: Binding energies and Au-S bond lenght for different positioning of OPE3-Ph on gold surface in DFT-PBE, DFTB, and DFTB-fixed where the gold atoms are fixed using DFT-PBE

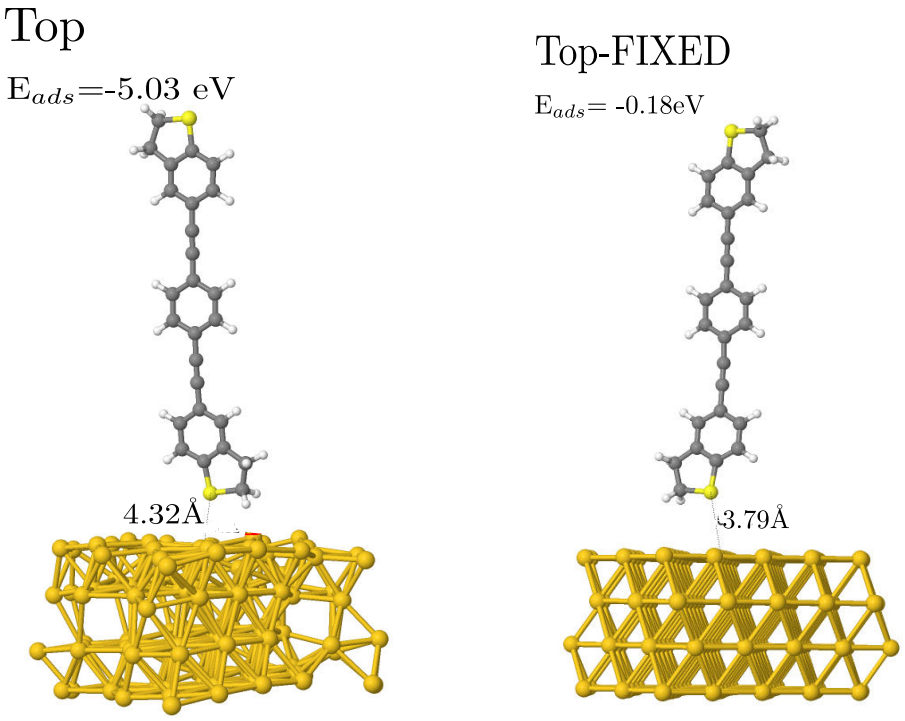

(a) (b)

Figure 4.3: Optimal binding configurations of OPE3-Ph on Au(111) from periodic DFTB simulations and the bonding parameters when a) all the atoms are free to move b) the gold atoms are fixed.

take a favorable shape but also the Au-S bond length has a large difference with the one of DFT calculations. Hence, Slater-Koster parameterization in DFTB does not work probably in the optimization of periodic gold surfaces.

Consequently, it was decided to do an optimization of OPE3-Ph on Au(111), where the gold surface was fixed at its equilibrium position and only the atoms of the molecule were allowed to move. For the top postition, the Au-S bond length is

3.79Å, which is larger than the one obtained from DFT. The binding energy is -0.18 eV, which is in a good agreement with DFT results.

It should be noted that in this part of the project as the DFTB optimization does not work properly for the periodic gold surface, we needed to make a decision for a new strategy to model the molecular junction. We have shown for OPE3-Ph on Au(111) that if the gold atoms are fixed at their equilibrium position, we have a good agreement for the resulting binding energies obtained by DFTB and DFT. However, to build the molecular junction, a geometry optimisation is needed. To this end, we use DFT to build the molecular junctions. Later on, this junction was used for NEGF-DFTB calculations, since for a given structure the transport calculations are faster in DFTB.

4.2.3 Tilted binding configurations in DFT

Afterwards, we explored also other possible binding configurations. The supercell was built the same way as Sec.4.2.1 except that the molecule was placed on the top of Au(111) in a tilted configuration. We considered three different positioning of Sulfur on Au(111), top, bridge, and fcc. A top view of the optimal configuration, binding energies and bonding angles are shown in Fig.4.4.

The most stable binding configuration is the top position with an Au–S bond length of 2.55 Å, as shown in Fig.4.4. The bonding angles indicate a pyramidalisation of sulfur, consistent with a coordinate bond where one of the S lone pairs interacts with Au d-orbitals. The binding energy of OPE3-Ph for the most stable conformer shows that the DHBT group provides an effective anchor. Moreno-García and co-workers investigated the binding energy of several aurophilic functional groups. Specifically, they looked at cyano (CN),amino (NH_2), thiol (SH), 4-pyridyl (PY) and the present DHBT and found the energetical ordering $NH_2 <$ DHBT $\approx$ CN $\approx$ PY $<$ SH, where NH_2 denotes the least stable anchor group. Although the OPE3 molecular wire was coupled to an Au pyramid in the Moreno-García study,

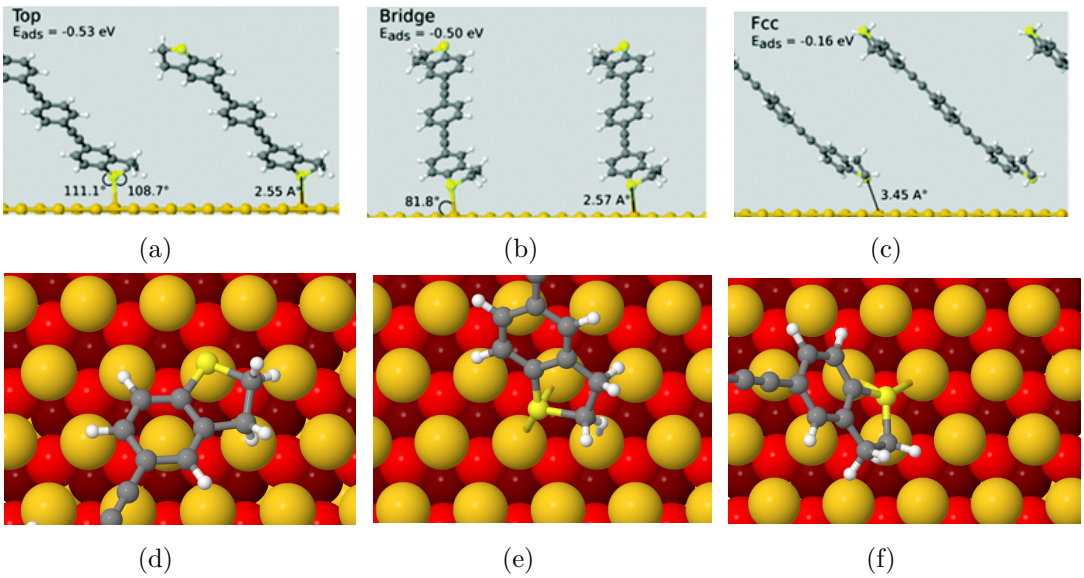

Figure 4.4: Optimal binding configurations of OPE3-Ph on Au(111) from periodic DFT simulations. Side views and bond parameters for a) top b) bridge and c) fcc. Top view for d) top e) bridge f) fcc (darker colour of Au atoms indicates larger distance to the surface). a,b,c copied from [2]. d,e,f reproduced from [2]

the reported binding energy of E_{ads} = -0.41 eV is close to our result for the top position [116]. The fcc structure shows a low adsorption energy and a very long Au-S distance of 3.45 Å. Optimization of the bridge configuration leads to a structure where the DHBT sulfur is nearly at a top position. In contrast to the more common thiol anchor groups, DHBT features a sulfur lone pair with fixed orientation with respect to the molecular plane, and this reduces the available conformational space.

Table. 4.3 shows the binding energies and Au-S bond length for various positioning of OPE3-Ph on gold surface in straight and tilted binding configuration. In both straight and tilted binding configurations, the top positioning of sulfur atom on gold surface has the least binding energy. However, the tilted binding configurations show more stable structure. Moreover, Au-S bond length for tilted configurations are in conformity with experimental value [124]. Thereby, latter we use tilted configuration to obtain the electronic transport properties of OPE3 derivatives.

Structure	Binding energy (eV)		Au-S (Å)	
	straight	tilted	straight	tilted
bridge	-.11	-0.50	2.97	2.57
fcc	-.13	-0.16	2.71	3.45
top	-.17	-0.53	2.77	2.55

Table 4.3: Binding energy and Au-S bond length for different positioning of OPE3-Ph on gold surface in straight and tilted binding configuration

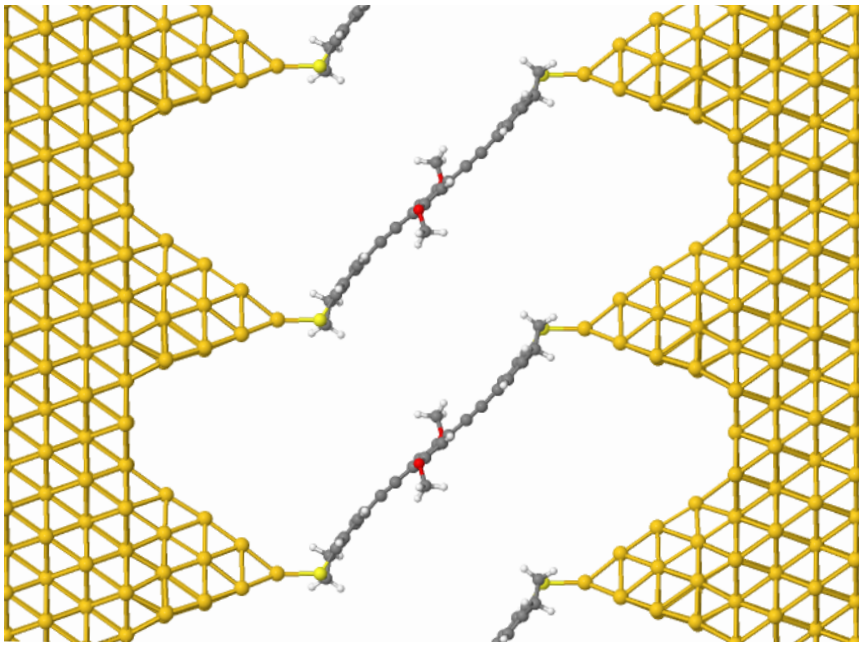

Figure 4.5: Device geometry for DFTB transport simulations. Shown here is OPE3-Ph$(OMe)_2$ connected to semi-infinite gold leads. Reproduced from [2]

4.3 NEGF-DFTB for junctions of OPE3 derivatives

Preamble: *The content of this section is a literal copy of our collaborative paper [2]. However, the convergence test for the transmission and the conductance is not mentioned in the paper.*

NEGF-DFTB was employed to compute the thermoelectric properties of OPE3 derivatives. We used the auorg-1-1 Slater-Koster set [39, 122, 123] with orbital dependent Hubbard parameters. A periodic setup was used, where the device is repeated perpendicular to the transport direction along the surface. This necessitates a solution of the Poisson equation in periodic boundary conditions to compute

the charge density in the device region. The device in Fig.4.5, was prepared in multiple steps. At first, we optimized the geometry of the OPE3 derivatives between two Au_{20} clusters in the gas phase using NWCHEM code [125]. The calculation was performed using a 6-31G* basis set for C, H, S and lanl2dz_ecp basis set for Au. For the exchange-correlation functional, PBE-GGA was used. Using Atomic Simulation Environment (ASE) [126], the Au_{20}-molecule-Au_{20} was fixed between two Au(111) surfaces accommodating three layers with 30 atoms per layer. Then, we coupled this device to gold leads accommodating three layers that were repeated in the transport direction. Not to mention, during all of this process the Au-S-C angle, that we found in the gas phase geometry optimization, was preserved. Consequently, tilting of the molecule to the surface was accurate.

4.3.1 Convergence test for the transmission and the conductance

To compute the transmission using DFTB-NEGF, the Poisson equation was solved in the device region using a Green's function solver. The parameters for the Green's function solver need to be converged. We solve Poisson equation to obtain the transport properties. First convergence test was done for the accuracy for the approximate solution of the Poisson equation. The minimal grid to sample the transport device in the real space and the energy step along the real axis integration for NEGF calculations were converged. For the complex contour integration of the Green's function, the number of Poles enclosed in the contour and the number of points along the contour should be converged. After convergence test, the default values in DFTB+ for Green's function solver were used. Moreover, the transmission function should be converged with respect to the k-point sampling of the leads. As shown in Fig.4.6a, the energy dependent transmission was computed for different k-point sampling from $2 \times 2 \times 2$ to $11 \times 11 \times 11$. As the mesh in k-point sampling increases the dip around the Fermi energy starts to fade. Using the transmission function, we calculated the conductance from Eq.1.37. The results is shown in Fig.4.6b.

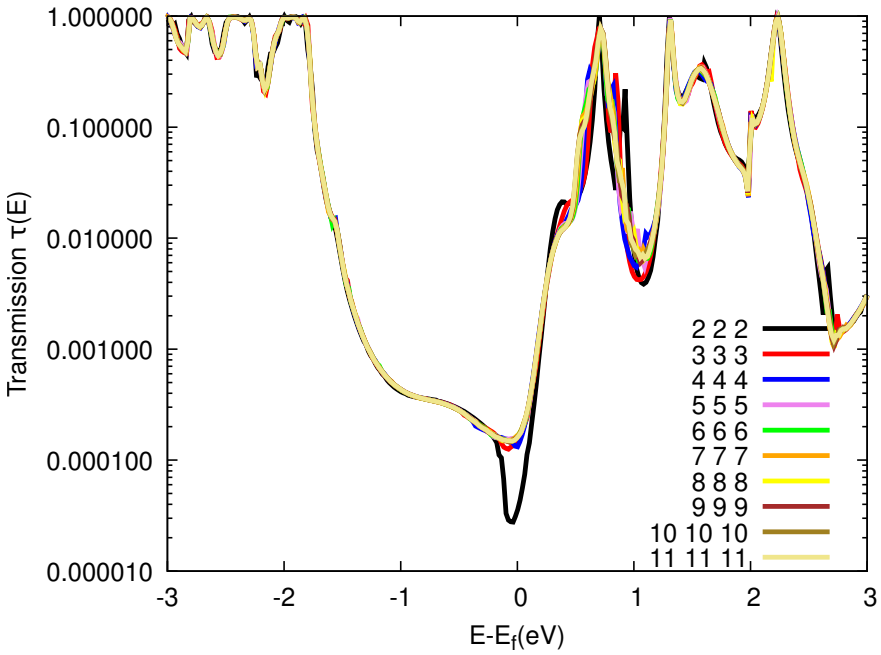

(a)

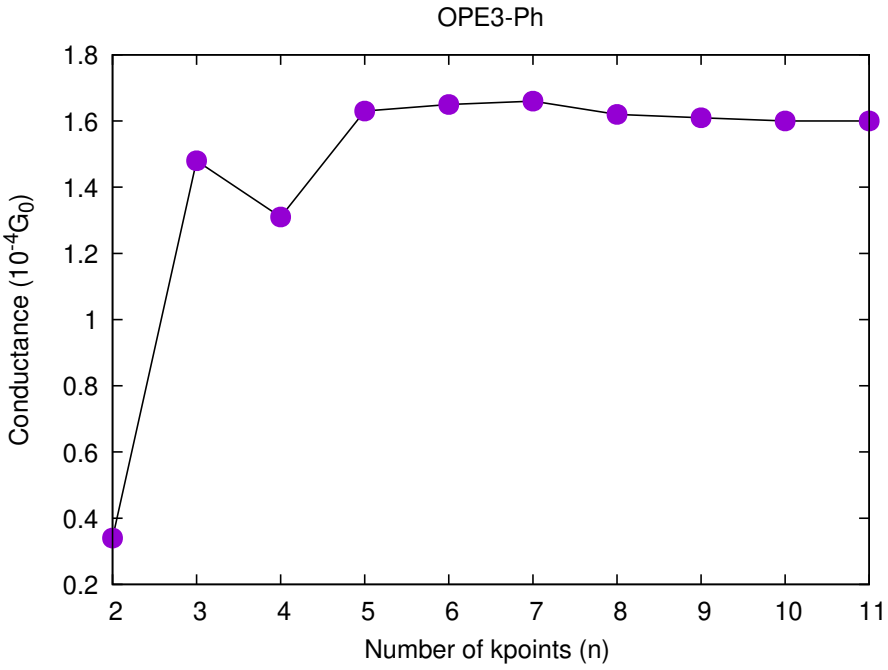

(b)

Figure 4.6: a) Transmission function for different k-point sampling for OPE3-Ph and b) Conductance of OPE3-Ph versus number of k-points. The x-axis shows n for an n × n × n k-point set.

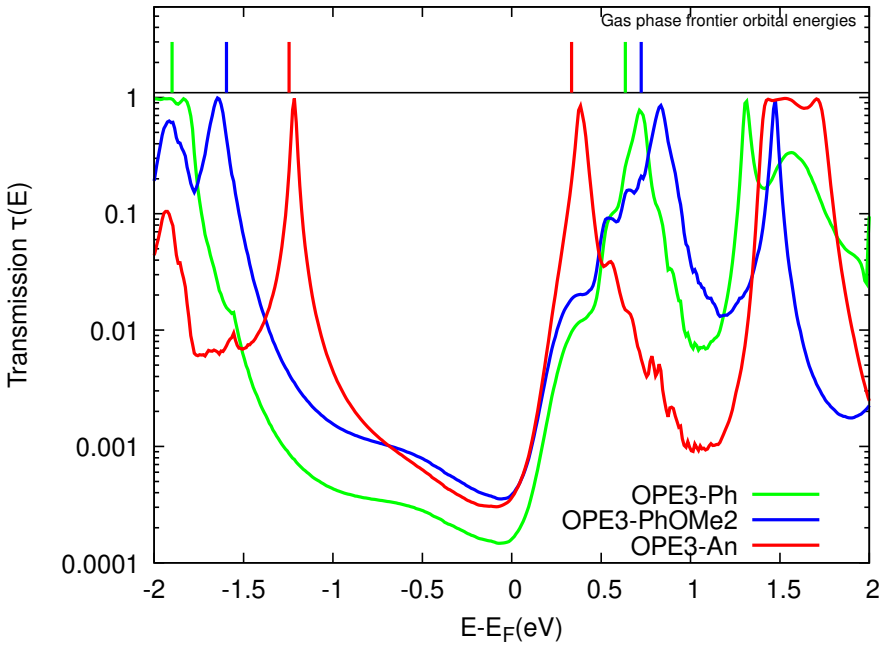

Figure 4.7: DFTB transmission function $\tau(E)$ for three OPE3 derivatives. For illustration the HOMO and LUMO energies of the isolated molecules in the gas phase are at the top of the plot. The gas phase energy levels are shifted by a Δ to be aligned with Fermi energy of the substrate, where Δ is the difference between the middle of HOMO-LUMO gap for the device and the molecule. We calculated ΔOPE3-Ph$= -1.45eV$,ΔOPE3-PhOMe$_2 = -1.44eV$, and ΔOPE3-An$= -1.0eV$.

To calculate the conductance, the behaviour of the transmission around the Fermi energy has a crucial role. Hence, the value of conductance fluctuates for insufficiently large k-point sampling. Finally, the value of conductance converges to $1.60 \times 10^{-4} G_0$ with an accuracy of $10^{-6} G_0$. In the following calculations, a 10×10×10 k-point sampling has been used in the construction of the lead self-energy.

4.3.2 Results for OPE3 derivatives

In this section, we discuss about the transport properties of the OPE3 derivatives using NEGF-DFTB. We computed the energy dependent transmission function $\tau(E)$, which is related to electronic conductance as shown in Eq.1.37. The result is shown in Fig.4.7. The side groups at the central OPE3 ring have a crucial

role on the HOMO position. The HOMO shift of approximately 0.15 eV in OPE3-Ph$(OME)_2$ with respect to the HOMO level in OPE3-Ph is due to electron-donating OMe group. The extension of the π system in OPE3-An has an even stronger effect with a shift of 0.75 eV with respect to OPE3-Ph. The LUMO energy levels do not show a big change in different derivatives. The electrical conduction occurs through the orbital that is closest to the Fermi energy, thereby, the differences in conductance for OPE3 derivatives is not large, as verified by our calculation and experiment (see Table.4.4). While OPE3-An shows a perfect LUMO transmission, both OPE3-Ph and OPE3-Ph$(OMe)_2$ show low values for transmission. This is most likely due to partial destructive interference of transmission paths through energetically close lying molecular orbitals.

4.3.3 Exploratory configurations for OPE3-Ph

To examine the effect of different binding configurations on transmission, we performed NEGF-DFTB calculations for possible configuration of a OPE3-Ph junction. We refer to the junction from the previous section, with Au_{20}-molecule-Au_{20}, as Au_{20}-tilted (see Fig.4.5). Additionally, we investigated four more possible junction configurations as shown in Fig.4.8. First, we considered the most stable structure from the binding energy calculation in section 4.2. So, the OPE3-Ph binds directly to the flat gold surface. It should be noted, considering limited computational resources, the second electrode is symmetrically placed with respect to the first electrode and no geometry optimization was done (flat surface- tilted, Fig.4.8d). As discussed in Sec.4.2.1, another possible geometry with a higher energy was predicted where OPE3-Ph was placed perpendicular to the Au(111). This junction is labelled flat surface-straight and shown in Fig.4.8b. Likewise, we considered binding through one Au atom where the OPE3-Ph is perpendicular to the gold surface (adatom – straight, Fig.4.8a) and OPE3-Ph tilted between the gold surfaces (adatom – tilted, Fig.4.8c). The fcc and hcp positioning of the Au atom were studied. The computational parameters for all of these possible junctions are

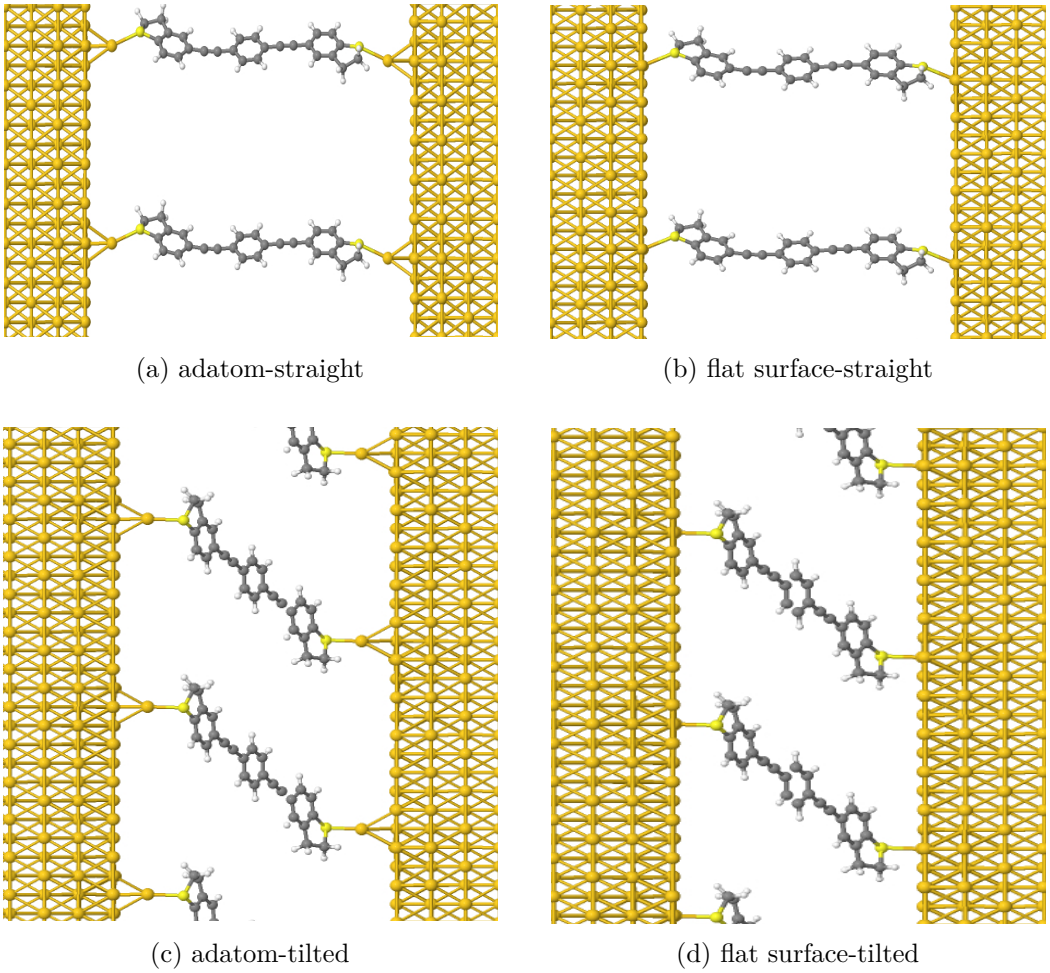

(a) adatom-straight (b) flat surface-straight

(c) adatom-tilted (d) flat surface-tilted

Figure 4.8: Possible OPE3-Ph junction configurations.

the same as for Au_{20}-tilted.

The transmission results are shown in Fig. 4.9. As a result of the manual construction of the junction without geometry optimization, the transmission for the junctions in Fig.4.8 is noisy around the Fermi energy. Nonetheless, for the straight junctions the HOMO/LUMO levels are shifted to higher energies with respect to Au_{20}-tilted and show transmission through the HOMO level, therefore, Seebeck coefficients become positive. On the other hand, the adatom junctions shift the HOMO/LUMO levels to lower energies with respect to flat surface junctions.

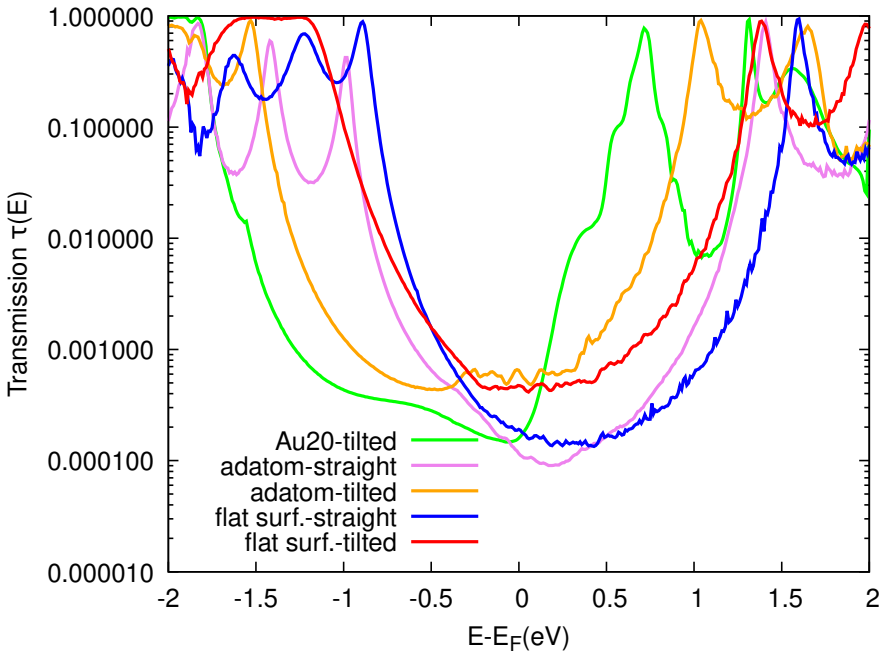

Figure 4.9: DFTB transmission for OPE3-Ph junction models in Fig.4.8 and the Au_{20}-tilted structure in Fig.4.5

4.4 Seebeck coefficients for OPE3 derivatives

Preamble: *The content of this section is a literal copy of our collaborative paper [2].*

As discussed in section 3.1, the electronic transmission can be used to estimate Seebeck coefficients from equation 3.4. At low temperatures, applying the Sommerfeld expansion the Seebeck coefficient reads [93]

$$S = -\frac{\pi^2 k_B^2 T}{3e} \frac{\tau'(E_F)}{\tau(E_F)}, \tag{4.2}$$

where E_F is the Fermi energy, and the $\tau'(E_F)$ denotes to the derivative of the transmission function with respect to the energy, estimated at the Fermi energy.

The theoretical and experimental values for Seebeck coefficient and electric conductance are reported in Table 4.4. The negative Seebeck coefficient which is an indication of transport through LUMO is in agreement with the experimental values. Not to mention, for the additional exploratory calculations shown in section

	G_{exp} $[10^{-4}G_0]$	G_{theo} $[10^{-4}G_0]$	S_{exp} $(\mu V/K)$	S_{theo} $(\mu V/K)$
OPE3-Ph	0.92	1.60	-11.4±0.5	-25.6
OPE3-Ph$(OMe)_2$	2.03	3.86	-7.9±1.3	-27.0
OPE3-An	1.82	3.64	-8.7± 1.6	-37.1

Table 4.4: Conductance and Seebeck coefficient for OPE3-Ph, OPE3-PhOMe$_2$ and OPE3-An at 295 K. Experiments are described at [2].

4.3, the straight conformers feature HOMO/LUMO resonances that are considerably shifted to higher energies with respect to Au_{20}-tilted and therefore lead to positive Seebeck coefficients. The adatoms have an opposite effect, such that the adatom–tilted conformer comes closest to the fully relaxed Au_{20}-tilted conformer. Thence, the Fermi level positioning is influenced by sulfur pyramidalisation and the bonding to undercoordinated Au atoms, both factors favouring a negative Seebeck coefficient (Fig.4.9).

In experiment, OPE3-Ph has the lowest conductance and the largest Seebeck coefficient. Since the transmission derivative is usually dominating over the transmission in the equation 4.2, this is consistent with a LUMO position of OPE3-Ph that is slightly closer to Fermi energy than for OPE3-Ph$(OMe)_2$ or OPE3-An. The DFT simulations do not reproduce the trend for Seebeck coefficients in the OPE3 derivatives. To some degree, these errors might be related to the known difficulties of DFT and DFTB to predict the transport gap and the positioning of the Fermi level [127]. All in all, our theoretical simulations confirm the experimental transport mechanism with a small variability in the thermopower.

Chapter 5

Thermoelectricity of cross-linked molecular junctions

"Have no fear of perfection, you'll never reach it."

— Marie Curie

As discussed in chapter.3, molecular junctions can be used to remove heat from nanoelectronic devices and convert the wasted heat to electricity [106]. However, until recently due to technical difficulties, tuning the thermoelectric properties of nano-junctions was not possible [128]. Notably, the recent innovative investigations in which a large thermoelectric efficiency was achieved by tuning the thermoelectric properties of a single-molecule junction, are reassuring [128, 129]. These studies open up new prospects of molecular electronics applications as well as probing the fundamental physics of thermoelectric conversion in nanoscale molecular junctions. Using MD along with convenient force fields to compute thermal conductance has been promising [130]. Since the molecular junction is at non-equilibrium during the experiments, we chose to perform our MD calculation using the NEMD method. The thermoelectric properties of single molecular junctions have been exhaustively studied. However, most of these studies are focused on linear molecules like OPE3-Ph or alkane-based molecular junctions. Here, cross-linked molecules were elected as having a dimer will increase the electronic transmission compared with a linear single molecule, consequently, the thermopower of the molecule. Also, the bridge

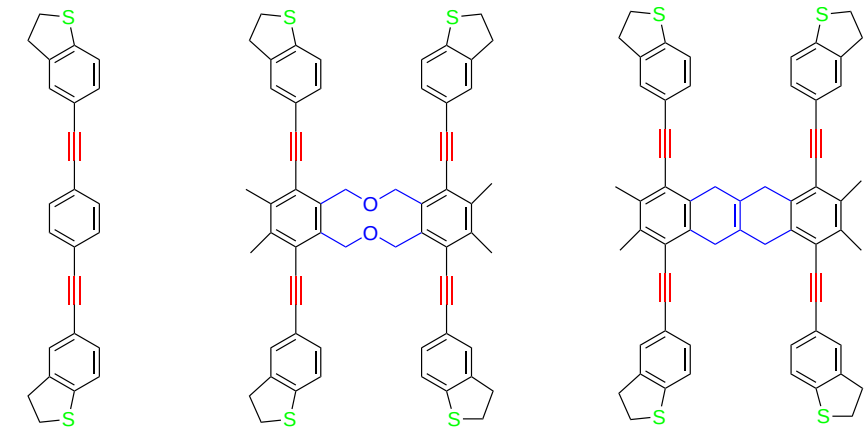

Figure 5.1: The structure of the OPE3 derivatives studied in this chapter

at the cross-linked molecules may diffuses phonons and decrease the thermal conductance. Moreover, studying cross-linked molecules is a way to go beyond single molecule junctions and fabricate thin films [131]. Additionally, this study may be considered as a first step to look at more complex molecular junctions.

In this chapter, we compute the single-molecule electronic and thermal conductance, thermopower and finally the thermoelectric efficiency of cross-linked OPE3 derivatives where three corresponds to the number of phenylene rings in the backbone. The structure of these molecules is shown in Fig.5.1. OPE3-CD, where CD stands for constrained dimer, contains two OPE-Ph which are cross-linked by an oxygen bridge. OPE3-CDR, where CDR means constrained dimer rigid, consists of two OPE-Ph which are connected by double bonded carbon atoms. The wide agreement between electronic conductance data obtained for OPE3 junctions by different research groups, makes this an excellent candidate for a systematic study on the influence of cross-linking. Using NEMD [130], DFT and DFTB, the calculations were performed to predict the thermoelectric efficiency of these molecules. We show that these molecules show the transport properties that are needed for thermoelectric applications.

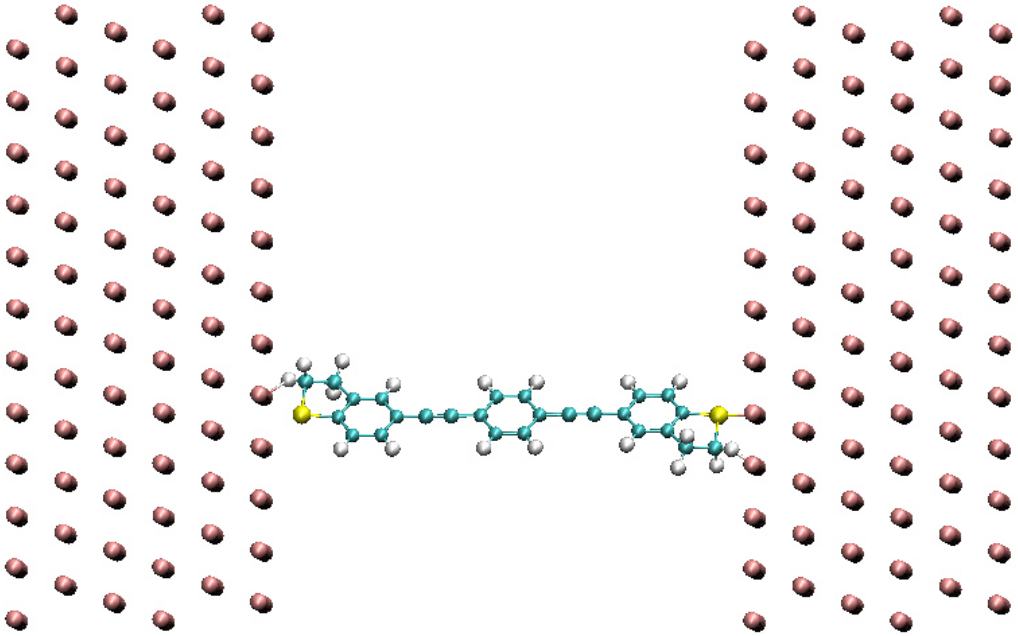

Figure 5.2: The Au(111)-OPE3-Ph-Au(111) junction used in MD calculations

5.1 Thermal transport of dimer molecular junctions of OPE3 derivatives

To compute the heat conductance across OPE3 derivatives, an Au(111)-OPE3-Ph-Au(111) junction was prepared in multiple steps. First, the molecule in the gas phase was optimized using DFT and the NWCHEM package. The calculation was performed using a 6-31G* basis set. Using Atomic Simulation Environment (ASE) [126], the molecule was fixed between two Au(111) surfaces accommodating six layers with 144 atoms per layer. For an illustration see Fig.5.2.

The molecular dynamic calculations were performed considering the OPLS force field and using the Large-scale Atomic/Molecular Massively Parallel Simulator (LAMMPS) package. For the interaction between the gold surface and sulfur atoms we used the force field parameters of the Morse potential defined as

$$V_{Morse}(R_{IJ}) = D_0\Big(\exp^{2\alpha(R_{IJ}-R_{eq})} - 2\exp^{\alpha(R_{IJ}-R_{eq})} \Big), \tag{5.1}$$

atom type	characteristic
Au	any atom in the surface
C*	sp^2 aromatic in 5-membered ring next to two carbons
CA	any aromatic sp^2 carbon
CT	any aromatic sp^3 carbon
H1	H attached to aliphatic carbon with one electron-withdrawing substituent
HA	H attached to aromatic carbon
HC	H attached to aliphatic carbon with no electron-withdrawing substituent
O	sp^3 oxygen in ethers
S	sulfur in methionine and cysteine

Table 5.1: OPLS force field atomic characteristic

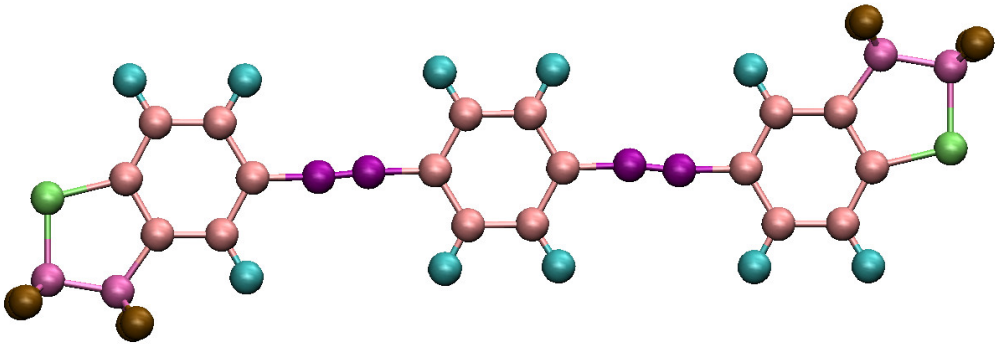

Figure 5.3: An illustration of OPE3-Ph molecule where using OPLS force field atomic characteristic. Where the peach, purple, blue, green, brown and pink corresponds to CA, CT, HA, S, HC, C*

where D_0 is the well depth akin to the molecule dissociation energy, and α is associated with the curvature of the potential at the equilibrium distance [5, 132, 133]. All the force field parameters are listed in Table.5.1 to 5.6. Additionally, an illustration of different atom types in OPLS force field has been shown for OPE3-Ph in Fig.5.3.

atom type	R_{IJ}(Å)	ϵ(kcal/mol)	atom type	R_{IJ}(Å)	ϵ(kcal/mol)
Au	5.29	2.63	H1	0.0150	1.387
C*	0.0860	1.7	HA	0.0157	1.4870
CA	0.0860	1.7	HC	0.0150	1.459
CT	0.0860	1.7	O	0.1700	1.6837
CTr	0.0860	1.7	S	0.2500	2.0000

Table 5.2: OPLS force field Van der Waals parameters

Bond type	k_r(kcal/(mol Å^2))	R_{eq}(Å)	Bond type	k_r(kcal/(mol Å^2))	R_{eq}(Å)
CA-CA	469	1.400	C*-CA	317	1.495
C*-S	227	1.810	C*-C*	367	1.52
C*-HC	367	1.080	CA-S	227	1.810
CA-HA	367	1.080	CA-CT	469	1.400
CTr-CA	20	1.400	CT-H1	331	1.09
CTr-CTr	800	1.100	CT-OS	313	1.405

Table 5.3: OPLS force field bond parameters

pair	D_0(kcal/mol)	α(Å^{-1})	R_{eq}(Å)
Au-S	9.04	1.378	2.903

Table 5.4: Morse potential parameters [5]

Angle type	K_θ (kcal/(mol radian^2))	θ°_{eq}	Angle type	K_θ (kcal/(mol radian^2))	θ°_{eq}
C*-C*-CA	50	114.70	CA-CA-S	62.1	122.55
C*-C*-HC	35	110.5	CA-CT-H1	35	120
C*-C*-S	50	114.70	CA-CT-OS	80.0	109.5
C*-CA-CA	63	120	CA-CTr-CT	63	180.0
C*-S-CA	63	134	CT-OS-CT	100.0	111.8
CA-C*-HC	35	111.2	H1-CT-H1	35	106
CA-CA-CA	63	120	H1-CT-OS	80.0	109.5
CA-CA-CT	63	120	HC-C*-HC	35	106
CA-CA-CTr	63	120	HC-C*-S	48.2	119.88
CA-CA-HA	35	120	Au-S-C*	50	107.285

Table 5.5: OPLS force field angle parameters

torsion	f	K_ϕ(kcal/mol)	ϕ°	torsion	f	K_ϕ(kcal/mol)	ϕ°
X-C*-CA-X	4	14.500	180.0	X-CTr-CTr-X	4	14.500	180.0
X-CA-CA-X	4	14.500	180.0	X-CA-S-X	3	1.8000	180.0
X-C*-C*-X	4	14.500	180.0	X-CT-OS-X	3	1.8000	180.0
X-CA-CT-X	4	14.500	180.0	X-C*-S-X	3	1.8000	180.0
X-CA-CTr-X	4	14.500	180.0				

Table 5.6: OPLS force field torsion parameters

5.1.1 Thermal conductance for OPE-Ph

The timestep was set to 0.01 fs, and after a energy minimization procedure, the center of mass of the two surfaces were tethered to be fixed at their position by soft springs. Next, the junction was equilibrated at room temperature in the NPT ensemble for 1 ns. To obtain reasonable statistics, the calculation was performed for 40 independent configurations. For each configuration the initial velocities had been generated randomly. It should be noted that one can always run the calculations for more configurations and decrease the uncertainty of the results.

After equilibration, we performed the thermal conductance calculations for 2 ns using the steady state method. For the temperature difference between the walls, we verified linearity of thermal conductance for a temperature difference of 100 K, accordingly the temperature difference between the gold surfaces was set to 100 K for all the calculations. At last, the accumulated energy of the hot (cold) gold surface, hot (cold) thermostat, versus time were plotted as shown in Fig.5.4a. A linear fit to the data determined the slope of the plot and it was used to compute the heat conductance from the Eq.2.14. An OPE3-Ph thermal conductance histogram at room temperature is shown in Fig.5.4b, hence, thermal conductance at room temperature is 21.99 $\pm$ 3.8 pW/K, where the first value is the thermal conductance and the second value shows the uncertainty in our simulations. This result shows a good agreement with the experimental value 20 $\pm$ 6 pW/K measured for the same molecule junction [4].

5.1.2 Scaling behaviour of OPEn-Ph derivatives molecular junction thermal conductance

The analysis was performed for OPE3 and the constrained dimer of the molecule, now denoted OPE3CD (see Fig.5.1). The impact of temperature was studied to determine if thermal transport is ballistic or diffusive. If it is ballistic, thermal conductance is expected to be independent of temperature (in classical molecular

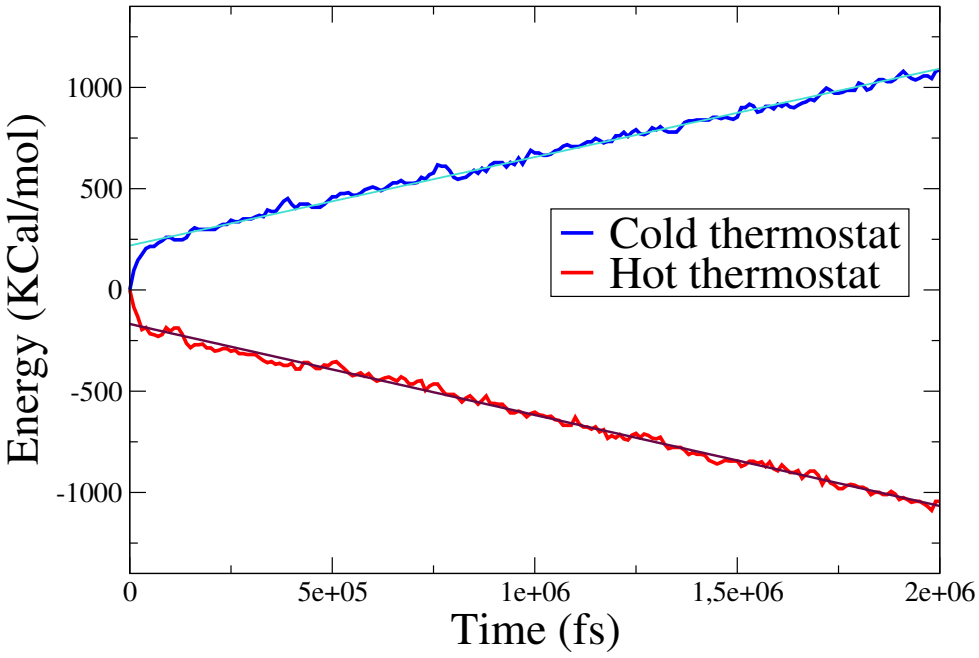

(a)

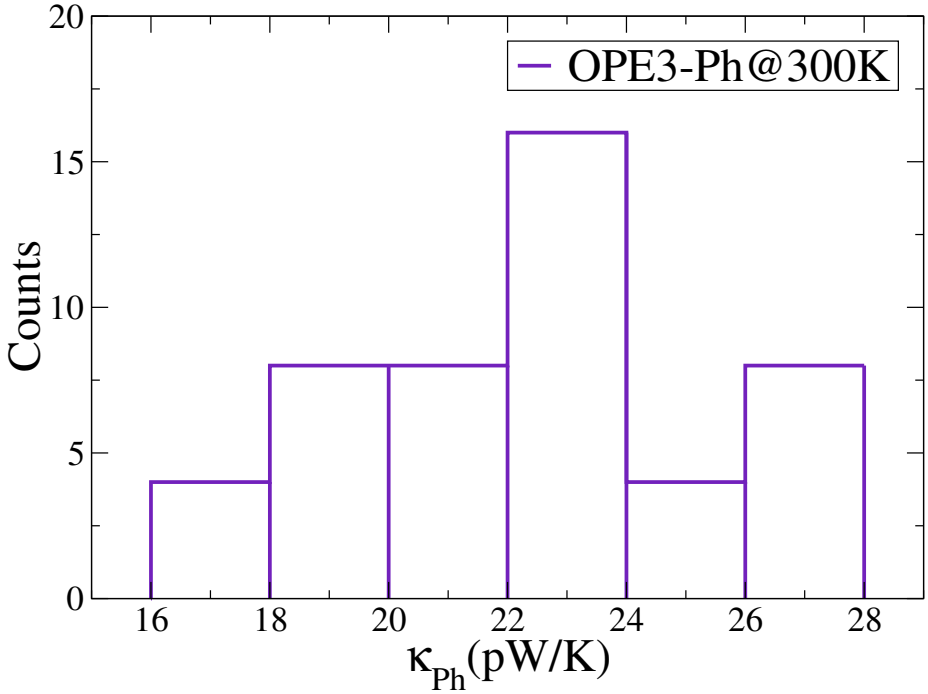

(b)

Figure 5.4: Total accumulated energy versus time for Au(111)-OPE3-Ph-Au(111) when the temperature difference between the gold surfaces is $\Delta T = 100$ K and b) The histogram of thermal conductance for OPE3-Ph at 300 K(40 seeds)

dynamics simulations, quantum effects are absent and all vibrational modes are populated at any temperature). On the contrary, if the heat carriers are scattered between the two heat reservoirs, one expects a thermal conductance decreasing with temperature. As shown in Fig.5.5a, the value of thermal transport for the dimers is twice the one of OPE3-Ph. This result is also validated by our thermal transmission spectrum for the OPE3-Ph derivatives as shown in Fig.(5.6)

Moreover, Fig.5.5a indicates that thermal conductance is almost independent on temperature for OPE3-Ph and OPE3-CDR derivatives, thence, the thermal transport is certainly ballistic. The nature of thermal transport can also be evidenced by length-dependent simulations. We performed thermal conductance calculation for different lengths of OPEn-Ph derivatives (n=3,4,5). As can be seen in Fig.5.5b, for OPEn-Ph and OPEn-CDR molecules, the thermal conductance is almost constant, which is again consistent with the ballistic nature of thermal transport. It should be noted, in the case of OPE4-CD and OPE5-CD, we do not observe a ballistic behaviour. It may happen that in these cases, the phonon mean free path is smaller than the molecule length. Phonon mean free path depends on the nature of the bridge in the cross-linked molecules as well as the molecular architecture. To confirm this, one would need to calculate phonon lifetime and phonon mean free path for each structure. Due to the lack of time, for the moment we did not do this step. So far, most of the studies on heat transport in single molecular junctions focused on linear molecules [134, 135, 131]. Therefore, we need further investigations to comprehend the transport mechanism in cross-linked molecules.

To interpret the relative values of the conductance of the junctions, we obtained transmission spectrum corresponding to OPE3 derivatives during thermal conductance calculations. The transmission spectrum is a measure of the transmission through the sulfur-gold bond at the hot surface. More precisely, it is defined by [87]:

$$q(\omega) = \frac{1}{\Delta t} \sum_{i \in Au, j \in S} \tilde{f}_{ij,\alpha}(\omega) \tilde{v}^{*}_{i,\alpha}(\omega) \tag{5.2}$$

where Δt is the interval between two configuration saving, the sum runs over

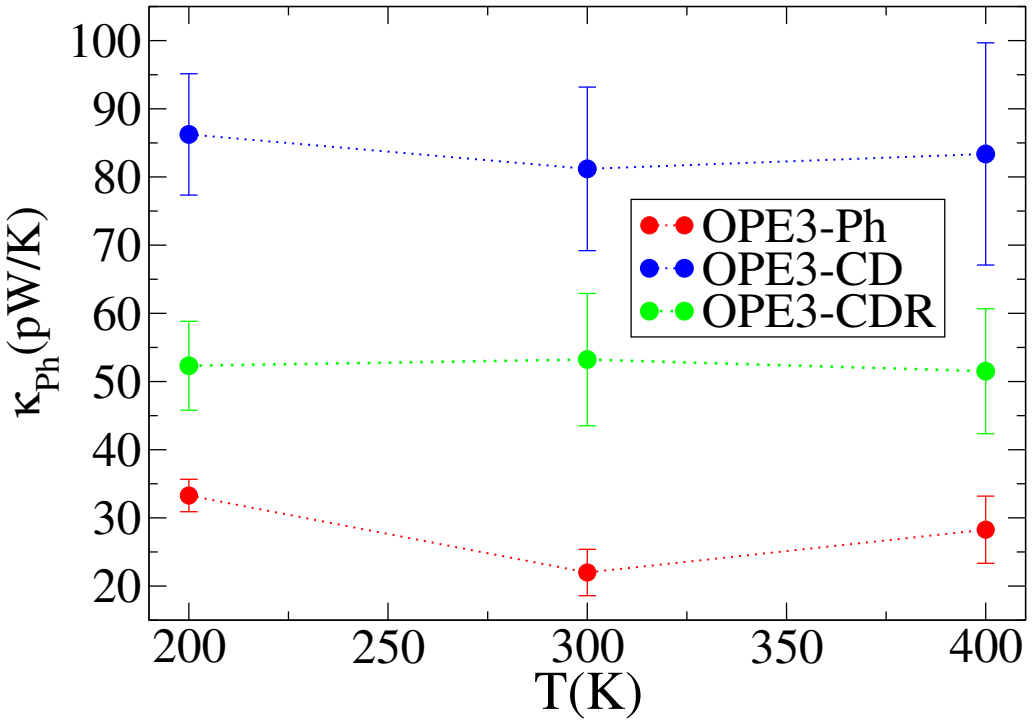

(a)

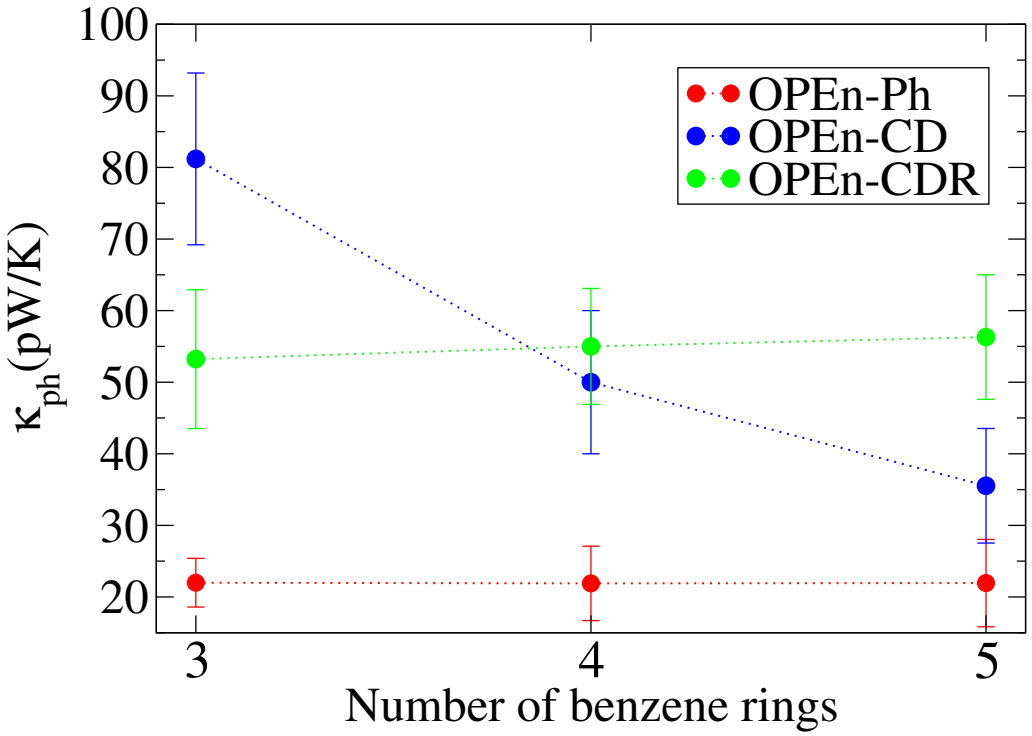

(b)

Figure 5.5: a) Thermal conductance vs temperature for OPE3 derivatives b) Thermal conductance vs length for OPEn derivatives at 300 K

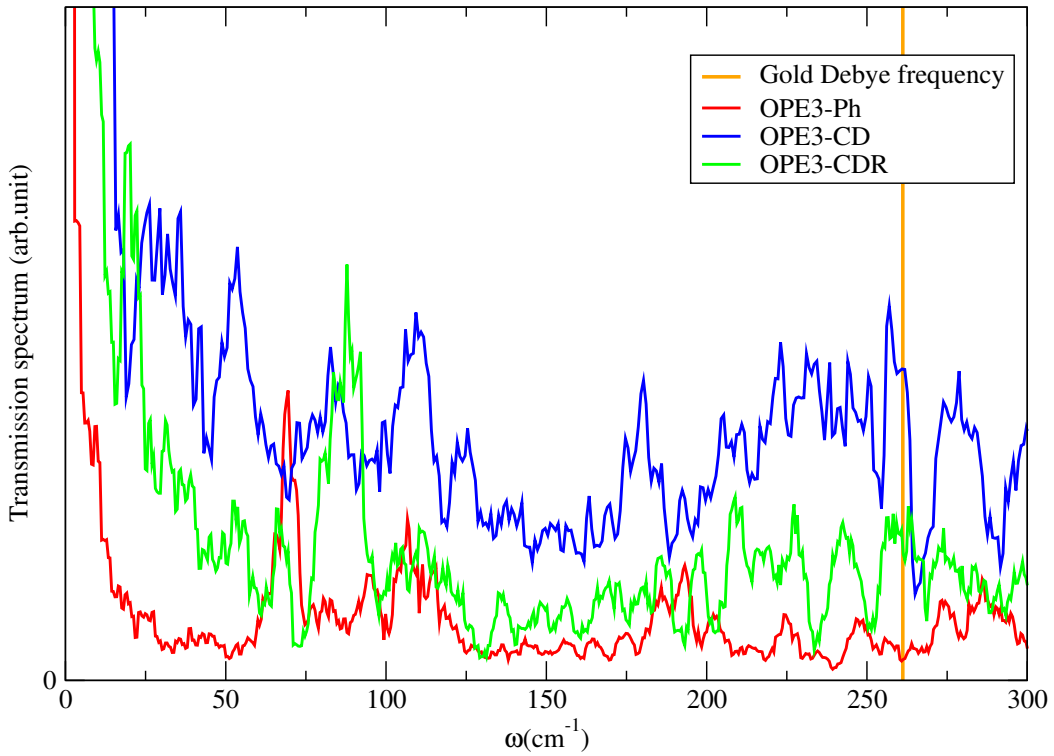

Figure 5.6: The transmission spectrum during thermal conductance calculations for OPE3 derivatives averaged for 10 seeds at 300 K

all sulfur-gold bonds, $\tilde{f}_{ij,\alpha}(\omega)$ is the time-Fourier transform of the bonding force between a sulfur atom and one of its gold neighbour, $\tilde{v}_{i,\alpha}(\omega)$ is the time Fourier transform of the velocity of atom i, α denotes a spatial direction $\alpha \in x, y, z$ and $*$ denotes the conjugate of a complex number.

We computed the transmission spectrum for 10 independent configurations at room temperature using eq.5.2. The MD calculation was done in the NVE ensemble and we recorded the system dynamics every 100 fs to map over all the possible frequencies for the junctions. The average transmission spectrum for OPE3 derivatives is shown in Fig.5.6. The OPE3-CD transmission dominates at most of the frequencies over OPE3-Ph and OPE3-CDR. All the modes with the frequency less than the Debye frequency of gold (shown in Fig.5.6) contribute to thermal conductance. In Fig.5.5a, we can see that the value for thermal conductance of OPE3-CDR is almost twice of the one of OPE3-Ph. On the other hand, OPE3-CD shows a higher thermal conductance compared with OPE3-Ph. The transmission spectrum

of OPE3 derivatives, confirms this results.

5.2 Electronic transport of dimer molecular junctions of OPE3 derivatives

In this section, we investigate the electronic transport of OPE3 derivatives introduced in this chapter. The electronic properties of OPEn-Ph, where n denotes to the number of phenylene rings in the backbone, were computed using NEGF-DFTB having the same settings as in section 4.3. The devices were constructed in the same fashion. However, when checking the scaling behaviour, the different oligomers were not fully relaxed to keep them planar, in order to address the influence of chain length without interplay with additional structural effects. As the dimer molecules are larger than monomers, to have at least 9 Å distance between the molecule and its periodic image, we need a larger surface area. So, the Au_{20}-molecule-Au_{20} was fixed between two Au(111) surface accommodating three layers with 36 atoms per layer.

5.2.1 Scaling behaviour of OPEn-Ph molecular junction electronic conductance

In order to investigate the scaling behavior of the molecular devices, we computed the conductance for OPEn-Ph oligomers having different lengths (n=3...6). The electronic transmission is shown in Fig.5.7a, while the corresponding conductance is given in Fig. 5.7b.

In agreement with the literature, [93], we observe an exponential decay of the electrical conductance as a function of the length L, indicating that minimizing the length L is required for high electron transport. Writing the conductance

$$G(L) = A \exp^{-\xi L}, \tag{5.3}$$

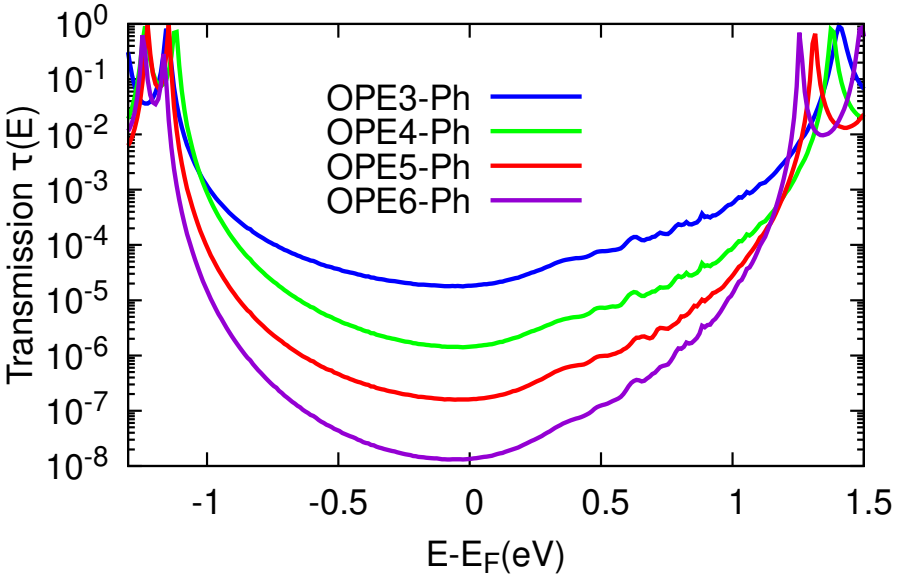

(a)

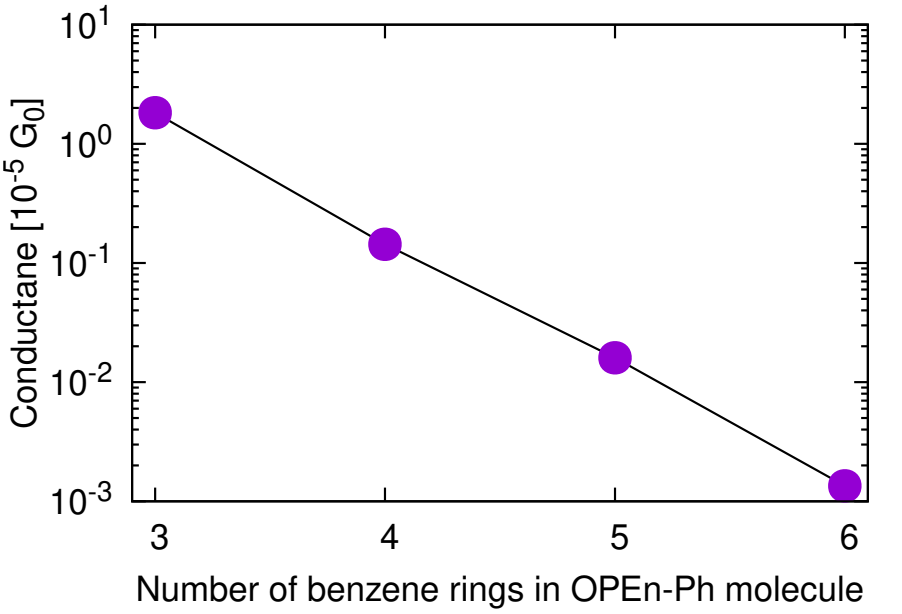

(b)

Figure 5.7: a) Electronic transmission function and b) electrical conductance at 300 K as a function of the number of benzene rings in the OPEn-Ph oligomers

where A is a prefactor which depends on the order of magnitude of the conductance value, what does it mean ? ,and the attenuation factor ξ is expected to depend on the chemical nature of the molecules (conjugated vs. saturated), the presence of electrophilic/electrophobic side groups and to a lower extent on the anchor groups [136]. We find $\xi = 0.35$ Å^{-1}, which agrees with the findings for other conjugated molecules [137, 138]. The transport characteristics are thus well described by sequential tunnelling model from ring to ring without reflection.

5.2.2 NEGF-DFTB calculations for junctions of OPE3 derivatives

The energy-dependent transmission function $\tau(E)$ of the OPE3 derivatives is shown in Fig.5.8. In both OPE3-CD and OPE3-CDR, the bridge attached to the central OPE3 ring has a crucial role in the HOMO position which results in the HOMO shift of approximately 0.4 eV with respect to OPE3-Ph. For the LUMO, a shift of 0.1 eV towards E_F is seen for both dimer molecules. The value of the transmission at LUMO stays the same for all three molecules, but the width is clearly larger for the dimers. As shown in Table.5.7, the conductance value for the dimers rises by a factor of six with respect to the monomer, not by a factor of two as one would possibly expect. The maximum conductance value is observed in OPE3-CD with 7.05 $\times 10^{-4} G_0$. The Seebeck coefficient is negative for all the OPE3 derivatives as the transport occurs through the LUMO [110]. The absolute value of the Seebeck coefficients for the dimers increase compared with OPE3-Ph (see Table.5.7).

Some more analysis have been done to investigate the origin of the unusual rise in the conductance values. Inspection of Fig. 5.8 reveals that there is a resonance at 0.5 eV below the Fermi energy. To address the origin of this resonance, a molecular orbital analysis was done for Au_{20}-OPE3-Ph-Au_{20} and OPE3-Ph in the gas phase. The HOMO and LUMO energy levels for OPE3-Ph in the gas phase are shown in Fig.5.9a and 5.9b, respectively. The corresponding molecular orbitals in the Au_{20}-OPE3-Ph-Au_{20} complex were identified as shown in Fig.5.9c and 5.9d.

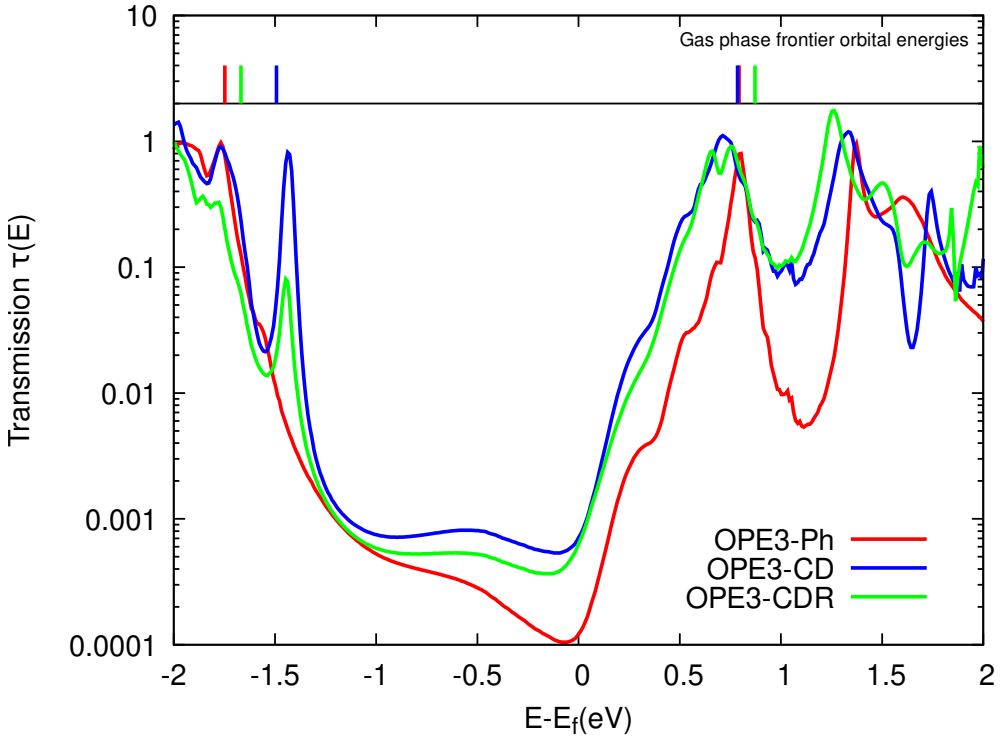

Figure 5.8: NEGF-DFTB transmission function $\tau(E)$ for the three OPE3 derivatives. For illustration the HOMO and LUMO energies of the isolated molecules in the gas phase are at the top of the plot. The gas phase energy levels are shifted by a Δ to be aligned with Fermi energy of the substrate, where Δ is the difference between the middle of HOMO-LUMO gap for the device and the molecule. We calculated Δ (OPE3-Ph)$= -1.30eV$,Δ (OPE3-CD)$= -1.45eV$, and Δ (OPE3-CDR)$= -1.22eV$.

Next, we searched for new molecular orbitals between these two energy levels which have a high contribution from the molecule and are absent in the bare OPE3-Ph compound. This new levels are shown in Fig.5.9e and 5.9f and their energy difference with respect to Fermi energy is about -0.6 eV. The energy difference of these energy levels with Fermi energy is about -0.6 eV. Our analysis shows that these molecular orbitals are due to the coupling of the molecule with leads, specifically, the d orbital of Sulfur atoms in OPE3-Ph couples with the d orbital of gold atoms in Au_{20}. All things considered, we notice three main reason for the significant increase in the conductance values. In the dimers the LUMO is shifted towards the Fermi energy. Furthermore, the transmission at LUMO is broadened. Finally,

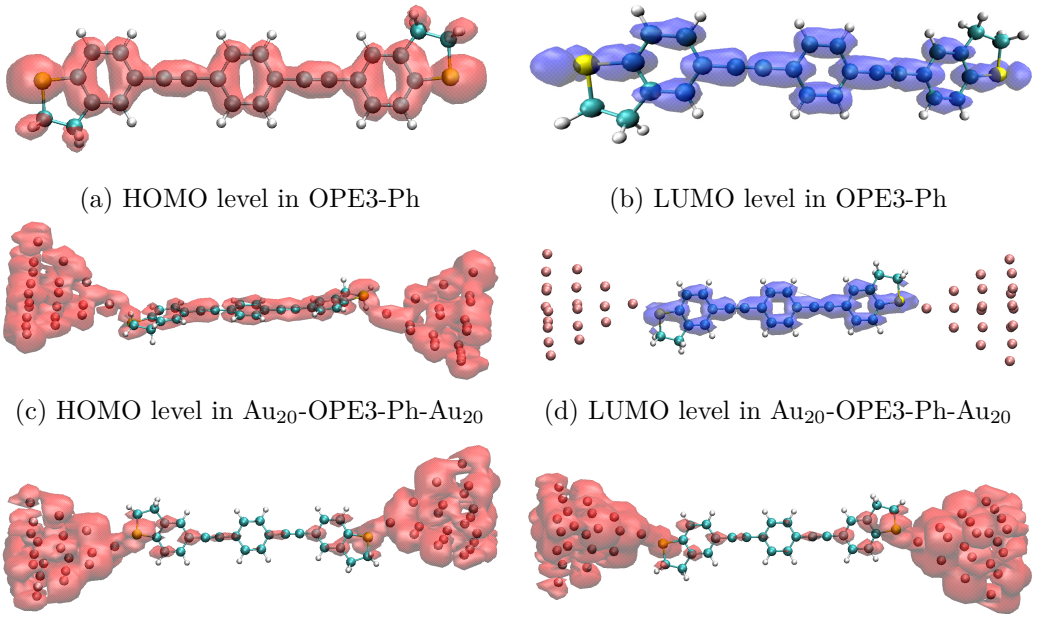

(a) HOMO level in OPE3-Ph

(b) LUMO level in OPE3-Ph

(c) HOMO level in Au_{20}-OPE3-Ph-Au_{20}

(d) LUMO level in Au_{20}-OPE3-Ph-Au_{20}

(e) HOMO-1 level of Au_{20}-OPE3-Ph-Au_{20} with energy of E-E_F=-0.59 eV

(f) HOMO level of Au_{20}-OPE3-Ph-Au_{20} with energy of E-E_F=-0.58 eV

Figure 5.9: Molecular orbital analysis for OPE3-Ph and Au_{20}-OPE3-Au_{20}

there are new molecular states at the complex that seem to be more conductive for the dimers.

5.3 Thermoelectric efficiency of dimer molecular junctions of OPE3 derivatives

The figure of merit ZT for the different dimer molecular junctions were calculated following the section 3.2. The calculated transmission may be used to estimate the electronic thermal conductivity using equation 3.8. The Wiedemann–Franz law states that the electronic thermal conductivity could be estimated by [10]

$$\kappa_{el} \approx \frac{\pi^2 k_B^2}{3e^2} GT, \tag{5.4}$$

where G is the electrical conductance, and T is the temperature. As shown in Table.5.7, we calculated the value of κ_{el} for OPE3 derivatives at room temperature. Overall, the values of κ_{el} are negligible compared with κ_{ph}. This means that

Structure	G $[10^{-4}G_0]$	S $[\mu V/K]$	κ_{ph} $[pW/K]$	κ_{el} $[pW/K]$	ZT $\times 10^{-4}$
OPE3-Ph	1.2	-36.80	21.99±3.8	0.069	1.72
OPE3-CD	7.05	-47.50	81.19±12	0.399	4.55
OPE3-CDR	6.30	-62.79	53.22±9.7	0.356	10.83

Table 5.7: Electronic conductance, Seebeck coefficient, phonon and electron contribution to thermal transport and figure of merit for different OPE3 derivatives at 300 K

.

thermal transport across the molecules we consider is mainly mediated by phonons. Finally, the figure of merit ZT were calculated from Eq. 3.7. The results for room temperature are shown in Table.5.7. The figure of merit for OPE3-Ph, OPE3-CD and OPE3-CDR is 1.72×10^{-4}, 4.55×10^{-4}, and 10.83×10^{-4}, respectively.

It would be desirable to sample a larger space of metal–molecule geometries to approach the experimental conditions, but already at this stage, the theoretical simulations confirm the main transport mechanism and thermal conductance values of OPE3-Ph. As the value of electronic conductance and Seebeck coefficient are overestimated in DFT and DFTB, there is variability in the values of thermopower and ZT.

We should mention the values we obtained for figure of merit ZT of the OPE3 derivative junctions in this chapter are relatively large compared with the values obtained for other organic molecular junctions [139, 140, 141]. One of the most challenging aspects of computing thermoelectric efficiency of the molecular junctions using DFT (or DFTB), is the quantitative control of electronic predictions. In general, in ab-initio calculations, the alignment between molecular energy levels and Fermi energy of the metallic surface in the junctions is not controlled, and therefore leads to inaccuracy of electronic transport properties. The disparity comes from inaccuracy of the conventional exchange-correlation functionals. A sufficient approach to get the agreement between DFT calculations and experiments has been a great challenge in quantum chemistry and material science. Despite of all the effort done to develop methods to overcome these challenges, their applica-

tion encounters limits due to the computational cost [102]. However, we emphasize that DFT calculations accompany the experiments as they can predict the most favourable bonding configuration, the nature of transport, which molecular orbital influence the conductance, and last but not least the trends of experimental data can often be predicted accurately [142].

In summary, we investigated the thermoelectric properties of cross-linked derivatives of OPE3-Ph molecular junctions. Regarding the thermal transport, we found that it may increase at the most by a factor of three. Concerning the electronic transport, the relative increase may reach factor six as seen for OPE3-CD and OPE3-CDR. The figure of merit of cross-linked molecules may take relatively high values, as observed for the OPE3-CDR junction.

Chapter 6

Out of equilibrium current-voltage characteristics and dissipated heat

"When matter is becoming disturbed by non-equilibrium conditions it organizes itself, it wakes up. It happens that our world is a non-equilibrium system"

— Ilya Prigogine

The advance of experimental techniques to measure the transport properties of molecular junctions has motivated many theoreticians to investigate these molecular systems [143]. Most theoretical studies for single molecular junctions have been done considering the system at equilibrium [144]. However, to take advantage of a molecular junction, identifying charge and energy transport out of equilibrium is a necessity [12, 108]. Studying current-voltage (I-V) characteristics of molecular junctions gives us a fundamental insight of transport mechanism through molecular junctions at non-equilibrium [141, 145, 146, 147]. It has been shown that the I-V curves in molecular junctions are considerably dependent on the molecule-substrate contact [148]. First principle calculations are a powerful tool that can be used along with the experiment. It has been proven that the NEGF method is applicable to calculate electronic properties of single molecular junctions. It has been observed that these calculations predict the complexity of electronic conductance through single molecular junctions which can not be reached by standard circuit theor-

ies [149, 150, 151]. Moreover, recent experimental and theoretical studies made it possible to measure and compute Peltier cooling in molecular junctions, which is crucial to develop molecular-based cooling systems [3]. Applying an electrical current flow to molecular junctions can generate refrigeration if Peltier cooling is larger than Joule heating [3, 152].

In this chapter, the out of equilibrium characteristics of the OPE3 derivatives shown in Fig.4.1 have been investigated. The I-V characteristics of OPE3 derivatives were computed using DFTB. Furthermore, the bias dependent electronic transmission computed in DFTB is used to calculate the Peltier heat dissipated in the leads. Then, aligning the Fermi energy, the optimal cooling/heating power is obtained. At the end, an electro-thermal circuit model will be introduced to calculate the optimal temperature difference between the two leads in the molecular junctions.

6.1 Current-Voltage characteristics

NEGF-DFTB was employed to compute the thermoelectric properties of OPE3 derivatives out of equilibrium. The same molecular junctions as discussed in Sec.4.3 were used. A finite symmetric bias was applied to both leads such as the chemical potential of the right and the left and the right lead for a negative voltage V changed to $\mu_R = E_F - \frac{V}{2}$ and $\mu_L = E_F + \frac{V}{2}$, respectively. Hence, a current flows from the left lead to the right lead [3]. For the bias calculations, the transmission should be converge with respect to the point sampling of the real axis in the Green's solver. As it turned out the default values was sufficient. As for the rest of the parameters, we used the same setup as in Sec.4.3. For OPE3-Ph, the current values were obtained in a ± 1 V bias range. At higher bias values, the calculations for the junctions did not converge. It is also experimentally challenging to realize the I-V at high bias voltages.

Firstly, the potential in the device region was evaluated for the OPE3-Ph junction under bias and was compared with the junction at equilibrium. As shown in Fig.6.1,

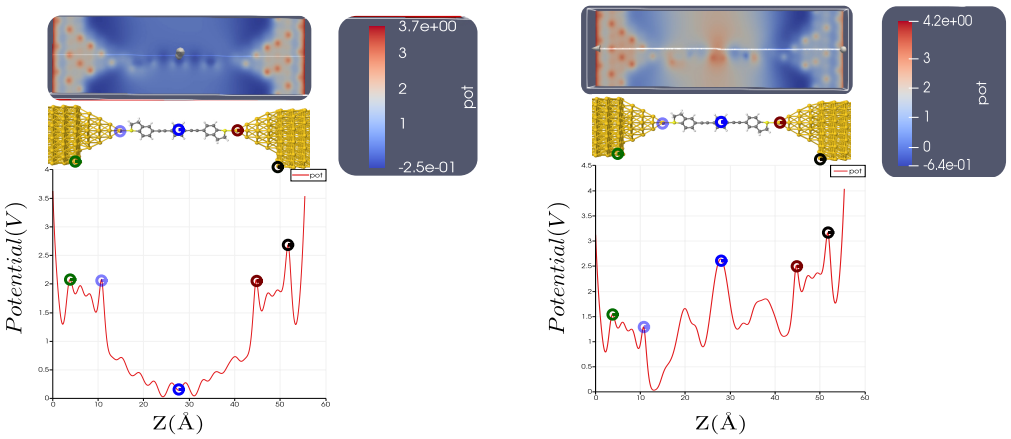

(a) OPE3-Ph under bias 0 V

(b) OPE3-Ph under bias -1 V

Figure 6.1: The potential in the device region for OPE3-Ph where the small circles with the same color show the same coordinate in z direction. The color map shows the potential value in the device region.

at equilibrium the potential is nearly symmetrical with respect to the center of the molecule, which is expected as the device is symmetrical. However, for the junction under bias, the potential drops linearly along the molecule with fluctuations on the atomic scale and there are larger changes at the interface. It should be noted that ideally, the potential in the metallic surfaces should be constant, but as the simulated system is not large we see some perturbation and fluctuations in the potential.

The transmission was computed for OPE3 derivatives under bias. The result is shown for OPE3-Ph in Fig.6.2a. The higher the bias value, the more perturbation occurs in the transmission. Furthermore, there is a notable change in the transmission at 0.5 V bias due to the energy level at -0.5 eV.

The I-V curves for OPE3 derivatives are shown in Fig.6.2b. In general, the I-V characteristics of OPE3 derivatives junctions are nonlinear, as reported for other organic molecular junctions [103, 153, 103]. Additionally, the symmetry of I-V curves proves that the coupling to the left and right leads is very similar in our transport device [153]. As the bias value increases, OPE3-An and OPE3-PhOMe$_2$ show a higher value of current compared with OPE3-Ph. For instance at bias 0.7

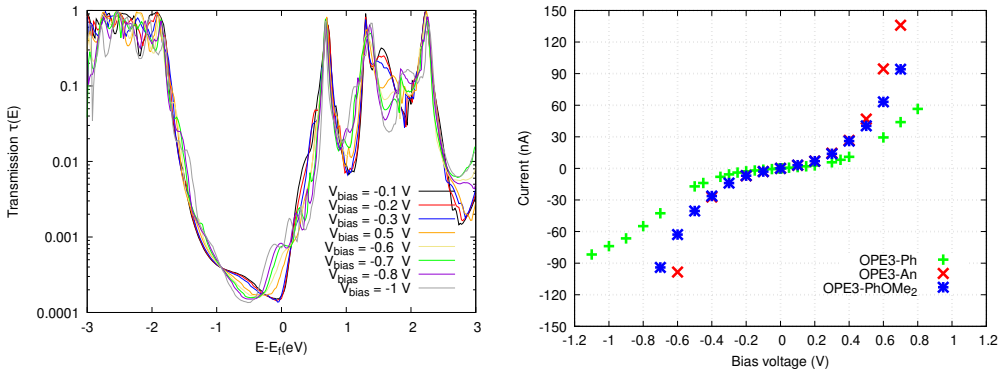

(a) (b)

Figure 6.2: a) Evolution of the electronic transmission under bias for OPE3-Ph. b) The current as a function of bias for OPE3 derivatives.

Molecule	HOMO-LUMO gap (eV) DFT/PBE	HOMO-LUMO gap (eV) DFTB
OPE3-Ph	2.10	2.54
OPE3-PhOMe$_2$	2.11	2.32
OPE3-An	1.43	1.58

Table 6.1: HOMO-LUMO gap for OPE3 derivatives obtained by DFT-PBE and DFTB in the gas phase

V, the highest value of current is 135.95 nA which is observed for OPE3-An. We predicted higher current values in presence of side groups for OPE3.

Note that, in DFT based transport calculations, the absolute value of current is overestimated as shown by Darancet and coworkers [12]. Yet, one should keep in mind that in their work, they have predicted I-V characteristics of molecular junctions using DFT-PBE method, while we used DFTB, hence, there is a large quantitative difference between our results for the absolute value of current. One of the reasons is that the DFTB HOMO-LUMO gaps are generally larger than the DFT-PBE ones, hence, the conductance in DFTB is closer to the experiments, consequently, the current values are closer to the experiments as well. To do a comparison, in Table.6.1, we compare the gas phase HOMO-LUMO band gaps for the OPE3 derivatives performed by DFTB+ and Nwchem with PBE exchange-correlation functional using a 6-31G* basis set. Additionally, while working with DFT, the basis set is larger compared to DFTB which leads to stronger coupling

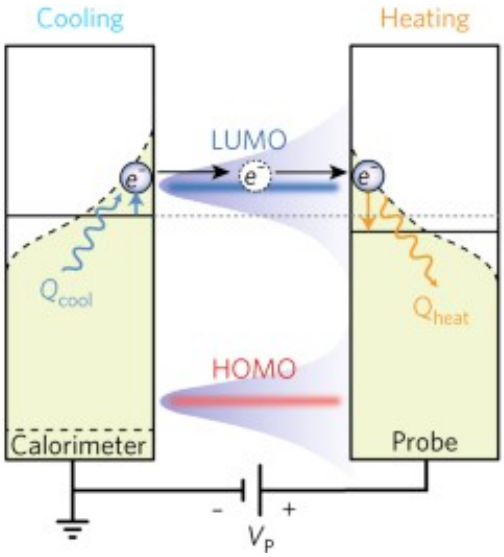

Figure 6.3: An illustration of the Peltier effect in LUMO-dominated molecular junctions levels. Q_{cool} and Q_{heat} denote cooling and heating power, respectively. The Lorentzian shapes around HOMO and LUMO show the transmission [3].

between the molecule and the lead.

6.2 Heat dissipation out of equilibrium

The bias dependent transmission was used to calculate the heat dissipated in the left lead from Eq.3.2. As mentioned in Sec.5.3, in DFTB calculations, there are some errors in the alignment between molecular energy levels and Fermi energy of the metallic surface in the junctions. In order to further explore the parameter space, we also performed simulations for a shifted Fermi energy that is closer to the LUMO resonance. In experiment a shift could be realized by gating the voltage. After applying a negative bias voltage, a current flows from the left lead to the right lead. In another word, electrons having the energy are injected to the right lead and leave the left lead. The charge flow happens in the energy range between the chemical potentials of the leads and in a small range above the chemical potential of the right lead and below the chemical potential of the left lead. As shown in Fig. 6.3, cooling in the left lead only happens when the electrons flow below the

Molecule	bias (V)	optimal P_L (pW) (E_F DFTB)	bias (V)	optimal E_F shift (eV)	optimal P_L (nW) (optimal E_F)
OPE3-Ph	0.01	-0.64	-0.04	0.8	-8.25
OPE3-PhOMe$_2$	0.01	-2.48	-0.03	0.9	-9.29
OPE3-An	0.02	-5.92	0.06	0.3	-11.29

Table 6.2: The optimal cooling for OPE3 derivatives ($T_L = T_R = 300$ K)

chemical potential of the left lead. Therefore, to reach net cooling in the left lead, the electrons which transmit above the chemical potential of the right lead should dominate. This can happen only when the transmission probabilities are larger at $\mu_L + V/2$ than the ones of $\mu_R - V/2$, i.e. the LUMO dominated transmissions [3]. The calculations were done for OPE3 derivatives. The results are shown in Fig.6.4a, 6.4c, and 6.4e. As expected for LUMO based transport, the highest cooling occurs for OPE3-An, due to the fact that the Fermi level is closer to LUMO compared with other derivatives (see Fig.4.7).

By varying the temperature difference ($\Delta T = T_L - T_R$) between the two leads, the bias dependent Peltier heat in the left lead was computed. As shown in Fig.6.4b, 6.4d, and 6.4f the cooling in this case is rather small compared with when we shift the Fermi level towards LUMO. The results indicate that net cooling is possible in a narrow voltage range around zero bias, which can be significantly enlarged by shifting the Fermi energy towards LUMO. The result shows that in such a scenario the cooling power is greatly increased.

The bias dependent transmission $\tau(E, V)$ was interpolated for all the bias values between the data points. The total power was optimized with respect to the interpolated transmission function for the Fermi energy predicted by the DFTB calculation. Hence, the optimal bias and corresponding optimal P_L were found. Additionally, the Fermi level was shifted towards the LUMO and once again the optimal bias and power were found.

The optimal cooling values and the corresponding voltages as well as optimal Fermi shifts are written in Table.6.2. The highest cooling value is -11.29 nW, which

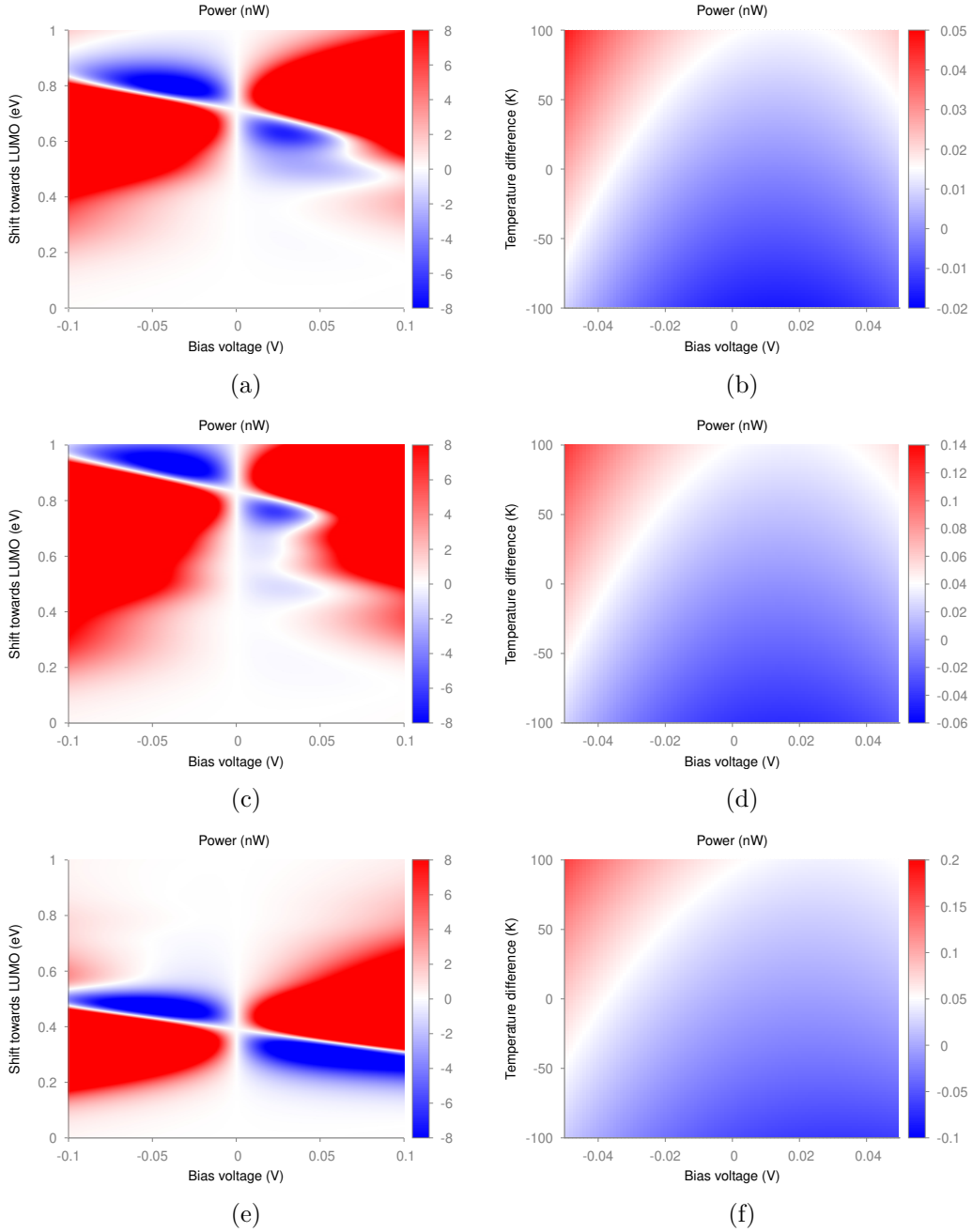

Figure 6.4: The bias dependent net heating/cooling in OPE3 derivatives ($T_L = T_R = 300$ K) where red shows positive values (heating) and blue shows negative values (cooling) taking to account different values for shifting the Fermi energy towards LUMO for a) OPE3-Ph, c) OPE3-PhOMe$_2$, e) OPE3-An, temperature difference between the leads for b) OPE3-Ph, d) OPE3-PhOMe$_2$, f) OPE3-An.

is observed for OPE3-An for the Fermi shift of 0.3 eV towards LUMO. Overall, the cooling power in OPE3 derivatives studied in this chapter, show relatively larger cooling values compared with other organic single molecular junctions [3]. Once again, it should be noted that DFT overestimation of conductance values and difficulty of effectively gating junctions over high gate voltages leads to the overestimation of cooling values. However, our simulations show that side groups increase the cooling power of OPE3.

6.3 Electro-thermal circuit for OPE3 derivatives

Firstly, we introduce the experimental setup which is used to measure the temperature in the transport device used by our collaborators at IBM [4, 1]. In order to measure heat and charge transport on single molecule scale, a micro-electro-mechanical system (MEMS) was suspended using four silicon nitride beams, as shown in Fig.6.5a. The characteristic thermal conductance of this support has been estimated as $\kappa_{Ph}^{supp} = 10^{-8}$ W/K [154]. In the central membrane of the device, the thermometer and the gold surface are placed. The gold substrate creates an electrical connection with the scanning tunnelling microscope (STM) tip. A gold tip is used to perform the STM-Break Junction (STM-BJ) measurement. The temperature measurements are performed by measuring the resistance of the four beams.

The electro-thermal circuit is shown in Fig. 6.5b. When the net heating power is negative, the left lead cools. However, in the phonon channel, the molecule and the support show thermal conductance. In the experimental setup T_R corresponds to the tip and its temperature stays constant due to the good thermal contact with the environment. Therefore, the temperature of the left lead is $T_L = T_R + \Delta T$. At equilibrium, one has:

$$P_L^{el} + P_{supp}^{th} + P_{mol}^{th} = 0, \tag{6.1}$$

where $P_L^{el} < 0$ is the net heating power due to the electrons in the leads , $P_{supp}^{ph} =$

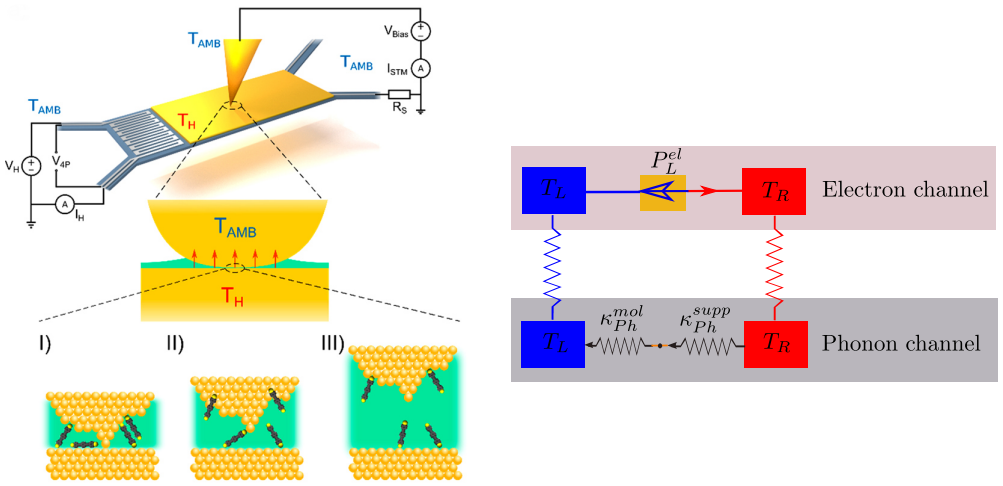

(a) (b)

Figure 6.5: a) Experimental setup used to measure thermal properties of molecular junction [4] b) Illustration of the electro-thermal circuit (inspired from [1])

$\Delta T \kappa_{ph}^{supp}$ is the heat loss due to the support, and $P_{mol}^{ph} = \Delta T \kappa_{mol}^{ph}$ is the backflow of heat along the molecule due to phonons. As we calculated in Sec.5.1, the thermal conductance of the OPE3-Ph junction is 22 pW/K. Note that, even though P_{supp}^{th} and P_{mol}^{th} are assumed to be constant over the temperature range studied, the net heating power in the leads is a function of the temperature difference between the leads as stated in Eq. 3.5.

Having said that, the temperature change between the leads reads

$$\Delta T = \frac{P_L^{el}(\Delta T)}{\kappa_{Ph}^{supp} + \kappa_{Ph}^{mol}} \tag{6.2}$$

which requires a self-consistent solution for ΔT. In our calculations $\Delta T < 0$ changes during the self-consistent cycle.

For OPE3-Ph, the optimal power with and without Fermi shift from Table.6.2 was used to obtain the ΔT as a function of κ_{supp}^{ph}. The results are shown in Fig.6.6a and 6.6b. As can be seen, taking the Fermi energy from the DFTB calculations as reference only marginal cooling may be realized. Shifting the Fermi energy to its optimal value increases the reachable ΔT considerably. The results for OPE3-$PhOMe_2$ and OPE3-An are shown in Fig.6.6c and 6.6d, respectively. Overall, to

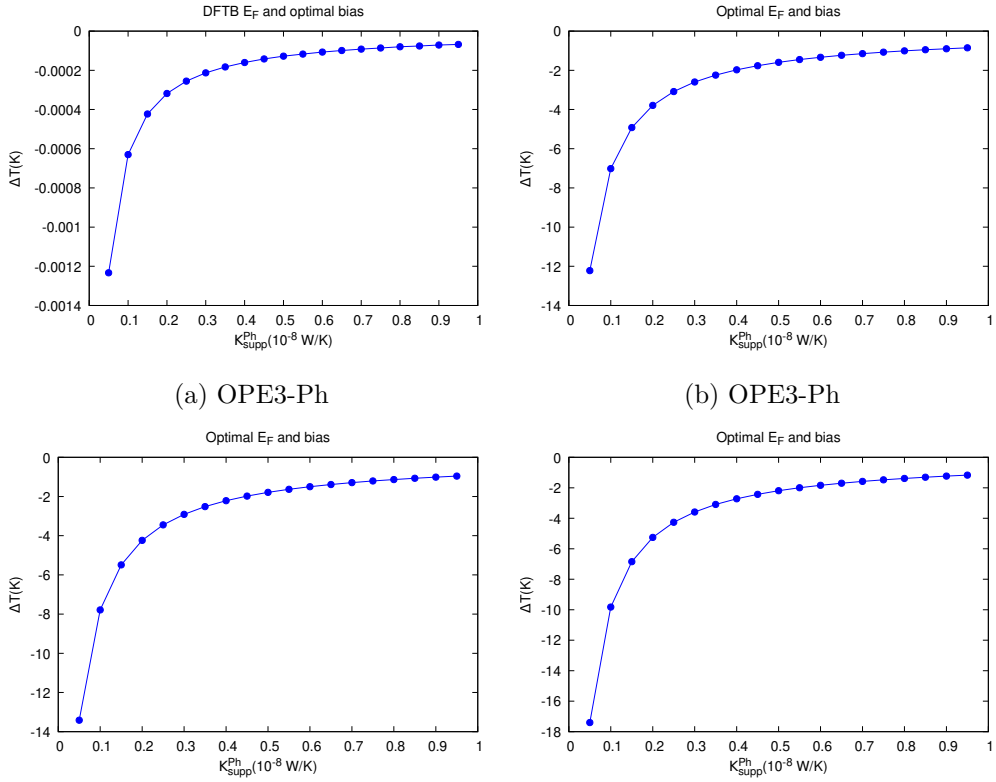

(a) OPE3-Ph

(b) OPE3-Ph

(c) OPE3-PhOMe$_2$

(d) OPE3-An

Figure 6.6: ΔT versus thermal conductance of the support (initial $T_L = T_R = 300$ K) for a) OPE3-Ph with optimal bias and DFTB Fermi energy b) OPE3-Ph with optimal bias and optimal Fermi energy c) OPE3-PhOMe$_2$ with optimal bias and optimal Fermi energy d) OPE3-An with optimal bias and optimal Fermi energy.

reach a decent-sized ΔT, the thermal transport of the support should be around 10^{-9} W/K. As expected, OPE3-An and OPE3-PhOMe$_2$ show a higher temperature change compared with OPE3-Ph.

To sum up, I-V characteristics for OPE3 derivatives were computed. A nearly symmetrical coupling to the leads was found in the transport device. We predict in bias values higher than 0.5 V, OPE3-An and OPE3-PhOMe$_2$ show a higher value for current compared with OPE3-Ph. The bias dependent transmission were used to obtain the heat dissipated in the leads at non-equilibrium condition. Moreover, to minimize the heating power the Fermi energy was shifted towards LUMO and the optimal values were found in the range of nW cooling. Next, an electro-thermal circuit was introduced which couples the electronic net cooling out of equilibrium

with thermal properties of the molecule and the setup. The temperature change of OPE3 derivatives in this circuit model was obtained using optimal E_F and power. Overall, these results show that the OPE3 derivatives are promising candidates to achieve cooling at the device level. The temperature differences shown in Fig.6.6 b-d, present clearly an optimistic upper bound. To reach these values one needs to achieve a further minimization of (negative) heat loss to the support as well as good electrostatic control.

Conclusion

"Do not go where the path may lead, go instead where there is no path and leave a trail."

— Ralph Waldo Emerson

The objective in this thesis was to compute the thermoelectric properties of OPE3 derivatives using ab-initio and molecular dynamics methods in the framework of the EFINED project. Moreover, the limitations of the theories and the comparison of their results with the experiment were studied.

First, we reviewed DFT and DFTB methods. We mentioned that to overcome the size limitation in DFT, one can use DFTB to investigate electronic structure of molecular systems [38, 44]. As shown in this work, the binding energies for a given structure in DFT and DFTB correspond each other. However, for the periodic gold surface, the Slater-Koster parameterization in DFTB can not be used for structure optimization. Accordingly, we used DFT to construct the transport device and NEGF-DFTB to obtain electronic transport properties OPE3 derivatives. We studied the effect of side groups on the electronic conductance and thermopower of OPE3 molecular junctions, OPE3-Ph, OPE3-$PhOMe_2$ and OPE3-An. Our results were compared to the experiment results. In general the theoretical results are overestimated compared with the experiments. However, our theoretical simulations confirm the experimental transport mechanism with a small variability in the thermopower. We have shown that these molecules show the structural features

that are required for thermal conductance studies [2]. MD calculations were applied to compute phonon transport in molecular junctions where the NEMD method was used [54, 70]. Please summarize the main results obtained in MD, regarding ballistic transport, relative increase due to the bridge, and the interpretation you gave. Combining the electron and phonon properties of OPE3 derivatives, we calculated the ZT figure of merit for cross-linked molecular junctions: OPE3-Ph, OPE3-CD and OPE3-CDR. The figure of merit for OPE3-Ph, OPE3-CD and OPE3-CDR is 1.72×10^{-4}, 4.55×10^{-4}, and 10.83×10^{-4}, respectively. Finally, the optimal cooling power were calculated for the molecular junctions under bias voltage. At last, applying an electro-thermal circuit model, the maximum cooling temperatures were computed.

As mentioned in this work, the biggest challenge in our theoretical study to compute thermoelectric efficiency of the molecular junctions using DFT (or DFTB), is the overestimation of electronic predictions which comes from the lack of control in energy level alignment and inaccuracy of exchange-correlation functionals [102]. Nonetheless, the ab-initio calculations accompany the experiments as they can predict the trends observed in experimental data [142]. Moreover, to approach the experiment conditions, we could sample a larger surface in the molecular junctions.

Elaborate on transition to thin films, other bridges, etc..

Bibliography

[1] E. Mykkänen, J. S. Lehtinen, L. Grönberg, A. Shchepetov, A. V. Timofeev, D. Gunnarsson, A. Kemppinen, A. J. Manninen, and M. Prunnila, "Thermionic junction devices utilizing phonon blocking," *Science advances*, vol. 6, no. 15, p. eaax9191, 2020. viii, xii, 2, 88, 89

[2] H. Dekkiche, A. Gemma, F. Tabatabaei, A. S. Batsanov, T. Niehaus, B. Gotsmann, and M. R. Bryce, "Electronic conductance and thermopower of single-molecule junctions of oligo (phenyleneethynylene) derivatives," *Nanoscale*, vol. 12, no. 36, pp. 18908–18917, 2020. x, xiii, 45, 47, 48, 49, 50, 55, 56, 62, 63, 93

[3] L. Cui, R. Miao, K. Wang, D. Thompson, L. A. Zotti, J. C. Cuevas, E. Meyhofer, and P. Reddy, "Peltier cooling in molecular junctions," *Nature nanotechnology*, vol. 13, no. 2, pp. 122–127, 2018. xi, 1, 44, 82, 85, 86, 88

[4] N. Mosso, H. Sadeghi, A. Gemma, S. Sangtarash, U. Drechsler, C. Lambert, and B. Gotsmann, "Thermal transport through single-molecule junctions," *Nano letters*, vol. 19, no. 11, pp. 7614–7622, 2019. xii, 41, 48, 69, 88, 89

[5] B. J. Henz, P. W. Chung, J. W. Andzelm, T. L. Chantawansri, J. L. Lenhart, and F. L. Beyer, "Determination of binding energy and solubility paramet-

ers for functionalized gold nanoparticles by molecular dynamics simulation," *Langmuir*, vol. 27, no. 12, pp. 7836–7842, 2011. xiii, 67, 68

[6] L. Rincón-García, C. Evangeli, G. Rubio-Bollinger, and N. Agraït, "Thermopower measurements in molecular junctions," *Chemical Society Reviews*, vol. 45, no. 15, pp. 4285–4306, 2016. 1, 42, 48

[7] W. B. Chang, C.-K. Mai, M. Kotiuga, J. B. Neaton, G. C. Bazan, and R. A. Segalman, "Controlling the thermoelectric properties of thiophene-derived single-molecule junctions," *Chemistry of Materials*, vol. 26, no. 24, pp. 7229–7235, 2014. 1, 41, 48

[8] L. Cui, R. Miao, C. Jiang, E. Meyhofer, and P. Reddy, "Perspective: Thermal and thermoelectric transport in molecular junctions," *The Journal of Chemical Physics*, vol. 146, no. 9, p. 092201, 2017. 1, 41, 42

[9] L. Cui, W. Jeong, V. Fernández-Hurtado, J. Feist, F. J. García-Vidal, J. C. Cuevas, E. Meyhofer, and P. Reddy, "Study of radiative heat transfer in ångström-and nanometre-sized gaps," *Nature communications*, vol. 8, no. 1, pp. 1–9, 2017. 1, 42, 48

[10] L. Cui, S. Hur, Z. A. Akbar, J. C. Klöckner, W. Jeong, F. Pauly, S.-Y. Jang, P. Reddy, and E. Meyhofer, "Thermal conductance of single-molecule junctions," *Nature*, vol. 572, no. 7771, pp. 628–633, 2019. 1, 78

[11] Y. Dubi and M. Di Ventra, "Colloquium: Heat flow and thermoelectricity in atomic and molecular junctions," *Reviews of Modern Physics*, vol. 83, no. 1, p. 131, 2011. 1, 41, 44

[12] P. Darancet, J. R. Widawsky, H. J. Choi, L. Venkataraman, and J. B. Neaton, "Quantitative current–voltage characteristics in molecular junctions from first principles," *Nano letters*, vol. 12, no. 12, pp. 6250–6254, 2012. 1, 81, 84

[13] R. G. Parr, "Density functional theory of atoms and molecules," in *Horizons of quantum chemistry*, pp. 5–15, Springer, 1980. 5

[14] R. Car, "Introduction to density-functional theory and ab-initio molecular dynamics," *Quantitative Structure-Activity Relationships*, vol. 21, no. 2, pp. 97–104, 2002. 5

[15] N. Argaman and G. Makov, "Density functional theory: An introduction," *American Journal of Physics*, vol. 68, no. 1, pp. 69–79, 2000. 5

[16] W. Kohn, "Nobel lecture: Electronic structure of matter—wave functions and density functionals," *Reviews of Modern Physics*, vol. 71, no. 5, p. 1253, 1999. 6

[17] P. Hohenberg and W. Kohn, "Inhomogeneous electron gas," *Physical review*, vol. 136, no. 3B, p. B864, 1964. 7, 8

[18] P. A. Dirac, "Note on exchange phenomena in the thomas atom," in *Mathematical Proceedings of the Cambridge Philosophical Society*, vol. 26, pp. 376–385, Cambridge University Press, 1930. 9

[19] D. M. Ceperley and B. J. Alder, "Ground state of the electron gas by a stochastic method," *Physical Review Letters*, vol. 45, no. 7, p. 566, 1980. 10

[20] J. P. Perdew and Y. Wang, "Pair-distribution function and its coupling-constant average for the spin-polarized electron gas," *Physical Review B*, vol. 46, no. 20, p. 12947, 1992. 10

[21] J. P. Perdew, K. Burke, and Y. Wang, "Generalized gradient approximation for the exchange-correlation hole of a many-electron system," *Physical Review B*, vol. 54, no. 23, p. 16533, 1996. 10, 50

[22] J. P. Perdew, K. Burke, and M. Ernzerhof, "Generalized gradient approximation made simple," *Physical review letters*, vol. 77, no. 18, p. 3865, 1996. 10, 11

[23] P. Ziesche, S. Kurth, and J. P. Perdew, "Density functionals from lda to gga," *Computational materials science*, vol. 11, no. 2, pp. 122–127, 1998. 10

[24] J. P. Perdew and K. Schmidt, "Jacob's ladder of density functional approximations for the exchange-correlation energy," in *AIP Conference Proceedings*, vol. 577, pp. 1–20, American Institute of Physics, 2001. 10, 11

[25] A. D. Becke, "A new mixing of hartree–fock and local density-functional theories," *The Journal of chemical physics*, vol. 98, no. 2, pp. 1372–1377, 1993. 11

[26] A. Savin and H.-J. Flad, "Density functionals for the yukawa electron-electron interaction," *International Journal of Quantum Chemistry*, vol. 56, no. 4, pp. 327–332, 1995. 11

[27] J. Toulouse, F. Colonna, and A. Savin, "Long-range–short-range separation of the electron-electron interaction in density-functional theory," *Physical Review A*, vol. 70, no. 6, p. 062505, 2004. 11

[28] A. D. Becke, "Density-functional thermochemistry. iv. a new dynamical correlation functional and implications for exact-exchange mixing," *The Journal of chemical physics*, vol. 104, no. 3, pp. 1040–1046, 1996. 11

[29] M. Segall, P. J. Lindan, M. a. Probert, C. J. Pickard, P. J. Hasnip, S. Clark, and M. Payne, "First-principles simulation: ideas, illustrations and the castep code," *Journal of physics: condensed matter*, vol. 14, no. 11, p. 2717, 2002. 14

[30] K. F. Garrity, J. W. Bennett, K. M. Rabe, and D. Vanderbilt, "Pseudopotentials for high-throughput dft calculations," *Computational Materials Science*, vol. 81, pp. 446–452, 2014. 14

[31] W. Kohn and L. J. Sham, "Self-consistent equations including exchange and correlation effects," *Physical review*, vol. 140, no. 4A, p. A1133, 1965. 14

[32] B. Tong and L. Sham, "Application of a self-consistent scheme including exchange and correlation effects to atoms," *Physical Review*, vol. 144, no. 1, p. 1, 1966. 14

[33] A. F. Oliveira, G. Seifert, T. Heine, and H. A. Duarte, "Density-functional based tight-binding: an approximate dft method," *Journal of the Brazilian Chemical Society*, vol. 20, no. 7, pp. 1193–1205, 2009. 15

[34] M. Sternberg, *The atomic structure of diamond surfaces and interfaces*. PhD thesis, Fachbereich Physik der Universität Paderborn, 2001. 15, 18, 19

[35] T. Frauenheim, G. Seifert, M. Elsterner, Z. Hajnal, G. Jungnickel, D. Porezag, S. Suhai, and R. Scholz, "A self-consistent charge density-functional based tight-binding method for predictive materials simulations in physics, chemistry and biology," *physica status solidi (b)*, vol. 217, no. 1, pp. 41–62, 2000. 15

[36] P. Koskinen and V. Mäkinen, "Density-functional tight-binding for beginners," *Computational Materials Science*, vol. 47, no. 1, pp. 237–253, 2009. 15, 16

[37] J. C. Slater and G. F. Koster, "Simplified lcao method for the periodic potential problem," *Physical Review*, vol. 94, no. 6, p. 1498, 1954. 15, 18

[38] W. M. C. Foulkes and R. Haydock, "Tight-binding models and density-functional theory," *Physical review B*, vol. 39, no. 17, p. 12520, 1989. 17, 18, 19, 92

[39] M. Elstner, D. Porezag, G. Jungnickel, J. Elsner, M. Haugk, T. Frauenheim, S. Suhai, and G. Seifert, "Self-consistent-charge density-functional tight-binding method for simulations of complex materials properties," *Physical Review B*, vol. 58, no. 11, p. 7260, 1998. 17, 51, 56

[40] M. Elstner, "Scc-dftb: what is the proper degree of self-consistency?," *The Journal of Physical Chemistry A*, vol. 111, no. 26, pp. 5614–5621, 2007. 17

[41] Y. Yang, H. Yu, D. York, Q. Cui, and M. Elstner, "Extension of the self-consistent-charge density-functional tight-binding method: third-order expansion of the density functional theory total energy and introduction of a modified effective coulomb interaction," *The Journal of Physical Chemistry A*, vol. 111, no. 42, pp. 10861–10873, 2007. 17

[42] R. Mulliken, "Electronic population analysis on lcao-mo molecular wave functions. iv. bonding and antibonding in lcao and valence-bond theories," *The Journal of Chemical Physics*, vol. 23, no. 12, pp. 2343–2346, 1955. 19

[43] T. Frauenheim, G. Seifert, M. Elstner, T. Niehaus, C. Köhler, M. Amkreutz, M. Sternberg, Z. Hajnal, A. Di Carlo, and S. Suhai, "Atomistic simulations of complex materials: ground-state and excited-state properties," *Journal of Physics: Condensed Matter*, vol. 14, no. 11, p. 3015, 2002. 19

[44] M. Elstner and G. Seifert, "Density functional tight binding," *Philosophical Transactions of the Royal Society A: Mathematical, Physical and Engineering Sciences*, vol. 372, no. 2011, p. 20120483, 2014. 19, 92

[45] A. E. Reed, R. B. Weinstock, and F. Weinhold, "Natural population analysis," *The Journal of Chemical Physics*, vol. 83, no. 2, pp. 735–746, 1985. 19

[46] R. Landauer, "Spatial variation of currents and fields due to localized scatterers in metallic conduction," *IBM Journal of research and development*, vol. 1, no. 3, pp. 223–231, 1957. 21, 22, 23

[47] A. Pecchia, G. Penazzi, L. Salvucci, and A. Di Carlo, "Non-equilibrium green's functions in density functional tight binding: method and applications," *New Journal of Physics*, vol. 10, no. 6, p. 065022, 2008. 22, 24, 25

[48] S. Datta, *Quantum transport: atom to transistor*. Cambridge university press, 2005. 22

[49] M. Büttiker, Y. Imry, R. Landauer, and S. Pinhas, "Generalized many-channel conductance formula with application to small rings," *Physical Review B*, vol. 31, no. 10, p. 6207, 1985. 23

[50] D. A. Areshkin and B. K. Nikolić, "Electron density and transport in top-gated graphene nanoribbon devices: First-principles green function algorithms for systems containing a large number of atoms," *Physical Review B*, vol. 81, no. 15, p. 155450, 2010. 23

[51] D. S. Fisher and P. A. Lee, "Relation between conductivity and transmission matrix," *Physical Review B*, vol. 23, no. 12, p. 6851, 1981. 24

[52] L. V. Keldysh *et al.*, "Diagram technique for nonequilibrium processes," *Sov. Phys. JETP*, vol. 20, no. 4, pp. 1018–1026, 1965. 24, 25

[53] N. Marzari, A. A. Mostofi, J. R. Yates, I. Souza, and D. Vanderbilt, "Maximally localized wannier functions: Theory and applications," *Reviews of Modern Physics*, vol. 84, no. 4, p. 1419, 2012. 25

[54] D. Frenkel and B. Smit, *Understanding molecular simulation: from algorithms to applications*, vol. 1. Elsevier, 2001. 27, 93

[55] D. Poulikakos, S. Arcidiacono, and S. Maruyama, "Molecular dynamics simulation in nanoscale heat transfer: a review," *Microscale Thermophysical Engineering*, vol. 7, no. 3, pp. 181–206, 2003. 28

[56] L. Verlet, "Computer" experiments" on classical fluids. i. thermodynamical properties of lennard-jones molecules," *Physical review*, vol. 159, no. 1, p. 98, 1967. 28, 31

[57] M. P. Allen and D. J. Tildesley, *Computer simulation of liquids*. Oxford university press, 2017. 28

[58] A. Rahman and F. H. Stillinger, "Propagation of sound in water. a molecular-dynamics study," *Physical Review A*, vol. 10, no. 1, p. 368, 1974. 28

[59] K. Patkowski and K. Szalewicz, "Argon pair potential at basis set and excitation limits," *The Journal of chemical physics*, vol. 133, no. 9, p. 094304, 2010. 29

[60] M. Bixon and S. Lifson, "Potential functions and conformations in cycloalkanes," *Tetrahedron*, vol. 23, no. 2, pp. 769–784, 1967. 29

[61] S. Lifson and A. Warshel, "Consistent force field for calculations of conformations, vibrational spectra, and enthalpies of cycloalkane and n-alkane molecules," *The Journal of Chemical Physics*, vol. 49, no. 11, pp. 5116–5129, 1968. 29

[62] J. W. Ponder and D. A. Case, "Force fields for protein simulations," *Advances in protein chemistry*, vol. 66, pp. 27–85, 2003. 29

[63] J. Wang, R. M. Wolf, J. W. Caldwell, P. A. Kollman, and D. A. Case, "Development and testing of a general amber force field," *Journal of computational chemistry*, vol. 25, no. 9, pp. 1157–1174, 2004. 29, 30

[64] W. D. Cornell, P. Cieplak, C. I. Bayly, I. R. Gould, K. M. Merz, D. M. Ferguson, D. C. Spellmeyer, T. Fox, J. W. Caldwell, and P. A. Kollman, "A second generation force field for the simulation of proteins, nucleic acids, and organic molecules," *Journal of the American Chemical Society*, vol. 117, no. 19, pp. 5179–5197, 1995. 29, 30, 31

[65] W. L. Jorgensen and J. Pranata, "Importance of secondary interactions in triply hydrogen bonded complexes: guanine-cytosine vs uracil-2, 6-diaminopyridine," *Journal of the American Chemical Society*, vol. 112, no. 5, pp. 2008–2010, 1990. 30

[66] J. N. Canongia Lopes, J. Deschamps, and A. A. Pádua, "Modeling ionic liquids using a systematic all-atom force field," *The Journal of Physical Chemistry B*, vol. 108, no. 6, pp. 2038–2047, 2004. 30

[67] D. Kony, W. Damm, S. Stoll, and W. F. Van Gunsteren, "An improved opls–aa force field for carbohydrates," *Journal of computational chemistry*, vol. 23, no. 15, pp. 1416–1429, 2002. 30

[68] B. Doherty, X. Zhong, S. Gathiaka, B. Li, and O. Acevedo, "Revisiting opls force field parameters for ionic liquid simulations," *Journal of chemical theory and computation*, vol. 13, no. 12, pp. 6131–6145, 2017. 30

[69] S. J. Weiner, P. A. Kollman, D. A. Case, U. C. Singh, C. Ghio, G. Alagona, S. Profeta, and P. Weiner, "A new force field for molecular mechanical simulation of nucleic acids and proteins," *Journal of the American Chemical Society*, vol. 106, no. 3, pp. 765–784, 1984. 30

[70] K. Termentzidis and S. Merabia, "Molecular dynamics simulations and thermal transport at the nano-scale," *Molecular Dynamics–Theoretical Developments and Applications in Nanotechnology and Energy, ed. L. Wang, InTech*, p. 73, 2012. 31, 36, 93

[71] W. C. Swope, H. C. Andersen, P. H. Berens, and K. R. Wilson, "A computer simulation method for the calculation of equilibrium constants for the formation of physical clusters of molecules: Application to small water clusters," *The Journal of chemical physics*, vol. 76, no. 1, pp. 637–649, 1982. 31

[72] J. C. Maxwell, "V. illustrations of the dynamical theory of gases.—part i. on the motions and collisions of perfectly elastic spheres," *The London, Edinburgh, and Dublin Philosophical Magazine and Journal of Science*, vol. 19, no. 124, pp. 19–32, 1860. 33

[73] J. C. Maxwell, "Ii. illustrations of the dynamical theory of gases," *The London, Edinburgh, and Dublin Philosophical Magazine and Journal of Science*, vol. 20, no. 130, pp. 21–37, 1860. 33

[74] F. Mandl, "Statistical physics, manchester physics," 2008. 33

[75] M. Born and T. Von Karman, "Vibrations in space gratings (molecular frequencies)," *Z Phys*, vol. 13, pp. 297–309, 1912. 33

[76] B. M. Szyja and D. Vanpoucke, "9. computational chemistry experiment possibilities," *Zeolites and Metal-Organic Frameworks*, p. 235, 2010. 33

[77] T. Dumitrica, *Trends in Computational Nanomechanics: Transcending Length and Time Scales*, vol. 9. Springer Science & Business Media, 2010. 36

[78] S. Kotake and S. Wakuri, "Molecular dynamics study of heat conduction in solid materials," *JSME International Journal Series B Fluids and Thermal Engineering*, vol. 37, no. 1, pp. 103–108, 1994. 36

[79] P. Chantrenne and J.-L. Barrat, "Analytical model for the thermal conductivity of nanostructures," *Superlattices and Microstructures*, vol. 35, no. 3-6, pp. 173–186, 2004. 36

[80] D. J. Evans, "Thermal conductivity of the lennard-jones fluid," *Physical Review A*, vol. 34, no. 2, p. 1449, 1986. 36

[81] M. Stevens, "Predator perception and the interrelation between different forms of protective coloration," *Proceedings of the Royal Society B: Biological Sciences*, vol. 274, no. 1617, pp. 1457–1464, 2007. 36

[82] A. J. McGaughey and J. M. Larkin, "Predicting phonon properties from equilibrium molecular dynamics simulations," *Annual review of heat transfer*, vol. 17, 2014. 37, 38

[83] D. Morin, "Normal modes," *Harvard University. http://www. people. f as. harvard. edu/djmorin/waves/normalmodes. pdf*, 2002. 37

[84] S. Widnall, "Lecture l19-vibration, normal modes, natural frequencies, instability," *Dynamics*, 2009. 37

[85] M. T. Dove and M. T. Dove, *Introduction to lattice dynamics*, vol. 4. Cambridge university press, 1993. 38, 40

[86] N. Neto, R. Righini, S. t. Califano, and S. Walmsley, "Lattice dynamics of molecular crystals using atom—atom and multipole—multipole potentials," *Chemical Physics*, vol. 29, no. 1-2, pp. 167–179, 1978. 38

[87] H. Han, S. Mérabia, and F. üller Plathe, "Thermal transport at solid–liquid interfaces: High pressure facilitates heat flow through nonlocal liquid structuring," *The journal of physical chemistry letters*, vol. 8, no. 9, pp. 1946–1951, 2017. 38, 71

[88] C. Kittel, P. McEuen, and P. McEuen, *Introduction to solid state physics*, vol. 8. Wiley New York, 1996. 38

[89] G. P. Srivastava, *The physics of phonons*. Routledge, 2019. 38

[90] R. T. Balmer, *Modern engineering thermodynamics-textbook with tables booklet*. Academic Press, 2011. 41

[91] D. K. C. MacDonald, *Thermoelectricity: an introduction to the principles*. Courier Corporation, 2006. 41, 43, 44, 45

[92] A. Aviram and M. A. Ratner, "Molecular rectifiers," *Chemical physics letters*, vol. 29, no. 2, pp. 277–283, 1974. 41

[93] J. C. Cuevas and E. Scheer, "Molecular electronics: An introduction to theory and experiment," 2010. 41, 62, 74

[94] D. Xiang, X. Wang, C. Jia, T. Lee, and X. Guo, "Molecular-scale electronics: from concept to function," *Chemical reviews*, vol. 116, no. 7, pp. 4318–4440, 2016. 41

[95] N. J. Tao, "Electron transport in molecular junctions," *Nanoscience And Technology: A Collection of Reviews from Nature Journals*, pp. 185–193, 2010. 41

[96] M. Galperin, M. A. Ratner, A. Nitzan, and A. Troisi, "Nuclear coupling and polarization in molecular transport junctions: beyond tunneling to function," *Science*, vol. 319, no. 5866, pp. 1056–1060, 2008. 41

[97] A. Nitzan and M. A. Ratner, "Electron transport in molecular wire junctions," *Science*, vol. 300, no. 5624, pp. 1384–1389, 2003. 41

[98] F. Chen, J. Hihath, Z. Huang, X. Li, and N. Tao, "Measurement of single-molecule conductance," *Annu. Rev. Phys. Chem.*, vol. 58, pp. 535–564, 2007. 41

[99] K. Wang, E. Meyhofer, and P. Reddy, "Thermal and thermoelectric properties of molecular junctions," *Advanced Functional Materials*, vol. 30, no. 8, p. 1904534, 2020. 41

[100] J. K. Sowa, J. A. Mol, and E. M. Gauger, "Marcus theory of thermoelectricity in molecular junctions," *The Journal of Physical Chemistry C*, vol. 123, no. 7, pp. 4103–4108, 2019. 41

[101] I. M. Grace, G. Olsen, J. Hurtado-Gallego, L. Rincón-García, G. Rubio-Bollinger, M. R. Bryce, N. Agraït, and C. J. Lambert, "Connectivity dependent thermopower of bridged biphenyl molecules in single-molecule junctions," *Nanoscale*, vol. 12, no. 27, pp. 14682–14688, 2020. 41

[102] F. Evers, R. Korytár, S. Tewari, and J. M. van Ruitenbeek, "Advances and challenges in single-molecule electron transport," *Reviews of Modern Physics*, vol. 92, no. 3, p. 035001, 2020. 41, 80, 93

[103] W. Lee, K. Kim, W. Jeong, L. A. Zotti, F. Pauly, J. C. Cuevas, and P. Reddy, "Heat dissipation in atomic-scale junctions," *Nature*, vol. 498, no. 7453, pp. 209–212, 2013. 41, 83

[104] C. Finch, V. Garcia-Suarez, and C. Lambert, "Giant thermopower and figure of merit in single-molecule devices," *Physical review b*, vol. 79, no. 3, p. 033405, 2009. 42, 45

[105] J. P. Bergfield, M. A. Solis, and C. A. Stafford, "Giant thermoelectric effect from transmission supernodes," *ACS nano*, vol. 4, no. 9, pp. 5314–5320, 2010. 42

[106] H. Sadeghi, S. Sangtarash, and C. J. Lambert, "Oligoyne molecular junctions for efficient room temperature thermoelectric power generation," *Nano letters*, vol. 15, no. 11, pp. 7467–7472, 2015. 42, 64

[107] V. Tayari, B. Senkovskiy, D. Rybkovskiy, N. Ehlen, A. Fedorov, C.-Y. Chen, J. Avila, M. Asensio, A. Perucchi, P. Di Pietro, *et al.*, "Quasi-two-dimensional thermoelectricity in snse," *Physical Review B*, vol. 97, no. 4, p. 045424, 2018. 42

[108] A. Tan, S. Sadat, and P. Reddy, "Measurement of thermopower and current-voltage characteristics of molecular junctions to identify orbital alignment," *Applied Physics Letters*, vol. 96, no. 1, p. 013110, 2010. 43, 81

[109] K. Esfarjani, M. Zebarjadi, and Y. Kawazoe, "Thermoelectric properties of a nanocontact made of two-capped single-wall carbon nanotubes calculated within the tight-binding approximation," *Physical Review B*, vol. 73, no. 8, p. 085406, 2006. 43, 46

[110] F. Rosi, "Thermoelectricity and thermoelectric power generation," *Solid-State Electronics*, vol. 11, no. 9, pp. 833–868, 1968. 44, 45, 46, 76

[111] L. L. Baranowski, G. J. Snyder, and E. S. Toberer, "The misconception of maximum power and power factor in thermoelectrics," *J. Appl. Phys.*, vol. 115, p. 126102, 2014. 45

[112] A. Harzheim, "Thermoelectricity in single-molecule devices," *Materials Science and Technology*, vol. 34, no. 11, pp. 1275–1286, 2018. 48

[113] Q. Zhang, Y. Sun, W. Xu, and D. Zhu, "Organic thermoelectric materials: emerging green energy materials converting heat to electricity directly and efficiently," *Advanced Materials*, vol. 26, no. 40, pp. 6829–6851, 2014. 48

[114] Q. Zhang, Y. Sun, W. Xu, and D. Zhu, "Thermoelectric materials: Organic thermoelectric materials: Emerging green energy materials converting heat to electricity directly and efficiently (adv. mater. 40/2014)," *Advanced Materials*, vol. 26, no. 40, pp. 6828–6828, 2014. 48

[115] Q. H. Al-Galiby, H. Sadeghi, L. A. Algharagholy, I. Grace, and C. Lambert, "Tuning the thermoelectric properties of metallo-porphyrins," *Nanoscale*, vol. 8, no. 4, pp. 2428–2433, 2016. 48

[116] P. Moreno-García, M. Gulcur, D. Z. Manrique, T. Pope, W. Hong, V. Kaliginedi, C. Huang, A. S. Batsanov, M. R. Bryce, C. Lambert, *et al.*, "Single-molecule conductance of functionalized oligoynes: Length dependence and junction evolution," *Journal of the American Chemical Society*, vol. 135, no. 33, pp. 12228–12240, 2013. 49, 55

[117] E. Leary, L. A. Zotti, D. Miguel, I. R. Márquez, L. Palomino-Ruiz, J. M. Cuerva, G. Rubio-Bollinger, M. T. González, and N. Agrait, "The role of oligomeric gold–thiolate units in single-molecule junctions of thiol-anchored molecules," *The Journal of Physical Chemistry C*, vol. 122, no. 6, pp. 3211–3218, 2018. 49

[118] J. Lynn, H. Smith, and R. Nicklow, "Lattice dynamics of gold," *Physical Review B*, vol. 8, no. 8, p. 3493, 1973. 49

[119] K. E. Riley, B. T. Op't Holt, and K. M. Merz, "Critical assessment of the performance of density functional methods for several atomic and molecular properties," *Journal of chemical theory and computation*, vol. 3, no. 2, pp. 407–433, 2007. 50

[120] P. Giannozzi, S. Baroni, N. Bonini, M. Calandra, R. Car, C. Cavazzoni, D. Ceresoli, G. L. Chiarotti, M. Cococcioni, I. Dabo, *et al.*, "Quantum espresso: a modular and open-source software project for quantum simula-

tions of materials," *Journal of physics: Condensed matter*, vol. 21, no. 39, p. 395502, 2009. 50

[121] A. Dal Corso, "Pseudopotentials periodic table: From h to pu," *Computational Materials Science*, vol. 95, pp. 337–350, 2014. 50

[122] T. A. Niehaus, M. Elstner, T. Frauenheim, and S. Suhai, "Application of an approximate density-functional method to sulfur containing compounds," *Journal of Molecular Structure: THEOCHEM*, vol. 541, no. 1-3, pp. 185–194, 2001. 51, 56

[123] A. Fihey, C. Hettich, J. Touzeau, F. Maurel, A. Perrier, C. Köhler, B. Aradi, and T. Frauenheim, "Scc-dftb parameters for simulating hybrid gold-thiolates compounds," *Journal of computational chemistry*, vol. 36, no. 27, pp. 2075–2087, 2015. 51, 56

[124] V. Yarzhemsky and C. Battocchio, "The structure of gold nanoparticles and au based thiol self-organized monolayers," *Russian Journal of Inorganic Chemistry*, vol. 56, no. 14, pp. 2147–2159, 2011. 55

[125] M. Valiev, E. J. Bylaska, N. Govind, K. Kowalski, T. P. Straatsma, H. J. Van Dam, D. Wang, J. Nieplocha, E. Apra, T. L. Windus, *et al.*, "Nwchem: A comprehensive and scalable open-source solution for large scale molecular simulations," *Computer Physics Communications*, vol. 181, no. 9, pp. 1477–1489, 2010. 57

[126] A. H. Larsen, J. J. Mortensen, J. Blomqvist, I. E. Castelli, R. Christensen, M. Dułak, J. Friis, M. N. Groves, B. Hammer, C. Hargus, *et al.*, "The atomic simulation environment—a python library for working with atoms," *Journal of Physics: Condensed Matter*, vol. 29, no. 27, p. 273002, 2017. 57, 66

[127] A. Gagliardi, T. A. Niehaus, T. Frauenheim, A. Pecchia, and A. Di Carlo, "Quasiparticle correction for electronic transport in molecular wires," *Journal of Computational Electronics*, vol. 6, no. 1, pp. 345–348, 2007. 63

[128] Y. Kim, W. Jeong, K. Kim, W. Lee, and P. Reddy, "Electrostatic control of thermoelectricity in molecular junctions," *Nature nanotechnology*, vol. 9, no. 11, p. 881, 2014. 64

[129] P. Gehring, A. Harzheim, J. Spiece, Y. Sheng, G. Rogers, C. Evangeli, A. Mishra, B. J. Robinson, K. Porfyrakis, J. H. Warner, *et al.*, "Field-effect control of graphene–fullerene thermoelectric nanodevices," *Nano letters*, vol. 17, no. 11, pp. 7055–7061, 2017. 64

[130] T. Luo and J. R. Lloyd, "Non-equilibrium molecular dynamics study of thermal energy transport in au–sam–au junctions," *International journal of heat and mass transfer*, vol. 53, no. 1-3, pp. 1–11, 2010. 64, 65

[131] T.-Q. Duong, C. Massobrio, G. Ori, M. Boero, and E. Martin, "Thermal resistance of an interfacial molecular layer by first-principles molecular dynamics," *The Journal of Chemical Physics*, vol. 153, no. 7, p. 074704, 2020. 65, 71

[132] L. A. Girifalco and V. G. Weizer, "Application of the morse potential function to cubic metals," *Physical Review*, vol. 114, no. 3, p. 687, 1959. 67

[133] R. N. Costa Filho, G. Alencar, B.-S. Skagerstam, and J. S. Andrade Jr, "Morse potential derived from first principles," *EPL (Europhysics Letters)*, vol. 101, no. 1, p. 10009, 2013. 67

[134] J. C. Klöckner, M. Bürkle, J. C. Cuevas, and F. Pauly, "Length dependence of the thermal conductance of alkane-based single-molecule junctions: An ab initio study," *Physical Review B*, vol. 94, no. 20, p. 205425, 2016. 71

[135] D. Segal and B. K. Agarwalla, "Vibrational heat transport in molecular junctions," *Annual review of physical chemistry*, vol. 67, pp. 185–209, 2016. 71

[136] E. Scheer and J. C. Cuevas, *Molecular electronics: an introduction to theory and experiment*, vol. 15. World Scientific, 2017. 76

[137] W. Wang, T. Lee, and M. A. Reed, "Mechanism of electron conduction in self-assembled alkanethiol monolayer devices," *Physical Review B*, vol. 68, no. 3, p. 035416, 2003. 76

[138] H. B. Akkerman and B. de Boer, "Electrical conduction through single molecules and self-assembled monolayers," *Journal of Physics: Condensed Matter*, vol. 20, no. 1, p. 013001, 2007. 76

[139] Y.-S. Liu, Y.-R. Chen, and Y.-C. Chen, "Thermoelectric efficiency in nanojunctions: a comparison between atomic junctions and molecular junctions," *ACS nano*, vol. 3, no. 11, pp. 3497–3504, 2009. 79

[140] B. Ludoph and J. Van Ruitenbeek, "Thermopower of atomic-size metallic contacts," *Physical Review B*, vol. 59, no. 19, p. 12290, 1999. 79

[141] P. Reddy, S.-Y. Jang, R. A. Segalman, and A. Majumdar, "Thermoelectricity in molecular junctions," *Science*, vol. 315, no. 5818, pp. 1568–1571, 2007. 79, 81

[142] Y. Geng, S. Sangtarash, C. Huang, H. Sadeghi, Y. Fu, W. Hong, T. Wandlowski, S. Decurtins, C. J. Lambert, and S.-X. Liu, "Magic ratios for connectivity-driven electrical conductance of graphene-like molecules," *Journal of the American Chemical Society*, vol. 137, no. 13, pp. 4469–4476, 2015. 80, 93

[143] L. A. Zotti, M. Bürkle, F. Pauly, W. Lee, K. Kim, W. Jeong, Y. Asai, P. Reddy, and J. C. Cuevas, "Heat dissipation and its relation to thermopower in single-molecule junctions," *New Journal of Physics*, vol. 16, no. 1, p. 015004, 2014. 81

[144] G. Foti and H. Vázquez, "Adsorbate-driven cooling of carbene-based molecular junctions," *Beilstein journal of nanotechnology*, vol. 8, no. 1, pp. 2060–2068, 2017. 81

[145] M. A. Reed, C. Zhou, C. Muller, T. Burgin, and J. Tour, "Conductance of a molecular junction," *Science*, vol. 278, no. 5336, pp. 252–254, 1997. 81

[146] A. Vilan, "Analyzing molecular current-voltage characteristics with the simmons tunneling model: scaling and linearization," *The Journal of Physical Chemistry C*, vol. 111, no. 11, pp. 4431–4444, 2007. 81

[147] R. Volkovich, R. Härtle, M. Thoss, and U. Peskin, "Bias-controlled selective excitation of vibrational modes in molecular junctions: A route towards mode-selective chemistry," *Physical Chemistry Chemical Physics*, vol. 13, no. 32, pp. 14333–14349, 2011. 81

[148] Y.-C. Chen, M. Zwolak, and M. Di Ventra, "Inelastic current- voltage characteristics of atomic and molecular junctions," *Nano Letters*, vol. 4, no. 9, pp. 1709–1712, 2004. 81

[149] J. M. Seminario, A. G. Zacarias, and J. M. Tour, "Molecular current- voltage characteristics," *The Journal of Physical Chemistry A*, vol. 103, no. 39, pp. 7883–7887, 1999. 82

[150] C.-K. Wang and Y. Luo, "Current–voltage characteristics of single molecular junction: dimensionality of metal contacts," *The Journal of chemical physics*, vol. 119, no. 9, pp. 4923–4928, 2003. 82

[151] C.-K. Wang, Y. Fu, and Y. Luo, "A quantum chemistry approach for current–voltage characterization of molecular junctions," *Physical Chemistry Chemical Physics*, vol. 3, no. 22, pp. 5017–5023, 2001. 82

[152] K. Kang and T. Lee, "Peltier cooling at molecular scale," *Nature nanotechnology*, vol. 13, no. 2, pp. 97–99, 2018. 82

[153] Y. Selzer, M. A. Cabassi, T. S. Mayer, and D. L. Allara, "Thermally activated conduction in molecular junctions," *Journal of the American Chemical Society*, vol. 126, no. 13, pp. 4052–4053, 2004. 83

[154] B.Gotsmann. bgo@zurich.ibm.com, 2019. 88

Colophon

This thesis is based on a template developed by Matthew Townson and Andrew Reeves. It was typeset with LaTeX 2_ε. It was created using the *memoir* package, maintained by Lars Madsen, with the *madsen* chapter style. The font used is Latin Modern, derived from fonts designed by Donald E. Kunith.